University of Southampton

Faculty of Environmental and Life Sciences

School of Ocean & Earth Science

Mantle Convection and Melt Experiment Located at the Transition Zone

DOI

Volume 1 of 1

by

Yuhang Dai

ORCID ID 0000-0001-9965-7106

Thesis for the degree of Doctor of Philosophy

April 2025

University of Southampton

Abstract

Faculty of Environmental and Life Sciences

School of Ocean & Earth Science

Doctor of Philosophy

Mantle Convection and Melt Experiment Located at the Transition Zone

by

Yuhang Dai

The mantle transition zone plays a significant role in mediating material transport between the upper mantle and lower mantle. Tight constraints on the mantle transition zone discontinuities reflect the locations and degree of such material transport. It is essential for a comprehensive understanding of geochemical reservoirs, hydration cycles, and the evolution of the Earth. We use P-to-S receiver functions calculated from an amphibious dataset in Cascadia to seismically image the underlying mantle transition zone. We find thinning of the mantle transition zone of 10 ± 6 km beneath the ridges and 8 ± 4 km behind the slab. We do not find evidence of thinning directly beneath the Cobb Hotspot. We find the 660 discontinuity topography is the largest signal in terms of magnitude and lateral scale and dominates the pattern of the mantle transition zone thickness, indicating it plays a major role in dominating material transport beneath the Cascadia ridges and subduction zones. The 410 is characterised by smaller variations, with locations of depressions away from locations of those where the 660 is uplifted. However, the depressions occur near slow seismic velocity anomalies imaged in the upper mantle and are accompanied by supra-410 melt phases. This may suggest that upper mantle convection plays a role in material transfer between the MTZ and the upper mantle, potentially entraining hydration from the shallow MTZ to the upper mantle that results in melt. We develop a new discontinuity imaging approach using deconvolved SS precursor phases. We demonstrate its effectiveness by applying it to synthetic seismograms and the global seismic dataset. Moho depths as shallow as 20 km and mantle transition zone discontinuities at 410 km and 660 km are shown to be resolvable. We image the Moho at 21 – 67 km depth beneath continental regions in 77 % of all continental bins, within 10 km of Crust 1.0. The approach shows broad promise for imaging mantle discontinuities. Finally, we apply the new approach to the global broadband seismic data set to image the mantle transition zone globally. The topographies of the mantle transition zone are tested with different migration models, including a 1-D reference model and seismic velocity tomography models. We obtain robust features across different migration models. We find the mantle transition zone is thickened beneath subduction zones with a thickness of ~ 255 – 270 km over 1800 - 3000 km laterally. The locations of thickening are coincident with the locations of inferred cold regions by imaged high-seismic-velocity anomalies in tomography models. We also find

thinning beneath oceans, but no apparent systematic anomalous thinning beneath hotspot regions is resolved. Similar to the observations beneath the Cascadia, the 660 topographies closely resemble the mantle transition zone thickness perturbations. This suggests the 660 topography likely dominates the variation of the mantle transition zone thickness, likely because slabs generally accumulate there, increasing the intensity and length scales of the associated anomalies. In other words, the 660 plays a major role in material transfer to the lower mantle. The lack of expected anticorrelations between the 410 topography and the 660 topography may be because 410 variations occur at a smaller scale, laterally or in-depth, than the resolution of SS precursor imaging. This also suggests that the dynamics of material transport across the mantle transition zone are more complex than simple vertical ascending beneath hotspots and descending beneath subduction zones.

Table of Contents

Table of Figures

Table of Figures

Table of Figures

Table of Figures

Research Thesis: Declaration of Authorship

Print name: Yuhang Dai

Title of thesis: Mantle Convection and Melt Experiment Located at the Transition Zone

I declare that this thesis and the work presented in it are my own and has been generated by me as the result of my own original research.

I confirm that:

1. This work was done wholly or mainly while in candidature for a research degree at this University;
2. Where any part of this thesis has previously been submitted for a degree or any other qualification at this University or any other institution, this has been clearly stated;
3. Where I have consulted the published work of others, this is always clearly attributed;
4. Where I have quoted from the work of others, the source is always given. With the exception of such quotations, this thesis is entirely my own work;
5. I have acknowledged all main sources of help;
6. Where the thesis is based on work done by myself jointly with others, I have made clear exactly what was done by others and what I have contributed myself;
7. Parts of this work have been published as:

Dai, Y., C. A. Rychert and N. Harmon (2023). "Seismic imaging beneath Cascadia shows shallow mantle flow patterns guide lower mantle upwellings." Journal of Geophysical Research: Solid Earth **128**(9): e2023JB026374.

Dai, Y., S. Tharimena, C. Rychert and N. Harmon (2024). "A global SS precursor method for imaging discontinuities: the Moho and beyond." Geophysical Journal International **238**(2): 756-763.

Signature: ..... Date: .....

Acknowledgements

The PhD student life is undoubtedly one of my life's most significant and influential experiences. It is especially remarkable as it started during the COVID-19 pandemic. It would not have been realisable without the help and support I received from numerous people during this journey.

First of all, I would like to express my sincere gratitude to Kate, Catherine A. Rychert. She is such a good supervisor that she has been giving constant scientific guidance and feedback. Also, I appreciate her cooking which I enjoy every time. I would like to express the same appreciation to my co-advisor Nick, Nicholas Harmon who has been providing me with scientific and technical advice and support. It's such an honour and pleasure for me to work with Kate and Nick no matter in Southampton, UK or Woods Hole, US, online or in person. I always admire their passion for science and am inspired by that. The pandemic brought great challenges, but they did an excellent job of maximizing their supervisors and support. This PhD would not be achievable without their guidance, support and encouragement.

This PhD is I also extend my thanks to the hosts of my placements, Yang Shen at the University of Rhode Island, and Ting Yang at the Southern University of Science and Technology. Those visits have not only expanded my scientific view but also enriched my life. Ting Yang is also my previous supervisor who guided me into the seismology field. I'm grateful for his generous support and encouragement.

I enjoyed the time I stayed at the University of Southampton, mostly at, National Oceanography Centre (NOC). It was wonderful to work at the office by the docks. It's a pity that there was no access to the great canteen and view of NOC in the first year due to the lockdown. Meanwhile, I appreciate my wonderful experiences at Woods Hole Oceanographic Institute, the University of Rhode Island, and the Southern University of Science and Technology during the placements.

I genuinely thank my friends and colleagues, thank you for accompanying and supporting me through this journey. Special thanks to Zaanyu Chan, Maoran Li, William Buffett, Puja Banerjee and Xuan Shan. Thanks to so many kind people I have met during my PhD all over those sites, NOC, Rhode Island, WHOI, and SUSTech.

Last but never least, I would like to express my deepest love and gratitude to my parents, Chunming Fu and Kaimin Dai. Thanks for their unconditional love, respect and support. I also extend the same appreciation to my parents' siblings, my families. Nothing would ever have been possible without their support.

Acknowledgements

Definitions and Abbreviations

MTZ..... The mantle transition zone. The region between the upper mantle and the lower mantle within the Earth.

RF..... Receiver function. A time series, computed from three-component seismograms, provides the relative response of Earth structure near the receiver

SNR ..... Signal-to-noise ratio. A value to evaluate the quality of data quantitatively comparing the signal we expect with others (noise).

Chapter 1 Introduction

1.1 Background

The Earth formed billions of years ago via gravitational accretion within the solar nebula, a cloud of gas and dust left over from the Sun's formation (Allegre et al., 1995), resulting in heating and differentiation, consequently forming compositionally distinct layers, including the core, mantle, and crust. The core is made of iron and nickel and consists of a solid inner core and a liquid outer core. The mantle is composed of rocky material, primarily consisting of peridotite and its higher-pressure equivalents, with a high proportion of the mineral olivine. The crust is classified into the continental crust, which is felsic to intermediate in composition and the oceanic crust, which consists primarily of basalts and gabbros. Early on in Earth's history, the core formed, separating denser iron and nickel towards the centre of the Earth. The remaining rocky material coalesced into a solid form, creating the ultramafic mantle, while further melting and differentiation of the mantle generated the mafic and felsic crust that makes up the planet today.

Earth is still cooling from its formation and the ongoing decay of radioactive elements, which results in colder temperatures near its surface in comparison to the asthenosphere. These colder temperatures result in a rigid, shallow mantle that, in combination with the crust, makes up the lithospheric tectonic plate. In the classical geophysical definition, heat transfer by conduction in the rigid lithosphere, whereas the weaker, asthenospheric mantle convects (e.g., Sleep, 2005). Constraining this convection is important for our understanding of the dynamics and evolution of the mantle. The surface expression of mantle convection is plate tectonics, which shapes the oceans and continents that humans live on. In addition, many geohazards are related to mantle convection, for instance, earthquakes at plate boundaries such as the edges of the Pacific plate, and volcanism at mid-ocean ridges, subduction zones and hotspots such as Hawaii. Mantle convection plays an important role in the cycles of water and other volatiles. Volatiles are broadly important in that the presence of water and carbon at the surface of the Earth is an important factor for life on the planet. Hydration may also have been an important factor in initiating plate tectonics, which, in turn, may also be a factor important to planetary habitability. Volatiles are released from the deep Earth into the atmosphere during volcanic eruptions, while subduction brings material from the surface back down into the mantle. Despite large amounts of volatile cycling, the oceans and atmosphere have remained relatively stable, again encouraging and allowing for life on the planet.

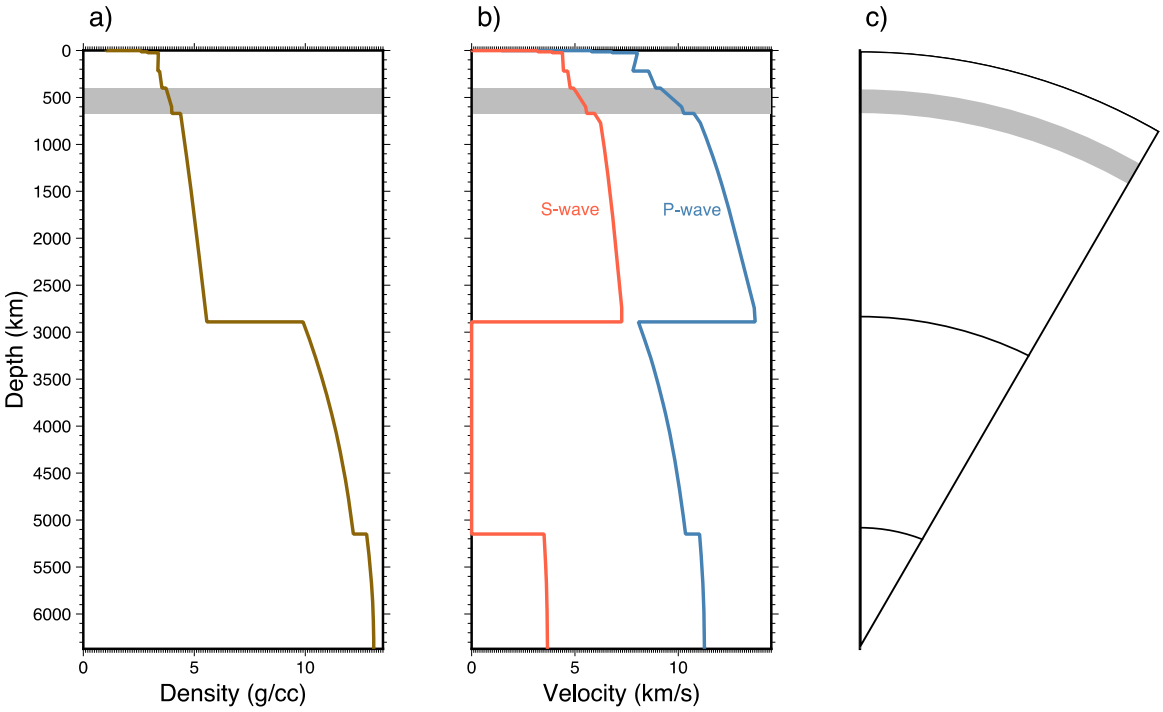

Figure 1.1 1-D Earth structure. a) Density profile of the Earth; b) P-wave (blue) and S-wave (orange) velocity profiles; c) Diagram of the layer structure of the Earth. Grey zones mark the location of the mantle transition zone (MTZ). Values are taken from the Preliminary Reference Earth Model (PREM) (Dziewonski & Anderson, 1981).

The mantle transition zone (MTZ) separates the upper mantle from the lower mantle and is bounded by two prominent seismic discontinuities at approximately 410 km and 660 km depth, as revealed by 1-D Earth reference models (e.g., Dziewonski & Anderson, 1981; Kennett & Engdahl, 1991). The discontinuities herein are referred to as "the 410" and "the 660" (Figure 1.1). The cause of these two seismic velocity increases with depth in the mantle is attributed to the pressure-temperature dependent phase transition of olivine grains into denser crystal structures with depth, in other words, with atomic structures that are dense and more energetically favourable at higher pressures, as determined by laboratory experiments (Ringwood, 1975) (Figure 1.2a). Olivine changes to wadsleyite and majorite at the 410, which is an exothermic reaction (e.g., Katsura & Ito, 1989). The transformation of wadsleyite into γ-spinel ringwoodite happens at around 500 – 600 km within the MTZ (e.g., Rigden et al., 1991), although this transformation is not always observed seismically in 1-D global average and is generally less discussed. Finally, γ-spinel ringwoodite changes to bridgmanite and ferropericlase at the 660, which is an endothermic reaction (e.g., Ishii et al., 2018; Ito & Takahashi, 1989; Ringwood, 1975). Clapeyron slopes from experimental studies describe the pressure-temperature conditions where the phase transformations are predicted to occur. The 410 has a positive Clapeyron slope, meaning that as temperature increases, so does the expected pressure of the phase transition. Conversely, the 660 has a negative Clapeyron slope, and therefore, at a hotter temperature, the predicted depth of the phase transition is decreased. The opposite sign

of the slopes provides the classical interpretation of transition zone thickness, in which it is thinner in hotter regions and thicker in colder regions (Figure 1.2b).

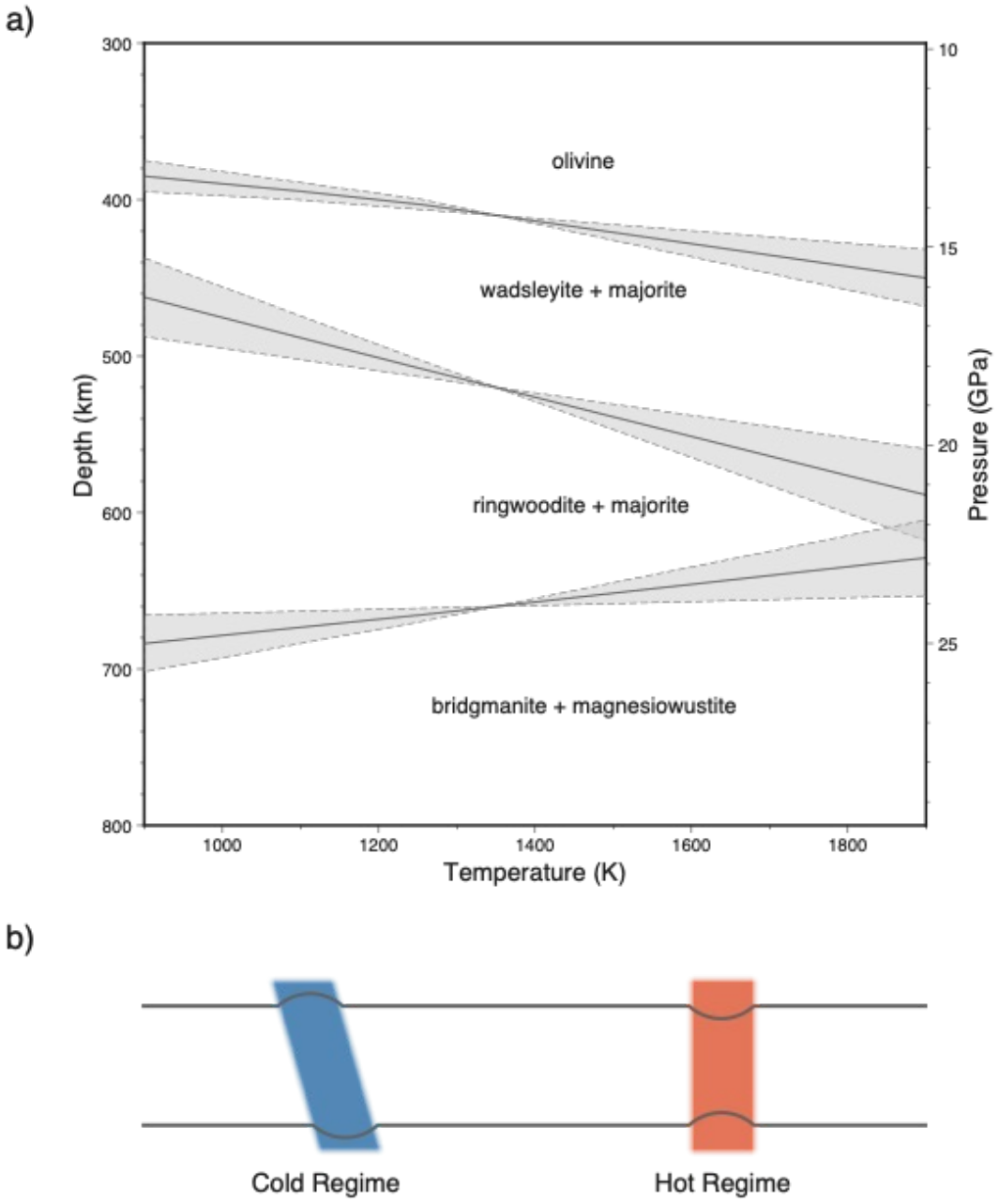

Figure 1.2 Schematic diagram of phase changes and mantle transition zone (MTZ). a) simplified diagram of major mineral phase changes, grey zones show the ranges from different Clapeyron Slopes (Faccenda & Dal Zilio, 2017). b) cartoons of the predicted MTZ topographies change in a cold regime (left) and a hot regime (right), respectively.

The MTZ is important for investigating Earth's dynamics since it acts as a gatekeeper between the upper mantle and lower mantle. Any material transport between the upper mantle and the lower mantle must occur through the transition zone. In addition, it has been suggested that MTZ can store up to several oceans ' worth of water (Hirschmann & Dasgupta, 2009), which has profound meaning

for the understanding of the water cycle of the planet. Moreover, atop MTZ (and/or the shallow lower mantle), widespread deep melt layers might exist (Bercovici & Karato, 2003; Schmandt et al., 2014). The melt layer may act as a geochemical reservoir and/or alter mantle viscosity. Finally, it has been proposed that the composition of the mantle is not necessarily the equilibrium assemblage of olivine that is typically assumed (Xu et al., 2008). Instead, it may be a mechanical mixture with potentially large basalt accumulations in the transition zone, in other words, again acting as a chemical reservoir, with potentially important implications for our understanding of Earth's dynamics.

In the classic model of mantle convection, heat from Earth's core interior causes thermal instabilities in the lower mantle, localised heating reduces viscosity, allowing buoyance, that results in upwellings (Campbell, 2007), referred to as plumes, which sometimes reach the surface of the Earth and result in volcanism at hotspots, such as Hawaii and Iceland (Koppers et al., 2021). In addition, as ocean plates age and cool, their density is increased, resulting in relatively lower viscosity, facilitating the movement of tectonic plates and they descend into the Earth's interior at subduction zones (Karato & Wu, 1993), typically the intersection of a slab and a buoyant, overriding continental plate, such as those that occur at the ring of fire surrounding the Pacific.

Seismic imaging, geodynamic modelling, and geochemical evidence offer some constraints on material transfer through the MTZ. Low seismic velocity anomalies are imaged and interpreted as mantle plumes that originate in the lower mantle and eventually reach the surface (French & Romanowicz, 2015; Montelli et al., 2006; Rickers et al., 2013), and high-velocity anomalies are imaged and associated with subducted slabs descending from the surface to the lower mantle (Fukao & Obayashi, 2013; Goes et al., 2017; Grand et al., 1997; Ritsema et al., 2004). Also, several studies that imaged the MTZ discontinuities found MTZ thinning in plume locations and thickening in slab locations (Flanagan & Shearer, 1998; Goes et al., 2017; Gu & Dziewonski, 2002; Houser et al., 2008; Huang et al., 2019; Lawrence & Shearer, 2008), in agreement with mineral physics predictions for vertical material transfer and associated hotter temperatures beneath hotspots and downward material and associated colder temperatures beneath subduction zones (Ito & Katsura, 1989).

However, greater complexity than the classical model of vertical or near vertical upwellings at hotspots and downwellings at subduction zones is likely required. Unique geochemical signatures at hotspots were once thought to have originated from a compositionally distinct lower mantle (Hofmann, 1997) that cannot be from a homogenous and well-mixed mantle, as might be expected for prolonged large-scale convective patterns. Several conceptual models have been developed as explanations. These include, for instance, pockets of enrichment in a generally heterogeneous Earth (Morgan & Morgan, 1999), isolated piles of material of different chemical composition (French & Romanowicz, 2015; Jellinek & Manga, 2002, 2004; McNamara & Zhong, 2005) that cause sluggish

convection at >1,000 km depth (French & Romanowicz, 2015), compositional layering (Kellogg et al., 1999) caused by slab stagnation at 660 km or 1,000 km (Ballmer et al., 2015; Marquardt & Miyagi, 2015) or stable lower-mantle convective cells of intrinsically strong (Mg, Fe) SiO3-bridgmanite in low-Mg/Si domains (Ballmer et al., 2017). Alternatively, the mantle may pervasively rise across the MTZ but typically be compositionally filtered during the process (Bercovici & Karato, 2003). However, the details of how and where these models might be in operation are still not known in part because observational reports from different methods, resolutions, and locations do not always agree, as we will describe below. In addition, greater complexity has been suggested from seismic imaging. Even if some slabs penetrate, others may stagnate or stagnate temporarily (Contenti et al., 2012; Fukao & Obayashi, 2013; Goes et al., 2017), and plumes may narrow or deflect when they reach the upper mantle (French & Romanowicz, 2015) and/or separate into many thinner plumes, like the branches of a tree (Tsekhmistrenko et al., 2021).

This thesis presents research that focuses on seismic imaging MTZ both regionally and globally, using receiver functions and/or SS precursors. A description of the datasets and methods is presented here.

1.2 The Seismic Data and Preprocessing

1.2.1 The Seismic Data

The data used in this thesis is open-source seismic data acquired from the National Science Foundation's (NSF) Seismological Facility for the Advancement of Geoscience (SAGE) – Data Management Center (DMC). Data was downloaded using the Standing Order for Data (SOD) software that is available from the SAGE website (Owens et al., 2004). Our local archive of the global dataset consists of seismograms of teleseismic earthquakes with magnitudes ≥ 5.5 that happened from 1990 to 2021 (Figure 1.3). With increased seismology observations worldwide in the past decades, over 41,890 broadband seismic stations have been deployed across all continents from the years 1990 to 2021. The data was downloaded as three-component seismograms in SAC format with one Z component (vertical) and two orthogonal horizontal components (N (north) and E (east) for most onshore stations or 1 (horizontal 1) and 2 (horizontal 2) for offshore stations (Ocean Bottom Seismograms) and some onshore stations) recorded by broadband seismometers. The instrument response of corresponding stations was removed while downloading and preprocessing the seismic records using SOD.

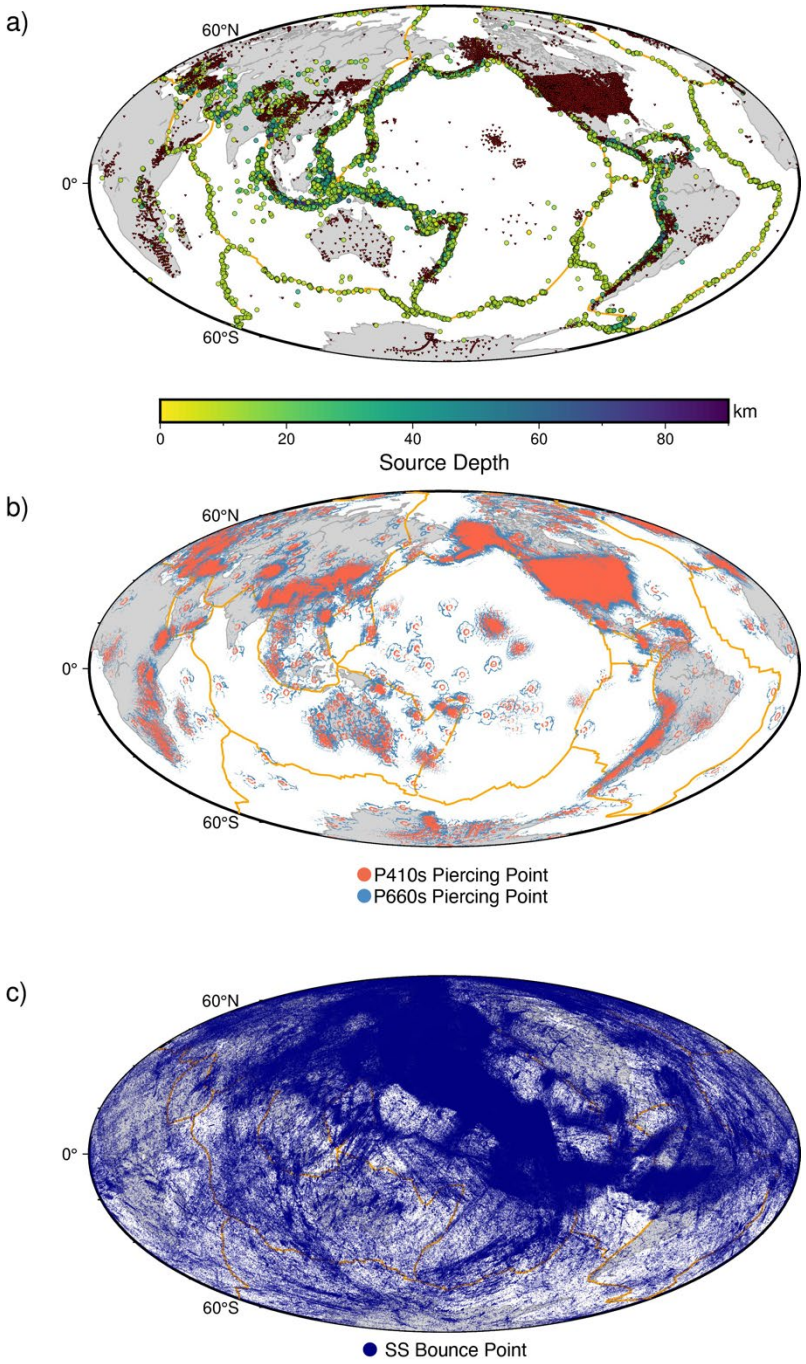

Figure 1.3 Dataset maps. a) Small inversed red triangles show broadband seismic stations from the National Science Foundation (NSF)'s Seismological Facility for the Advancement of Geoscience (SAGE) Data Management Center, which have been deployed from 1990 to 2021. Circles show earthquakes with magnitude > 5.5 Mw, and colours show the source depths. Orange lines show plate boundaries. b) piercing points of event data with epicentre distance between 35 degrees and 80 degrees from the global data set. c) SS bounce points of event data with epicentre distance between 90 degrees and 180 degrees from the global data set.

Seismograms capture ground motion resulting from an earthquake. These displacements are generated by two fundamental modes of body wave propagation: P-waves and S-waves. In the case of P-waves, displacement occurs in the direction of wave propagation, causing a volume change,

which is why they are referred to as compressional waves. For S-waves, the displacement occurs perpendicular to the direction of wave propagation. This type of motion does not result in volume change but instead generates shear forces, which is why S-waves are also called shear waves. The particle motions of an S-wave can be decomposed into two components, SV- and SH- waves. SV-component is that of which the particle motion is within a vertical plane perpendicular to the propagation vector. The particle motion of its orthogonal counterpart, the SH-component, is in the plane perpendicular to the vertical plane (Shearer, 2019). Particle motion for a harmonic compressional wave and shear waves polarized in the vertical plane (SV-wave) and in the horizontal plane (SH-wave) is illustrated in Figure 1.4.

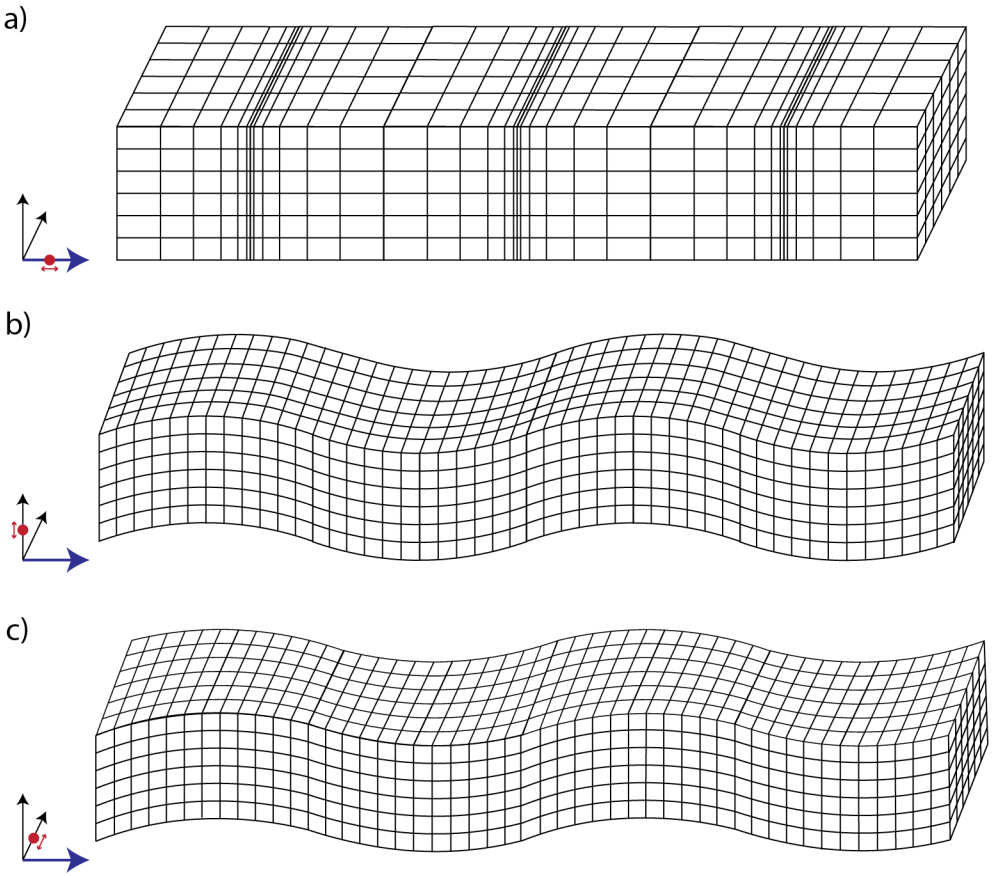

Figure 1.4 Particle polarisation and volume displacement of P- and S- waves. a) The big blue arrow shows the propagation direction of a harmonic plane P-wave. The red dots and arrows illustrate the direction of particle polarisation. The cubes show the displacement when the seismic wave propagates through. b) and c) Similar to a), but for SV- and SH- waves, respectively.

Seismic ray theory offers a fundamental framework to understand the propagation of seismic body waves through the Earth's interior. Analogous to geometrical optical ray theory, the model treats the propagation of seismic body waves as rays via a high-frequency approximation, simplifying the potentially complex wave sensitivity to the ray path of propagation, which is perpendicular to the wavefront (Cerveny, 2005).

The rays follow the rule of Snell's law:

$$\frac{\sin i_1}{\sin i_2} = \frac{v_1}{v_2}$$

where the angle of incidence i_1 in the first layer, and angle of reflection or transmission i_2 are related to the seismic velocities v_1 and v_2 of the two mediums (Figure 1.5).

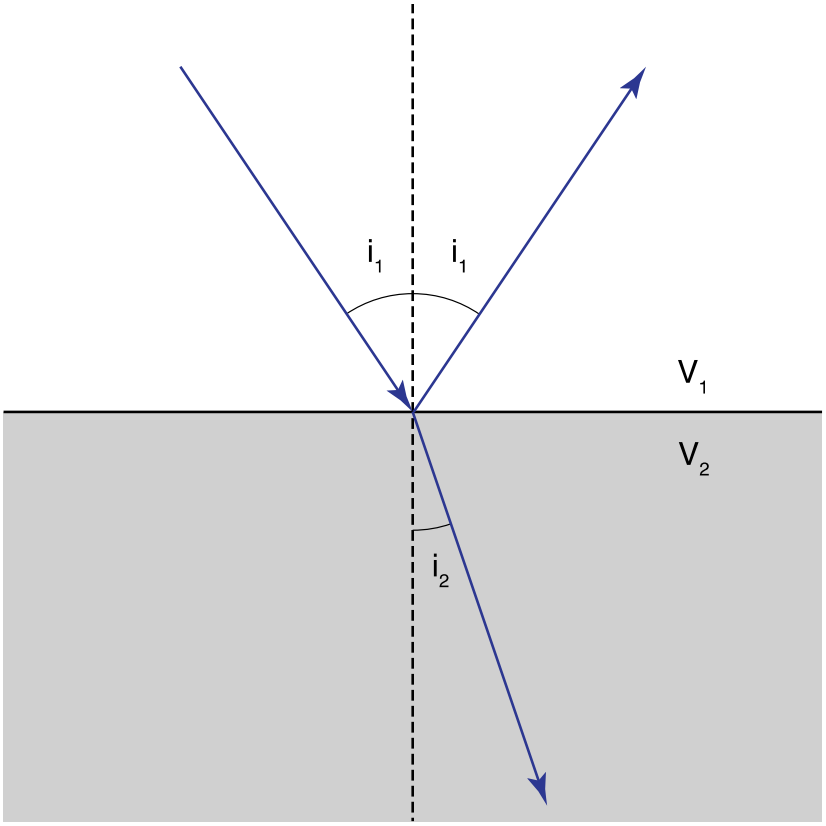

Figure 1.5 Diagram of Snell's Law. Blue arrows represent incidence, reflection and refraction waves at the boundary of two mediums with velocities of v_1 and v_2, respectively.

Broadband seismometers provide seismic signals in three orthogonal components. The two orthogonal horizontal components are usually directed to the North and East. However, due to the free-fall deployment of the ocean bottom seismometer, the horizontal components don't align with the geographic north and east but in random directions. Therefore, the first step of utilizing the horizontal 1 and 2 components is to orientate them to the north and east directions. There are a number of different approaches to obtaining the orientation. For instance , with the knowledge of the locations of earthquake events and stations, the particle motion of the P-wave can be determined either by minimizing the energy on the transverse component in a selected window (e.g., Niu & Li, 2011). Alternatively, first-arrival particle motion can be investigated (e.g., Yoshizawa et al., 1999). Minimizing the receiver function energy on the transverse component can provide the orientations as well (Janiszewski & Abers, 2015). Rayleigh wave particle motions can also be used to determine the orientation of the horizontals (Doran & Laske, 2017; Stachnik et al., 2012). Finally, without using the teleseismic data, the orientations of ocean bottom seismometers can be

determined by recovering the Rayleigh wave impulse response from ambient noise cross-correlation functions (Zha et al., 2013).

Rotation from the N and E components (or 1 and 2 components, once these are determined) to the radial-tangential system that aligns with the direction of shear wave propagation is done by multiplying a vector made up of the N and E components with a rotation matrix:

$$\begin{bmatrix} R \\ T \end{bmatrix} = \begin{bmatrix} \cos\theta & \sin\theta \\ -\sin\theta & \cos\theta \end{bmatrix} \begin{bmatrix} N \\ E \end{bmatrix}$$

Where R and T are radial and transverse components, N and E are the geographical north and east components, and θ is the rotation angle, i.e. the azimuth measured clockwise from north. The R component is aligned with the great circle connecting the epicentre of the earthquake and the seismic station. It corresponds to the SV-wave polarization and is positive in the direction away from the event. In contrast, the transverse component is orthogonal to the radial component and represents SH-wave polarization. In this thesis, we used the T components to obtain SS and its precursor waveforms.

However, the vertical (Z) and the radial (R) components can have contributions from both P- and S- components, given that the rays typically arrive at some incidence angle other than vertical. Isolating the P- and S- waves can be useful for isolating these components, particularly for receiver function analyses (section 1.2.3). In comparison, the transverse component is typically purely representative of shear waves, which makes it relatively simple, i.e., generally avoiding large converted phases in the P-SV system, which is why it is often used for SS precursor imaging (e.g., Deuss, 2009; Flanagan & Shearer, 1998; Huang et al., 2019; Rychert et al., 2012b; Schmerr & Garnero, 2006; Shearer, 1993; Shearer et al., 1999)(section 1.2.4).

A transformation matrix depending on whether the seismometer is on the free surface or ocean bottom (Cerveny, 2005) can be applied to convert the seismic waveforms in the R-Z system into the P- and SV- components.

The signals from onshore stations were rotated using the transformation matrix for the free surface:

$$\begin{bmatrix} P \\ SV \end{bmatrix} = \begin{bmatrix} \dfrac{p\beta^2}{\alpha} & \dfrac{1-2\beta^2p^2}{2\alpha\eta_\alpha} \\ \dfrac{1-2\beta^2p^2}{2\beta\eta_\beta} & -p\beta \end{bmatrix} \begin{bmatrix} R \\ Z \end{bmatrix}$$

in which R and Z are the radial and vertical components, p is the ray parameter, α and β are the P- and S- wave velocities and η_x is given by $\sqrt{x^{-2}-p^2}$ $(x=\alpha,\beta)$.

For data from ocean bottom seismometers, we rotated the waveforms using the transformation matrix for the solid Earth-ocean interface:

$$\begin{bmatrix} P \\ SV \end{bmatrix} = \begin{bmatrix} \frac{p{\beta_1}^2}{\alpha_1} & \frac{1-2{\beta_1}^2p^2}{2\alpha_1\eta_{\alpha_1}} - \frac{\alpha_0\rho_0}{2\alpha_1\rho_1\eta_{\alpha_0}} \\ \frac{1-2{\beta_1}^2p^2}{2\eta_{\beta_1}} & -p\beta_1 - \frac{\alpha_0 p\rho_0}{2\rho_1\eta_{\alpha_0}\eta_{\beta_1}} \end{bmatrix} \begin{bmatrix} R \\ Z \end{bmatrix}$$

where η_x is given by $\sqrt{1-x^2p^2}$ $(x = \alpha, \beta)$, ρ is the density, and subscripts 0 and 1 correspond to α, β and ρ for the water layer and seafloor layer, respectively.

In the transformation matrix, the physical properties of media are required. A typical model for the crust is P-wave velocity = 5.5 km/s, S-wave velocity = 3.2 km/s, and density = 2900 kg/m^3. For the oceanic model, the parameters are variable as the velocities of sediments vary with their thickness. The thickness and velocity of the sediment layer beneath each station can be determined by the delay times of P-to-S conversion at the sediment-crust boundary using empirical relationships (Agius et al., 2017; Rychert et al., 2018a).

1.2.2 Deconvolution

The recorded seismogram $s(t)$, can be ideally regarded as the convolution of the earthquake source mechanism $f(t)$, the seismic instrument response $r\ (t)$, and the seismic structure of the Earth encountered by the waveform $e(t)$ (Lay & Wallace, 1995):

$$s(t) = f(t) * r\ (t) * e(t)$$

The goal of receiver function analysis or SS and precursor imaging is to recover the term $e(t)$ that represents Earth's impulse response function, essentially highlighting the seismic discontinuities in Earth's interior.

The receiver function analysis is effective for a range of scattered phases. For example, in the receiver function method, the source wave, either a P-wave or an S-wave, the parent phase, is deconvolved from the corresponding S-wave component or the P-wave daughter components of the seismogram, respectively (e.g., Ammon, 1991; Hansen & Schmandt, 2017; Kumar et al., 2011; Ligorria & Ammon, 1999; Rychert et al., 2007). Whereas, for SS precursors, the source (either a stack of the SS wave or an attenuated S wave as the daughter phase) can be deconvolved from the SS waveform.

In the time domain, this involves cutting the source phase and convolving it with the partner component at a variety of time delays to determine the impulse response of the Earth (Abers et al., 1995; Ligorria & Ammon, 1999). This approach works well and is less complicated by the potential for side lobe reverberations that can occur in frequency domain approaches. It is also stable for

individual event-station deconvolutions (Vinnik, 2019). However, it is more computationally expensive, given that multiple deconvolutions need to be performed.

Alternatively, deconvolutions can be performed relatively rapidly and simply in the frequency domain via the division of the daughter component by the source component (Bostock, 1998; Bostock & Sacchi, 1997; Langston, 1979). Simultaneous deconvolutions often use water levels to stabilise the inversions, and this approach is most effective for stabilising and analysing multiple earthquakes recorded at a single station. However, the approach is less effective for recovering stable deconvolutions from individual waveforms.

Finally, multitaper frequency-domain approaches are effective for stabilising deconvolutions of singular event-station pairs and are computationally efficient (Park & Levin, 2000). The multitaper frequency-domain technique employs Slepian tapers to reduce spectral leakage by applying frequency-dependent down-weighting to the noisier portions of the spectrum. However, the technique was originally designed and optimized to image crustal discontinuities, and the amplitude of the deconvolution functions decayed after 10 seconds. The work of Helffrich (2006) proposed an extended-time multitaper frequency domain cross-correlation method that overcame the disadvantage. The work of Rychert et al. (2012a) extended the approach to S-to-P receiver functions, and the work of Shibutani et al. (2008) further optimized the multitaper parameterizations so that the approach would be more broadly applicable for a wider range of source and dominant periods. The fact that the method is both computationally inexpensive and stable for individual waveforms makes it optimal for analysing large datasets and for performing 3-D migrations of individual waveforms to enhance resolution.

The multitaper receiver function method can be regarded as a hybrid between multitaper deconvolution and Welch's method for spectra estimation. The method windows the time series with a sequence of short, overlapping tapers over its entire length to maintain phase information. The Fourier-transformed signals for each taper are then summed to create a frequency-domain representation that preserves the phase lags for each window of the time series. Then, the standard multitaper spectral estimates are performed (Park et al., 1987; Thomson, 1982)

$$H_e(f) = \frac{\sum_{k=1}^{K} Y_w^{(k)}(f) * Y_s^{(k)}(f)}{S_0(f) + \sum_{k=1}^{K} Y_w^{(k)}(f) * Y_w^{(k)}(f)}$$

here $H_e(f)$ is the estimate of Earth's structural scheme, $Y_{w,s}^{(k)}(f)$ are the kth of K Slepian-tapered Fourier-transformed signals of wavelet waveforms or the full seismogram of converted or reflected phases, $S_0(f)$ is the spectrum estimate of the pre-event noise, and $*$ denotes the complex conjugation. A $\cos^2$ taper and normalization factor is applied to the spectrum estimate:

$$\frac{1}{N_{win}} \times \frac{N_{ft}}{N_{fc}} \times \frac{2}{N_{ft}}$$

where N_{win} is the number of summed windows, N_{ft} and N_{fc} are the numbers of the points in the Fourier-transformed signals and the $\cos^2$ taper, respectively.

1.2.3 Receiver Functions

The seismic analysis tool receiver function (RF) is commonly used in passive seismology to obtain critical insight into the inner discontinuity structure of the Earth. The RFs are derived from the seismic body wave conversions, predominately from the P- and S- waves, at seismic discontinuities in the crust and mantle, e.g., Moho, lithosphere-asthenosphere boundary and MTZ boundaries (Vinnik, 1977) (Figure 1.6). In this thesis, we mainly analyse the P-to-S conversions at two MTZ discontinuities, the 410 and the 660, i.e., P410s and P660s, to image MTZ. S-to-P conversions are not ideal for transition zone work because the conversion is not expected to be created given the slowness of S-waves that sample the transition zone region (Yuan et al., 2006).

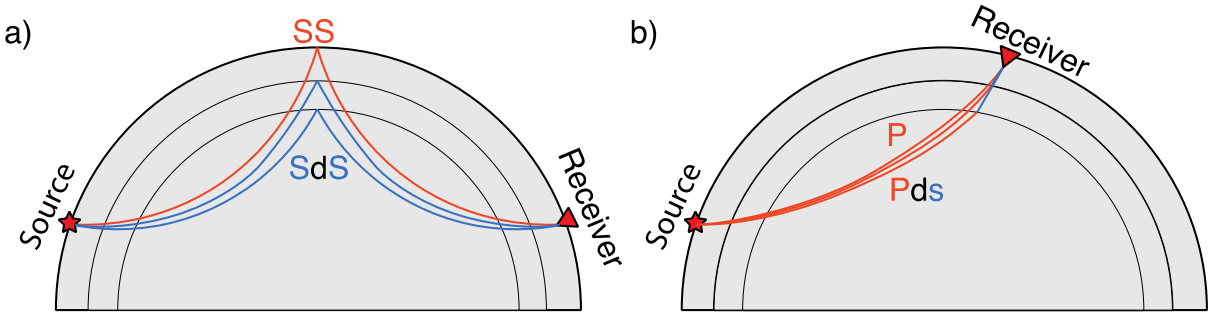

Figure 1.6 Diagrams for ray paths. a) ray paths of SS phase, S-wave reflected at the Earth's surface and its precursor SdS phase, that reflected at discontinuity d, e.g., Moho, the 410 and the 660. b) ray paths of direct P phase, and Pds phase, that P-wave converted to S-wave at discontinuity d.

Most seismic observations usually require a network of seismographs. For example, the implementation of seismic tomography relies on seismic data from different angles and with intersections sampling the structure; thus, a seismic station network of good coverage is required (Nolet, 1987). Nevertheless, receiver functions can be applied to a network of stations or just to a single station. In fact, with a good geographical distribution of seismic sources (earthquakes), the receiver functions of a single station can constrain the subsurface structure under the station and its vicinity within a certain distance (e.g., Kawakatsu et al., 2009; Rychert et al., 2005b). Analysing these converted phases, e.g., P410s (P-waves converted to S-waves at the 410) and P660s (P-waves converted to S-waves at the 660), provides the precise depths of those boundaries, the seismic velocity contrast between layers above and below, the sharpness of the velocity gradient at the discontinuity, and the topography on the discontinuity.

Converted P-to-S phases are of much smaller amplitudes than the primary P-waves and may not be easy to distinguish from the background noise in a single waveform. In practice, stacking many signals is required to resolve discontinuity structure. Stacking RFs is possible because of the deconvolution, which eliminates variability and complexities in a typical seismogram, e.g., from variations in the focal mechanism, back-azimuth, and/or instrument response.

Receiver functions are often calculated using seismic data from teleseismic events and earthquakes with epicentre between 35 degrees to 80 degrees from the seismic station. The incident waveforms from such distances arrive at near angles vertically beneath the stations. The simplest approach to calculating receiver functions is to deconvolve the Z components from the R components. However, rotation to the theoretical P-wave and SV-wave polarization directions can better partition the energy between the source and receiver (e.g., Agius et al., 2017; Agius et al., 2021; Rychert et al., 2012a; Rychert et al., 2014a; Rychert et al., 2013; Rychert et al., 2010). Therefore, the deconvolution of the P-wave components from the S-wave components can provide enhanced imaging capabilities in comparison to using the R and Z components (Shearer, 2019).

In addition, the phases are primarily sensitive to changes in shear wave velocity with depth, with little sensitivity to density (the other component of impedance contrast). In addition, these phases have sensitivity to discontinuity structure beneath seismic stations, and given station distributions, mostly available beneath continents.

P-to-S receiver functions have been particularly useful for imaging the Moho. The relatively high resolution provided by these phases makes them particularly useful for imaging locations where the crust is very thin, for example, beneath the oceans (e.g., Hung et al., 2021; Zhang & Olugboji, 2023) or where crustal thickness varies dramatically, e.g., beneath the subduction zones (e.g., Kim et al., 2021; Kim et al., 2012; Rychert et al., 2018a) or continental rifts (e.g., Dugda et al., 2005; Hodgson et al., 2017; Rychert et al., 2012a). Receiver functions have been applied to study subduction zones. Receiver functions are used to reveal the depth of subducting slabs (e.g., Wang et al., 2024), the geometry of slabs (e.g., Cheng et al., 2017) and the nature of the overlying mantle wedge. P-to-S receiver functions have been performed to detect the seismic lithosphere-asthenosphere boundary (e.g., Abt et al., 2010; Kumar et al., 2012; Rychert & Shearer, 2009; Rychert et al., 2010). However, overall, S-to-P receiver functions provide better resolution at lithosphere-asthenosphere boundary depths since they are not contaminated by reverberated phases from shallow, crustal discontinuities (Rychert et al., 2012a; Rychert & Harmon, 2016).

Receiver functions imaging of MTZ discontinuities has been very successful in terms of constraining detailed mantle dynamics. Lawrence and Shearer (2006) have depicted the global MTZ thickness maps using receiver functions. The long-wavelength features provide a general view and knowledge that the MTZ is thickened beneath the subduction zone and thinned beneath oceans. The

receiver functions can achieve a particularly fine resolution that they are more commonly used to image small-scale lateral variations in regional studies. For instance, Agius et al. (2017) applied receiver function analysis to stations in Hawaii and imaged a thin MTZ below north-central Hawaii surrounded by a thick zone. A possible non-vertical plume and adjacent mantle downwellings in the upper mantle are inferred by imaged the 410 and the 660 topography variations. It suggests complex plume dynamics. Since the receiver functions have a lateral resolution of ~150 – 200 km, regional studies can provide comprehensive observations that implement or challenge the conventional assumptions. For example, both depressed 410 and 660 are found by receiver functions beneath Iceland, a major acknowledged plume (Jenkins et al., 2016). The depressed bottom of the transition zone suggests a hot anomaly extends to at least the 660 beneath Iceland and a garnet-dominant phase transition as opposed to olivine's. A thin mantle transition zone has also been observed beneath the equatorial Mid-Atlantic Ridge by receiver functions (Agius et al., 2021), suggesting upwellings could happen more prevalently than previously thought, at least beneath slow-spreading ridges.

1.2.3.1 This Thesis

Signal-to-noise ratio (SNR) is a way used to quantify the quality of a waveform. The SNR of a waveform for P-to-S receiver function analysis was measured by the ratio of the average amplitude of the P-wave component in a 20-second-long window from the predicted P-wave arrival time and the average amplitude in a 20-second-long window 60 seconds earlier than the predicted P-wave arrival. For data from onshore stations, it's a practical way to select data with an SNR higher than a certain value, e.g., 2 is used in Chapter 2. Sometimes, visual inspection is required, especially for OBS data, which is rather noisier yet precious (e.g., Agius et al., 2017; Agius et al., 2021; Rychert et al., 2018a).

Seismic records from offshore stations are normally noisier compared to land data due to the complex oceanic environment. Loading from long-wavelength infragravity ocean waves at the water surface would cause the deformation of the seafloor as the response. It would produce compliance noise that contaminates the seismic records (Crawford & Webb, 2000). Another major noise that affects the OBS seismic records is the tilt noise. It is caused by the bottom currents acting on the OBS (Crawford & Webb, 2000). Removing the two kinds of noise benefits most of the seismology studies. The compliance noise can be corrected via a transfer function between the vertical component and the pressure record (Crawford & Webb, 2000). The tilt noise can be removed by applying a transfer function between the vertical and the two horizontal components sequentially (e.g., Crawford & Webb, 2000) or between the vertical and the calculated maximum horizontal direction of the tilt noise (e.g., Bell et al., 2015).

However, the frequency band applied in the corrections is 0.005 to 0.03 Hz (Bell et al., 2015), below the frequency band used for the MTZ study, i.e. 0.05 – 0.2 Hz. The compliance and tilt noise corrections from the OBS data are not necessary for receiver functions study on the MTZ. Agius et al. (2021) have shown that they don't have significant effects on P410s and P660s. The receiver functions of ocean-bottom stations may also suffer from strong reverberations, especially for imaging the shallow structure, due to the existence of water and sediment layers (Kim et al., 2021). Yet the reverberations are less likely to affect the MTZ phases (Chapter 2), as previous studies have shown (e.g., Agius et al., 2017; Agius et al., 2021).

In a seismogram, the P-wave is the first arrival, and the P-to-S conversion arrives at a later time given the slow travel times of S-waves in comparison to P-wave. The differential arrival times of the primary phase and converted phases provide estimates of the depth of discontinuities, and relative amplitudes provide estimates of seismic properties contrasts (e.g., Julià, 2007; Rychert & Harmon, 2016). Seismic arrivals can be traced back to image discontinuity depths using an assumed seismic migration model. This inherently imparts some degree of uncertainty. However, testing the effects of various migration models can be performed to quantify these effects and lend support for the interpretation of the data. In addition, station elevation corrections and sedimental corrections should also be considered, especially in an amphibious environment, e.g., Cascadia (Chapter 2). In a dense seismic station network, such as that in Cascadia, receiver functions can then be staked, as is the case for this study, onto a 3-D grid with a lateral spacing of 1 degree by 1 degree and a vertical interval of 1 km (e.g., Agius et al., 2017; Rychert et al., 2013). A smoothing operator with a radius determined by the Fresnel zone of the waveform is applied to the stacking.

1.2.4 SS and its Precursors

An SS wave is an S-wave generated by a seismic event that has reflected once at the surface of the Earth near the midpoint of the ray path between the source and receiver (Choy & Richards, 1975). SS precursors are SS waves that are reflected at deeper seismic velocity and density discontinuities than the surface and arrive before the main SS phase due to their shorter ray path (Figure 1.6, 1.7). SS precursors are generally denoted as SdS, where d is the discontinuity depth that precursor was generated. The utility of SS precursors is that they are sensitive to the bounce point region and, therefore have sensitivity to discontinuity structure in regions where station coverage is sparse.(Lawrence & Shearer, 2008)

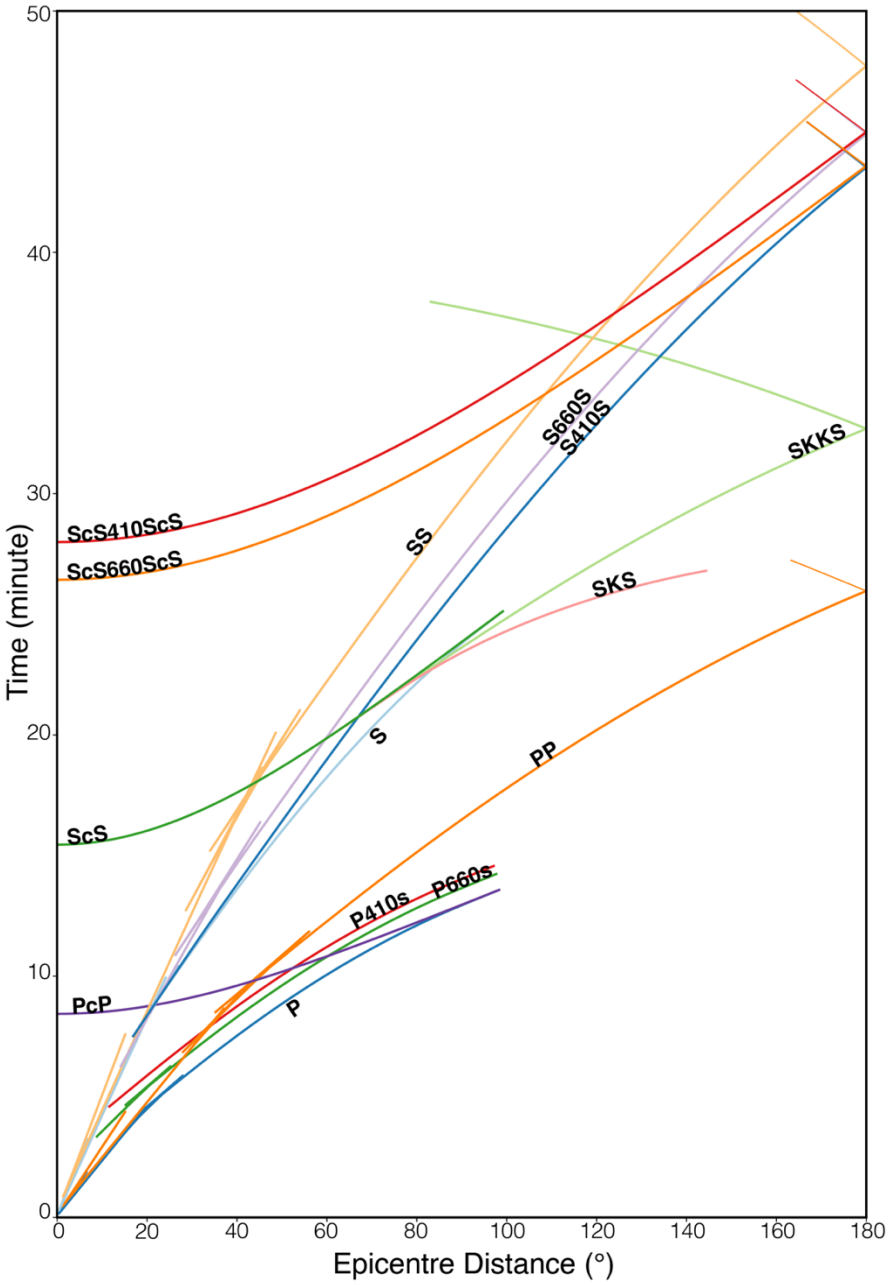

Figure 1.7 Theoretical travel time. Travel time of several body phases used or with notable effects in this study. The travel times are calculated using 1-D reference Earth model IASP91 with a source depth of 0 km.

SS precursors are measured on the transverse component, corresponding to horizontally polarized shear waves. SS precursors are underside reflections and, therefore have sensitivity to the impedance contrast at a seismic discontinuity, i.e. the shear velocity contrast and density contrast. Given the distribution of earthquakes and global seismic station coverage, the entire Earth is illuminated by a least hundreds of SS bounces (Figure 1.3), allowing imaging even in the remote ocean basins. Taking advantage of the SS and its precursor sampling, the observed seismic records can provide excellent global coverage. However, SS precursors are relatively long-period waveforms, with periods of ~15 s (Rychert & Shearer, 2010a). This means that the waveforms have relatively wide lateral resolution, on the order of 15 degrees (Shearer, 1993). Narrow, small-sized topographic

anomalies are effectively diminished due to the size of the SS Fresnel zone (Shearer et al., 1999). In addition, the SS precursor Fresnel zone shape is not simple, instead resembling a saddle (Dahlen & Tromp, 1999; Lawrence & Shearer, 2008; Tharimena et al., 2016). However, this can be simplified/mitigated somewhat by stacking waveforms from event-station pairs from a variety of azimuths (Tharimena et al., 2016).

Acceleration seismograms have been considered to minimize waveform interference and emphasize high-frequency features. Bin stacks of acceleration seismic waveforms were used to detect the lithosphere-asthenosphere boundary depths beneath the Pacific (Schmerr, 2012). To image shallow reflectors associated with the Moho and the lithosphere-asthenosphere boundary, an approach deconvolving the SS phases from itself before migrating and stacking in bins has been performed beneath Asia (Heit et al., 2010). Waveform modelling on the sidelobes of the stacked SS waveforms was performed to image the shallow discontinuities (Rychert & Shearer, 2010a). Synthetic waveforms were generated by convolving a reference SS stack with impulse operators corresponding to various discontinuity depths and characteristics, with the optimal discontinuity identified through a grid search approach. Alternatively, waveform modelling on the sidelobes of the stacked SS waveforms is applied to image lithospheric discontinuities (Rychert & Shearer, 2010a). A reference SS phase stack is convolved with impulse operators corresponding to a range of discontinuity depths and properties to construct synthetic waveforms. A grid search approach is then used to determine the best-fitting discontinuity. This approach has been applied to image the lithosphere-asthenosphere boundary beneath the Pacific (Rychert & Shearer, 2011) and mid-lithosphere discontinuity beneath the Ontong Java Plateau (Tharimena et al., 2016). The lithospheric structures beneath the Pacific (Tharimena et al., 2017b) and cratons (Tharimena et al., 2017a) have been imaged using a similar modelling method but with a differential evolution algorithm (Price et al., 2005; Storn & Price, 1997) that minimized the model storage size and computation time at the same time in comparison to a typical grid search.

For studies using SS and its precursors, the earthquake source depths are usually limited to no more than 75 km (Flanagan & Shearer, 1998; Rychert & Shearer, 2011; Rychert et al., 2010) to avoid interferences from depth phases. The epicentral distance of data is another factor that affects the quality of SS and precursor waveforms, considering the contaminations from other phases. A window of 90 – 180 degrees is generally applied in SS and its precursor studies (e.g., Deuss, 2009; Rychert & Shearer, 2011; Shearer et al., 1999).

Deep mantle discontinuities are most commonly imaged by the SS precursors. The velocity and density contrasts across the 410 and the 660 produce notable underside reflections, referred to as S410S and S660S, respectively. However, the amplitudes of SS precursors are typically ~ 5 - 10% of the amplitudes of the corresponding SS phase due to the fairly weak discontinuities (less than 10%).

Such small amplitudes are not significant out of the background noise and are hardly visible in a single waveform, even after properly filtering. Therefore, imaging using SS precursors requires stacking a large number of seismic signals to suppress the noise and highlight the precursors. It's typical to stack data sharing close geographical locations of SS bounce points and to obtain the global maps of the MTZ topography, e.g., the global map of the 410 depths (e.g., Chambers et al., 2005) and the 660 depths (e.g., Shearer & Masters, 1992).

Clear S410S and S660S phases have been observed in global body wave stacks of data from the Global Digital Seismograph Network over a 5-year-long period (Shearer, 1990). With the increasing deployments of seismic stations, the coverage of the SS bounce points is improving, and the density of sampling is rising.

The absolute travel times of the SS and precursors to it are affected by the velocity structure along their long ray paths. Nevertheless, the SS precursors that are reflected at the MTZ boundaries are almost identically affected by the upper mantle heterogeneity. The differential travel times of the S410S and S660S are relatively robust regardless of the assumptions of velocity models (Chapter 4). More often, the global maps of MTZ thickness derived from the differential travel time are reported (e.g., Gossler & Kind, 1995; Gu & Dziewonski, 2002).

The global topography maps of the 410, the 660 discontinuities, as well as the thickness of MTZ have been obtained using SS and its precursors (e.g., Deuss, 2009; Flanagan & Shearer, 1998; Gu et al., 1998; Houser et al., 2008; Shearer, 1993).

Regional MTZ topographies studies with the concentrations of SS bounce points have been conducted, for instance, beneath the Pacific (e.g., Cao et al., 2011; Lee & Grand, 1996; Niu et al., 2002; Schmerr & Garnero, 2006; Yu et al., 2017; Zheng et al., 2015) and beneath Asia (e.g., Heit et al., 2010; Lessing et al., 2014; Tauzin et al., 2018). Except for the depths, studies using those reflection phases have also been used to reveal the impedance contrast at MTZ discontinuities, e.g., the reflectivity of the 410 (Chambers et al., 2005). Benefiting from massive amounts of seismic stations deployed globally in the past decades, the SS and precursors have given critical constraints on seismic anisotropy in MTZ (Huang et al., 2019).

Conventionally, studies of MTZ imaged by the SS precursors are more focused on the connections between thermal anomalies and topography perturbations. Recently, with the increase of seismic records and improvement of data processing and imaging techniques, the SS precursors imaging could bring forth more subtle details of MTZ. Analyses of the amplitude variation of the S410S and S660S compared to SS have inferred a poorly mixed mantle and suggested a ~ 4% basalt fraction in the bottom of the MTZ (Waszek et al., 2021; Yu et al., 2023).

Besides the 410 and the 660, the nuanced nature of MTZ can be informed by the SS and precursor signals. The global stacking of SS precursors has provided evidence of a discontinuity within the MTZ, namely the 520-km discontinuity (Shearer, 1990). Moreover, SS precursors have presented another discontinuity, the 560, within the MTZ with its global geographical distribution (Deuss & Woodhouse, 2001; Tian et al., 2020). A sporadic low-velocity layer atop the MTZ beneath the Pacific is also revealed by strong negative sidelobes of SS precursors (Wei & Shearer, 2017).

SS precursors reflected from other mantle discontinuities have been imaged as well. A 4000 – 5000 km-wide discontinuity at around 950 – 1050 km has been imaged beneath the Pacific by applying reverse-time migration full-waveform imaging to SS precursor data (Zhang et al., 2023). At shallower depths, additional mantle discontinuities have been imaged by SS precursors, such as the Lehmann discontinuity at 220 km and the X-discontinuity around 250 – 350 km (Deuss & Woodhouse, 2004).

Discontinuities in the lithosphere have also been investigated by the SS and/or its precursors. The depths of the lithosphere-asthenosphere boundary have been measured by picking the corresponding phases directly from acceleration seismograms (Schmerr, 2012) or by matching waveform modelling beneath the Pacific (e.g., Rychert & Shearer, 2011; Tharimena et al., 2017a; Tharimena et al., 2017b). SS precursors can reveal the seismic anisotropy in the mantle (e.g., Huang et al., 2019; Rychert et al., 2014b). The SS precursor modelling has also imaged the mid-lithosphere discontinuities (e.g., Tharimena et al., 2017a; Tharimena et al., 2016) and the Moho (e.g., Rychert & Shearer, 2010a).

1.2.4.1 This thesis

SS phases are Hilbert transformed relative to the *S* phases (Choy & Richards, 1975). Taking this concept, the SdS precursors produced by internal discontinuities can be separated from the main SS phases by deconvoluting stacked source *S* phases from Hilbert-transformed *SS* phases. The reference S source for each event is constructed by stacking S phases from individual waveforms. S waveforms with signal-to-noise ratios no larger than 2.8 are generally rejected for their poor quality. S phases are automatically identified as the maximum positive or negative amplitude pulse within a 20-second window centred on the theoretical S phase arrival time. The S phase signals are then stacked and normalised to standardise amplitude. They are trimmed to a 40-second window centred on the picked S phase, resulting in the S wavelet for the corresponding event.

A lowpass of 1 Hz or a bandpass of 0.02 to 0.5 Hz are commonly applied to waveforms. The signal-to-noise ratio of an SS waveform is calculated as the ratio of the maximum amplitude of the seismic phase to the standard deviation in a time window of 270 seconds to 30 seconds preceding

the *SS* pulse. Data with SNR larger than 3 are normally of good quality and used in further studies (Chapter 3, Chapter 4).

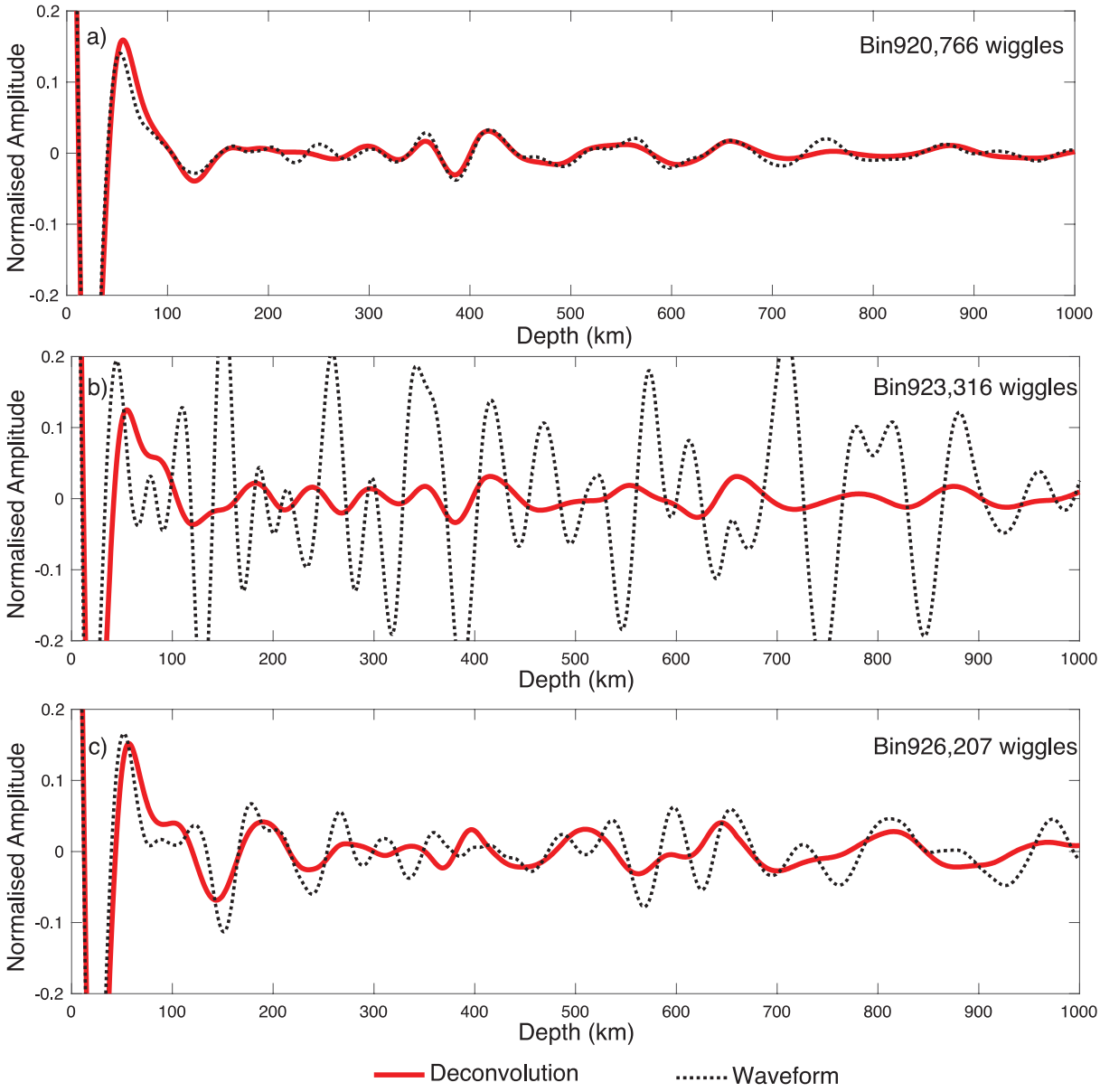

Figure 1.8 Comparison of SS precursors imaging approach. a) – c) Stackings of SS waveforms (dashed black dashed lines) and deconvolutions (solid red lines) of bins 920, 923, 926, located in South America and the adjacent area. The bin index and number of stacked wiggles are shown at the top right corner.

The S wavelet of the corresponding event is deconvolved from each SS and its precursors using an extended time multitaper frequency domain deconvolution (Helffrich, 2006; Rychert et al., 2012b).

The impulse response produced by deconvolutions is converted from the time domain to the depth domain with assumed seismic velocity models. Data with bounce points within 10 degrees from the bin centre are stacked to represent the structure beneath the geographical bin. Depths of discontinuities are measured as the locations of peaks of corresponding phases.

Introducing a sophisticated deconvolution method allows the application of SS and precursor analysis on rather weak signals and improves the resolution (Figure 1.8).

1.2.5 Thermal Anomaly Estimate

As stated above, the solid-state phase transitions of minerals, especially the olivine, the most abundant mineral in the upper mantle, are normally thought to contribute to the seismic wave speed increases at the 410 and the 660. Those phase changes are sensitive to pressure and temperature. Therefore, the topographies of MTZ are commonly regarded as thermometers that reflect the thermal conditions of the MTZ (Bina & Helffrich, 1994; Deuss, 2009). Quantitative estimates of thermal anomalies revealed by MTZ topographies have been made by assuming certain values of Clapeyron slope in Chapter 2 or by marching the predictions from thermodynamic modelling in Chapter 4. In this thesis, the discussions about thermal anomalies are mainly based on the classical paradigm, i.e., a positive Clapeyron slope for the 410 and a negative Clapeyron slope for the 660. A previous MTZ study has proposed the global mantle temperature ranges between 1300 -1900 K (Waszek et al., 2021), where the classic paradigm is sufficient to represent the variations of the MTZ topographies as we don't consider amplitudes here.

1.2.5.1 Clapeyron Slopes

In a simplified model, different Clapeyron slopes are generally used to represent the linear characteristics of those mineral phase transformations (Figure 1.2a). Clapeyron slopes specify the temperature dependence of pressure. The Clapeyron slopes are positive for phase changes at the 410 and the 520, and negative at the 660. However, the slope for each transition varies a lot from different experimental predictions. Akaogi et al. (1989) reported a Clapeyron slope of 1.5 MPa/K for the olivine and wadsleyite transformation, while Katsura et al. (2004) reported a much higher slope of 4 MPa/K. A range of values from 2.1 to 3.6 MPa/K have also been reported (e.g., Bina & Helffrich, 1994; Katsura & Ito, 1989; Morishima et al., 1994; Yonggang et al., 2008). The Clapeyron slopes of the wadsleyite changing into ringwoodite are steeper, and values from 2.8 to 7 have been proposed (e.g., Hernández et al., 2015; Inoue et al., 2006; Katsura & Ito, 1989; Suzuki et al., 2000; Yonggang et al., 2008). For the transformation from ringwoodite into bridgmanite and ferropericlase, the Clapeyron slopes have been suggested to vary from steep, around -4 MPa/K (e.g., Hernández et al., 2015; Ito et al., 1990), to intermediate values, -3.1 to -2.5 MPa/K (Ghosh et al., 2013; Hirose, 2002; Ye et al., 2014), to -1.3 or even -0.5 MPa/K (e.g., Fei et al., 2004; Ghosh et al., 2013; Katsura et al., 2003; Litasov et al., 2005). The choice of the Clapeyron slopes notably affects the estimate of thermal anomalies derived from the MTZ topographies and the understanding of MTZ.

1.2.5.2 Thermodynamic Modelling

Thermodynamic modelling is used to estimate compositions, i.e. mineral assemblages and material properties, using constraints from high-pressure-high-temperature experiments. It is normally used to map the stability fields for given bulk compositions under mantle conditions and obtain the densities and elastic moduli, and thus seismic properties of proposed MTZ compositions.

Pyrolite is the theoretical composition of the Earth's upper mantle based on melting models, compositions of meteorites and the least-differentiated mantle peridotite samples at the surface (Ringwood, 1975). It is commonly used in thermodynamic modelling for the MTZ. Thermodynamic modelling and mineral elastic properties datasets have been reported (e.g., Ritsema et al., 2009; Stixrude & Lithgow-Bertelloni, 2011; Xu et al., 2008). Using slightly different pyrolytic compositions does not affect the phase diagram notably (Waszek et al., 2021). With the assumption that the chemistry of the mantle is fully equilibrated, phase assemblages are obtained via Gibbs free energy minimisation (Connolly, 2005). The thermodynamic modelling shows a nearly linear relationship between temperature and pressure, i.e., depth, for olivine to wadsleyite and wadsleyite to ringwoodite. However, at the bottom of the transition zone, it becomes more complicated. The endothermic transition of ringwoodite into bridgmanite and ferropericlase (Bina & Helffrich, 1994) dominates when the temperature is less than 2000 K. At higher temperatures, the transformation of majoritic garnet to Al-bearing Mg-rich bridgmanite with a positive Clapeyron slope plays a greater role in determining the mantle properties (Jenkins et al., 2016) (Figure 1.9).

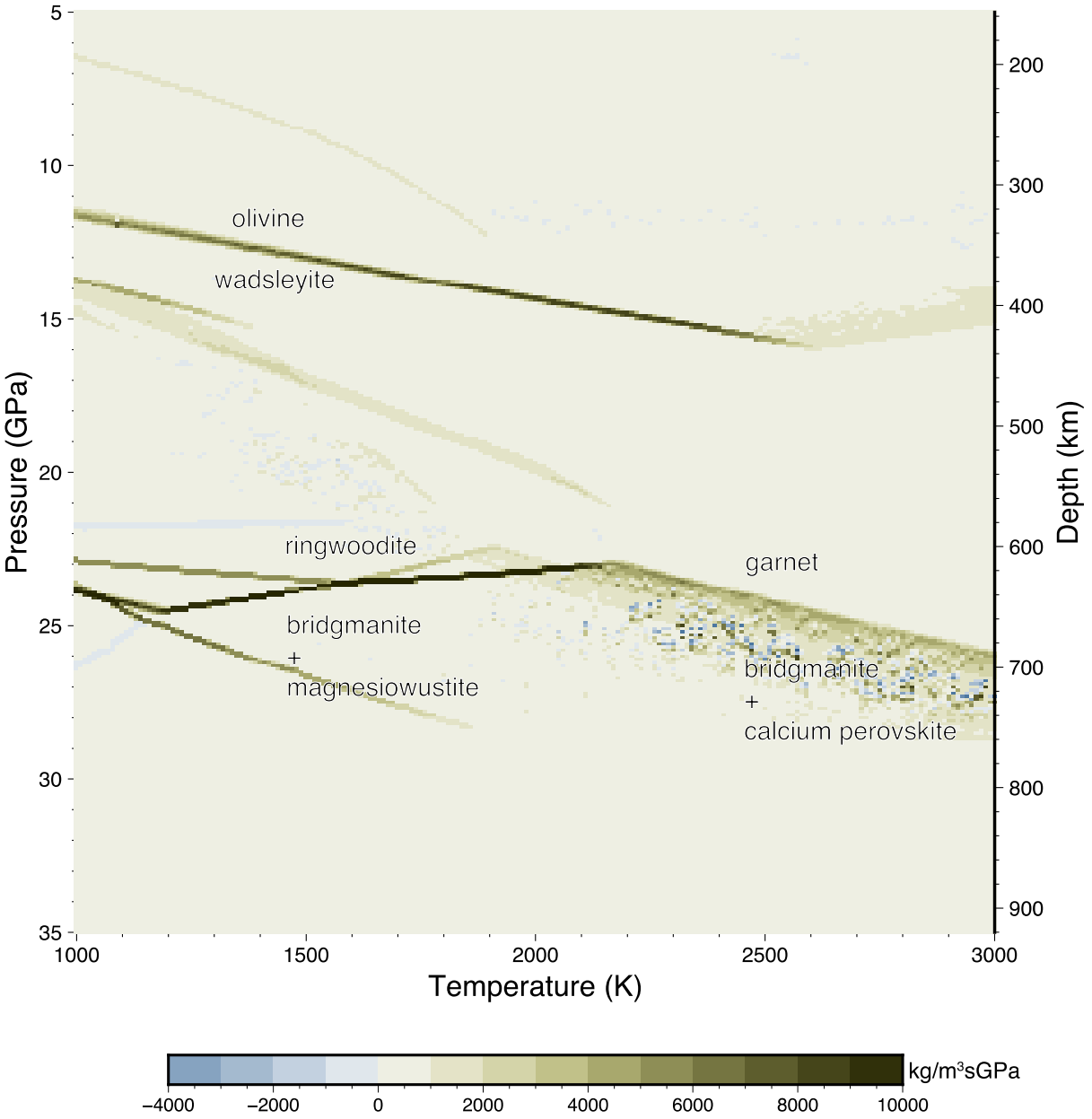

Figure 1.9 Seismic impedance gradient. Seismic impedance (the product of shear velocity and density) gradient obtained by thermodynamic modelling of an equilibrium assemblage of pyrolite with weight 45.5% of SiO2, 38.3% of MgO, 7.18% of FeO, 3.98% of Al2O3, and 3.57% of CaO (Baker & Stolper, 1994). Perple_X code (Connolly, 2005) is used for computation to minimise Gibbs free energy with thermodynamic formalism and mineral elastic properties database from Stixrude and Lithgow-Bertelloni (2011).

In addition to the pyrolite equilibrium assemblage mantle model, mechanical mixture models (Christensen & Hofmann, 1994; Morgan & Morgan, 1999) have also been suggested and perhaps preferred over pyrolite compositions of the mantle based on amplitude observation of SS precursors (e.g., Waszek et al., 2021; Yu et al., 2023). The mixture of harzburgite (pyrolite depleted by upper mantle melting) and basalt combined in proportions to have the same bulk composition as pyrolite may be generated by differentiation that has occurred at mid-ocean ridges and then recycled back into the mantle at subduction zones (Hacker et al., 2011; Ringwood, 1991). The amplitudes of the

S410S and S660S phases are sensitive to the basalt fractions. A fraction of 0.3 – 0.4 is suggested by fitting the precursor observations to the mechanical mixture models (Waszek et al., 2021; Yu et al., 2023). The relationship between observed precursor amplitudes and compositional anomalies is out of the scope of this thesis but will be considered in future work. Nevertheless, the depths of the MTZ boundaries are consistent among the equilibrium assemblage model and mechanical mixture models with basalt fractions smaller than 0.6 (Waszek et al., 2021; Yu et al., 2023).

1.3 Outline of this Thesis

The focus of this thesis is to image and investigate the mantle transition zone using receiver functions and SS precursors at high resolution. The observations cover the Cascadia, which has various unique tectonic environments, with high lateral resolution, and the whole global MTZ with excellent long-period data coverage. It also includes the use of unique oceanic bottom seismic records and the inclusion of a high number of SS precursor records for increased global resolution.

This work is constructed as a “three-paper thesis” with three major chapters. Chapter 2 presents the MTZ beneath the Cascadia imaged by receiver functions using an amphibious dataset. Chapter 3 introduces the development of an SS precursor method that is validated by comparison to CRUST1.0 and demonstrates its utility for imaging shallower discontinuities compared to most traditional studies. Chapter 4 implements the SS precursor method developed in Chapter 3 on the global database to image the MTZ.

Chapter 2 Seismic imaging beneath Cascadia shows shallow mantle flow patterns guide lower mantle upwellings

2.1 Abstract

The mantle transition zone plays an important role in modulating material transport between the upper mantle and the lower mantle. Constraining this transport is essential for understanding geochemical reservoirs, hydration cycles, and the evolution of the Earth. Slabs and hotspots are assumed to be the dominant locations of transport. However, the degree of material transport in other areas is debated. We apply P-to-S receiver functions to an amphibious dataset from Cascadia to image the mantle transition zone discontinuities beneath mid-ocean ridges, a hotspot, and a subduction zone. We find a mantle transition zone thinned by 10 ± 6 km beneath the ridges and by 8 ± 4 km behind the slab, closely resembling the 660 discontinuity topography. Depressions on the 410 discontinuity are smaller, 5 ± 2 km on average, focused in the north and the south and accompanied by supra-410 discontinuity melt phases. The depressions occur away from locations of uplifted 660 discontinuity, but near slow seismic velocity anomalies imaged in the upper mantle. This suggests lower mantle upwellings occur beneath ridges and slabs but stall in the transition zone, with upper mantle convection determining upward material transport from the transition zone. Therefore, upper mantle dynamics play a larger role in determining transfer than typically assumed.

2.2 Introduction

The mantle transition zone (MTZ) is the region between the upper mantle and lower mantle bounded by two seismic discontinuities at approximately 410 km (the 410) and 660 km (the 660) (Dziewonski & Anderson, 1981). These are typically interpreted as the pressure-induced transformation of olivine grains into denser crystal structures, as predicted by laboratory experiments: α olivine to β-spinel (wadsleyite) at ~410 km and ringwoodite to bridgmanite and magnesiowüstite at ~660 km (Ringwood, 1975). The MTZ is arguably one of the most important parts of the Earth for understanding its evolution and behaviour because: 1) any material moving between the upper and lower mantle has to pass through the MTZ, 2) the MTZ has the capacity for storing huge amounts of water, several oceans worth (Hirschmann & Dasgupta, 2009), and 3) the top of the MTZ (and/or the shallow lower mantle) may be a region of widespread deep melts (Bercovici & Karato, 2003; Schmandt et al., 2014), which may act as geochemical reservoirs and/or alter mantle viscosity.

It is typically assumed that material transfer between the upper and lower mantle occurs where hotspots upwell vertically and where subducting plates descend vertically or sub-vertically. Seismic tomography models also find slow velocities interpreted as ascending material beneath hotspots and fast velocities associated with descending material beneath subduction zones (Nolet et al., 2007). Seismic imaging of MTZ discontinuities generally reflects mineral physics predictions for thickening beneath subduction zones and thinning beneath hotspots (Gu & Dziewonski, 2002; Houser et al., 2008; Lawrence & Shearer, 2006; Lawrence & Shearer, 2008).

Several lines of geochemical evidence suggest greater complexity than large, long-lived full mantle convection, or in other words, a well-mixed mantle. These include isotopic differences between ridges and hotspots and bulk compositional discrepancies between the predictions and observations of Earth's interior layering and atmosphere (Hofmann, 1997). Possible explanations include pockets of enrichment, chemical piles, layering of stagnant slabs (Ballmer et al., 2015; Jellinek & Manga, 2004; Kellogg et al., 1999; Marquardt & Miyagi, 2015; Morgan & Morgan, 1999), or stable high-viscosity lower-mantle convective cells (Ballmer et al., 2017). Alternatively, the mantle may pervasively rise across the MTZ, but typically be compositionally filtered during the process (Bercovici & Karato, 2003). Although more intricate convection and alternative locations of material transfer across the MTZ may be implied by these conceptual models, tight constraints have remained elusive.

Seismic observations have also been used to argue for greater complexity than the simple vertical ascent of material beneath hotspots. Deflected upwellings or tree-like upwelling structures have been inferred from global seismic tomography images (French & Romanowicz, 2015; Tsekhmistrenko et al., 2021). Imaged slow velocity regions or MTZ thinning have been interpreted as material upwelling from the lower mantle in alternative locations away from hotspots (Agius et al., 2021; Suetsugu et al., 2006). However, it has also been suggested that some of the observations may also be related to nearby plume material (Portner et al., 2017; Zhao et al., 2013) or be artefacts of tomographic inversion (Bezada et al., 2016).

Several studies have found seismic phases interpreted as conversions from a melt layer just above the MTZ. This is thought to be the result of hydrated material that upwells through the MTZ, but melts when it enters the lower water solubility conditions shallower than the MTZ. However, the phases have been used to link the presence of a melt layer to a variety of different tectonic environments (Hier-Majumder et al., 2021; Revenaugh & Sipkin, 1994; Song & Kim, 2011; Vinnik & Farra, 2007) and also to suggest the presence/absence of the melt layer is sporadic without necessarily having a tectonic correlation (Tauzin et al., 2010; Wei & Shearer, 2017).

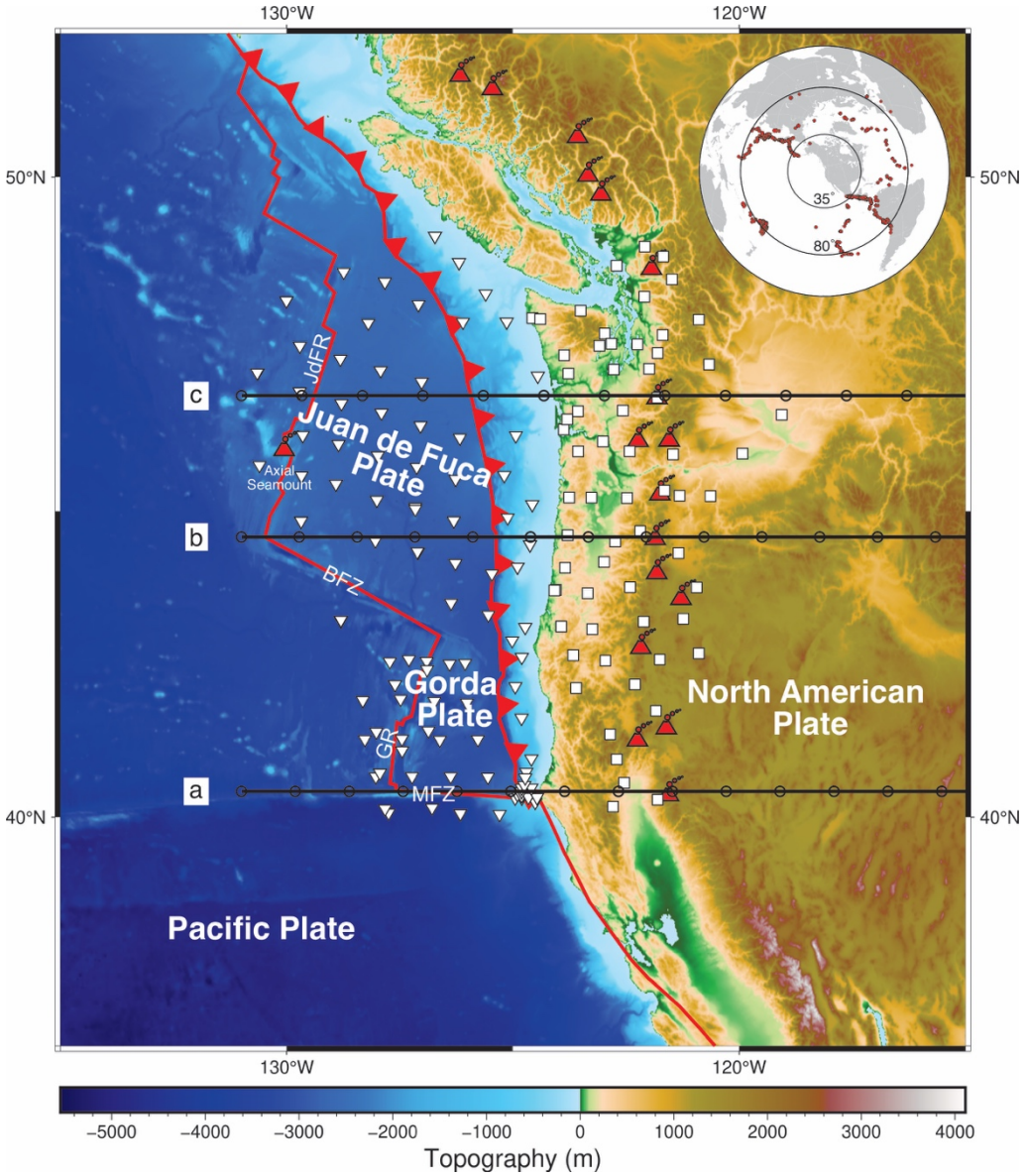

Figure 2.1 Map of the study area. The background shows bathymetry/topography. White inverted triangles represent seismometer locations offshore and white squares represent seismometer locations onshore. Red volcano symbols indicate the locations of major volcanos of the Cascadia Arc and the Axial Seamount (the active volcano associated with the Cobb Hotspot), which is on the Juan de Fuca Ridge. Thick red lines show plate boundaries, and the serrated line shows the trench. Three thick black lines represent the locations of the cross sections in Figure 2.4 and Figure 2.6. Black circles along the cross sections correspond to a spacing of 100 km. The inset map shows the locations of earthquakes (red circles) used in this study. Juan de Fuca Ridge (JdFR), Blanco Fracture Zone (BFZ), Gorda Ridge (GR), and Mendocino Fracture Zone (MFZ) are as labelled.

High-resolution in situ imaging of MTZ discontinuities provides independent and tight constraints on material transfer and melt layering. Yet, this imaging has proven challenging given that most seismic stations are located on land, i.e., limited to ~30% of Earth's surface, and typically away from many tectonic regions of interest.

The Cascadia subduction zone lies in the northeastern Pacific where the Juan de Fuca and Gorda Plates subduct beneath the North American Plate (Figure 2.1). The Cascadia Initiative experiment deployed an amphibious seismic array from the intermediate spreading Juan de Fuca and Gorda Ridges, including the Cobb Hotspot, to the Cascadia arc and backarc region (Toomey et al., 2014) offering an excellent opportunity to investigate material transfer at a range of tectonic environments. Body wave tomography images high-velocity slabs descending to MTZ depths and slow velocities in the upper mantle beneath the slabs (Bodmer et al., 2018). However, connections between these shallow mantle dynamics, the MTZ, and the lower mantle have yet to be investigated. Here we image the MTZ discontinuities beneath the Cascadia region using P-to-S (Ps) receiver functions (RF)s from an amphibious dataset and compare the variations of these discontinuities and MTZ thickness with the seismic velocity anomalies.

2.3 Data and Methods

2.3.1 Receiver functions

In this study, we used an amphibious dataset recorded by 202 stations including 136 ocean bottom seismometers (OBS)s and 66 onshore instruments. The data were collected by the Cascadia Initiative (OBSIP, 2011), USArray Transportable Array (Array, 2003), the Pacific Northwest Seismic Network (Washington, 1963), Berkeley Digital Seismic Network (Center, 2014), and the United States National Seismic Network ((ASL)/USGS, 1990). We used earthquakes of magnitudes greater than 5.5 Mw with epicentral distances between 35° and 80° that happened during the deployment period of the Cascadia Initiative experiment (Figure 2.1). These initial parameter cut-offs resulted in seismograms from 29683 event-station pairs.

The seismograms located on land were rotated into the P- and S-wave components using a transformation matrix (Cerveny, 2005) for the free surface :

$$\begin{bmatrix} P \\ SV \end{bmatrix} = \begin{bmatrix} \frac{p\beta^2}{\alpha} & \frac{1-2\beta^2p^2}{2\alpha\eta_\alpha} \\ \frac{1-2\beta^2p^2}{2\beta\eta_\beta} & -p\beta \end{bmatrix} \begin{bmatrix} U_R \\ U_Z \end{bmatrix}$$

where U_R and U_Z are the radial and vertical components, p is the ray parameter, α and β are the P and S wave velocities, and η_x is given by $\sqrt{x^{-2}-p^2}$ $(x=\alpha,\beta)$. Stations located on the seafloor were rotated using the transformation matrix for the solid Earth-ocean interface:

$$\begin{bmatrix} P \\ SV \end{bmatrix} = \begin{bmatrix} \frac{p\beta_1{}^2}{\alpha_1} & \frac{1-2\beta_1{}^2p^2}{2\alpha_1\eta_{\alpha_1}} - \frac{\alpha_0\rho_0}{2\alpha_1\rho_1\eta_{\alpha_0}} \\ \frac{1-2\beta_1{}^2p^2}{2\eta_{\beta_1}} & -p\beta_1 - \frac{\alpha_0 p\rho_0}{2\rho_1\eta_{\alpha_0}\eta_{\beta_1}} \end{bmatrix} \begin{bmatrix} U_R \\ U_Z \end{bmatrix}$$

where η_x is given by $\sqrt{1-x^2p^2}$ $(x = \alpha, \beta)$, ρ is the density, and subscripts 0 and 1 correspond to α, β and ρ for the water layer and seafloor layer, respectively.

The parameters used for rotation of the onshore stations were as follows: P-wave velocity = 5.5 km/s, S-wave velocity = 3.2 km/s, and density = 2900 kg/m^3. For OBS data, we used the sediment properties calculated from Ps sediment-crust conversion delay times for each individual station using empirical relationships (Rychert et al., 2018a). The OBS data were not corrected for tilt or compliance since these corrections are applied to the frequency band of 0.005 to 0.03 Hz (Bell et al., 2015), i.e., below that of this study (0.05-0.2 Hz), and therefore they do not influence the Ps receiver function imaging of MTZ discontinuities (Agius et al., 2021). We show examples of coherent RFs with adjacent piercing points at 410 km from on- and offshore data in Figure A.1.

We applied a band-pass filter between 0.05-0.2 Hz to the waveforms and then calculated the signal-to-noise ratio (SNR). The SNR of each signal was determined by comparing the largest amplitude in a 20-second-long window after the predicted P-wave arrival time to the standard deviation of the amplitudes in a window beginning 60 seconds prior to the predicted P-wave arrival. For land stations waveforms with SNRs smaller than 2 were discarded. We did not discard OBS data using the SNR approach. Instead, we performed an initial visual inspection of the OBS waveforms and performed an initial elimination. We can confirm by visual inspection that the largest amplitudes also correspond to the P-waves and the initial SNR cutoff is a valid approach. The remaining waveforms, corresponding to 21356 event-station pairs, were deconvolved using the extended-time multi-taper frequency domain deconvolution technique (Helffrich, 2006).

Each RF was migrated to depth with respect to sea level, correcting for station elevation. The mantle migration model assumes velocities from IASP91 (Kennett & Engdahl, 1991). For crustal velocities, a modified version of CRUST1.0 was used (Laske et al., 2013). For land stations, the sediment and crystalline crust layers from CRUST 1.0 were used. For the OBS stations, we used the sediment thickness and velocities derived from the Ps sediment-crust conversion delay times at each station (Rychert et al., 2018a) and crystalline crust values from CRUST1.0.

We inspected each waveform and corresponding RF visually to pick reliable waveforms, eliminating unstable deconvolutions characterized by pure ringing. The P410s and P660s conversions arrived with coda and in some cases, strong noise. In some cases, only one of the conversions was clear, while the other was suppressed by noise or ringing. Establishing two separate datasets for the

P410s and the P660s can maximize the potential use of as many RFs as possible (Agius et al., 2017). For RFs in each dataset, we required Ps phases that clearly stand out from the Moho and either the 410 or 660 discontinuities, within 40 km of the theoretical. We considered the converted phases from 410 and 660 in comparison to those at all adjacent piercing points within ~100 km of the conversion, after migration to the depth domain, and eliminated outlier RFs with conversions at apparent depths different (> ~20 km) than the neighbouring waveforms. Thereafter, we obtained 1919 RFs in total. The P410s data set consisted of 952 waveforms with 205 from OBS data, whereas the P660s data set comprised 1261 waveforms with 392 from OBS data.

We found that the amplitudes of RFs from OBS data were systematically larger than those from land data (Figure 2.2). This has been observed in previous amphibious experiments, and it is expected for typical sediment/ocean interfaces (Kim et al., 2021). We divided the RF amplitudes by the ratios of the median amplitudes of the offshore and onshore P410s and P660s data, respectively, as done in previous work, in order to meld the datasets (Kim et al., 2021). Our testing with synthetic seismograms indicates this is a reasonable way to deal with the two datasets (Supplementary Material). Synthetic testing shows that while ocean bottom receiver functions are predicted to show a different character than land receiver functions at shallow depths, this does not affect the resolution of discontinuities at MTZ depths. In addition, reverberations in ocean receiver functions from shallow discontinuities are not expected to strongly influence MTZ discontinuity resolution (Figure A.1, A.2).

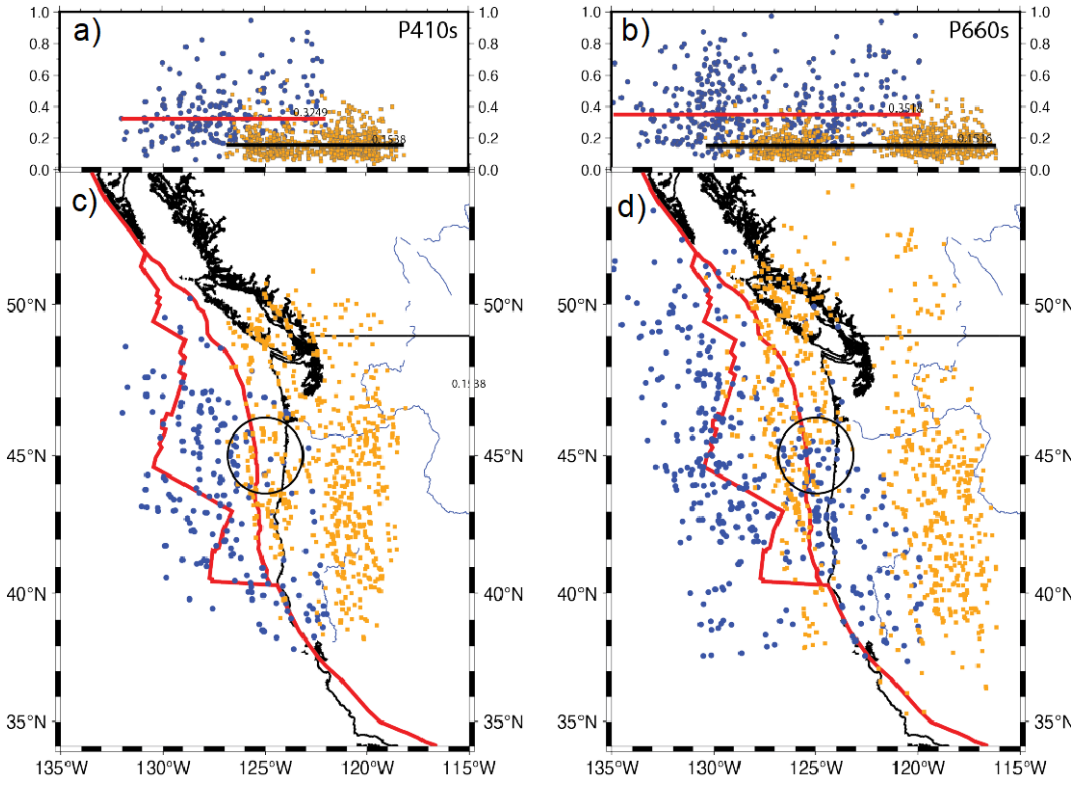

Figure 2.2 Piercing points of picked RFs at 410 and 660 km depth and corresponding P410s P660s amplitudes. a) Amplitudes of P410s vs. longitude. Blue circles show piercing point

longitudes at 410 km of picked RFs from offshore data. Orange squares show piercing point longitudes at 410 km of picked RFs from onshore data. The red thick line shows the median of P410s amplitudes from offshore data, and the black thick line shows the median from onshore data. Numbers on the right side of the lines indicate the corresponding median values. b) Similar to a) but for P610s. c) Spatial distribution of piercing points (blue circles for ocean data and orange squares for land data) at 410 km depth. Red lines show plate boundaries. The black circle indicates the bin used in Figure A.3. d) Same as c. but for the P660s dataset.

2.3.2 Error bars, depth migration, and tests

Selected RFs were migrated to depth and back-projected along the theoretical ray path and stacked onto a 3-D grid that has a lateral spacing of 1° by 1° and a 1km depth spacing. The grid smoothing was determined by waveforms within the Fresnel zone of which the radius is $\sqrt{(\frac{\lambda}{2}+d)^2-d^2}$, where λ is the wavelength and d is the depth, centred in the grid. Since we set separate collections for P410s and P660s, two 3-D grids were generated first and then merged into one by using a linear weighing between 410- to 660- km depth of the grids. A weighted average is applied to the 410 and 660 datasets. The weights for the P410s dataset grid decrease linearly from 1 to 0 from 410 to 660 km depth, while weights for the P660s dataset grid increase linearly from 0 to 1 over the same depth range. There are sufficient waveforms (> 5) to resolve discontinuities in all bins plotted (Figure A.4). There are no gaps within the model, therefore sampling does not affect our interpretation. The region of overlap of resolved 410 and 660 is > 10 degrees longitude and > 20 degrees of latitude.

The reported error bars in the abstract are the standard errors of the means of each bin across subregions. In the main text, the error bars of the 410 and 660 km discontinuity depths represent the standard error of the mean of the depths of the peaks of the individual waveforms in each bin. These vary across the study area from 1 - 4 km and 1 - 7 km for the 410 and the 660 respectively (Figure A.5). The error bars on transition zone thickness reported for a given region in our study area correspond to the errors propagated from the 410 and the 660 discontinuity depths.

We performed tests using different migration models to test the robustness of our observations (Figure 2.3). In all tests, we left the sediment and crustal corrections intact, given that these shallow layers are well-constrained by independent observations. We report maximum differences compared to results from sediment and crustal corrections IASP91 model in absolute depths, noting that the observed phases and depth anomaly patterns presented and discussed in the following sections remained intact.

We first tested the effect of using the 1-D mantle velocities from PREM (Dziewonski & Anderson, 1981) instead of IASP91. The average differences in the depths of the 410 and the 660 between these two models are 1.69 km and 3.88 km, respectively, and 3.39 km for the difference of the MTZ thickness.

We also tested a series of 3-D models. We tested the effect of using the regional P-wave velocity anomalies from model CAS2018_P (Bodmer et al., 2018) (extrapolating in the western and southern edges to cover our study area), relating the anomalies to P-velocity assuming an IASP91 background model and calculating S-wave velocities assuming the Vp/Vs values from IASP91. The results have a good agreement with migration using the 1-D mantle model. 95% of pixel-to-pixel differences of the depths of the 410 and the 660 and the thickness of the MTZ ranged within 5 km, 11 km, and 10 km respectively.

Then we tested the global model PRI (Montelli et al., 2006) which has both P- and S-wave velocities. The average differences in the depths of the 410 and the 660 between these two models are 2.50 km and 10.24 km, respectively, and 7.08 km for the difference of the MTZ thickness.

We also tested the global S-wave velocity model SEMuM2 (French et al., 2013) assuming P-wave velocities calculated using the Vp/Vs ratio from the IASP91. The average differences in the depths of the 410 and the 660 between these two models are 4.40 km and 9.61 km, respectively, and 5.58 km for the difference of the MTZ thickness.

Changes in depth resulting from migration model changes are sometimes larger than the reported formal error bars. However, this is a systematic error or bias. The trends are robust regardless of the migration model, and therefore would not change the interpretation or our understanding of the Earth.

Since the overall observed patterns remain intact, e.g., the depressions of the 410 in the north and south and the uplifted 660 beneath the ridges and slabs, these tests show that the main interpretations of this manuscript are robust. We prefer the IASP91 migration model given that it avoids inherent additional uncertainties related to resolution in tomographic models. In addition, it avoids uncertainty related to choosing a Vp/Vs ratio when using local models that are only for Vp.

2.3.3 Temperature estimates

We estimated temperature anomalies for the MTZ using the relationships of temperature with discontinuity depths applied in previous work (Agius et al., 2021): These include a +2.9 MPa/K slope for the 410 (Bina & Helffrich, 1994) and a −2.5 MPa/K slope for the 660 (Ye et al., 2014) based on experimental relationships of pressure and mineral phase transitions. The average 5 km depression

of the 410 and the 15 km elevation of the 660 correspond to 60 K and 190 K thermal anomalies respectively using the assumed Clapeyron slopes.

A wide range of Clapeyron slopes has been reported, from 1.5 - 2.9 MPa/K for the phase transition at the 410 (Akaogi et al., 1989; Bina & Helffrich, 1994) and from −4.0 to −2.0 MPa/K at the 660 (Bina & Helffrich, 1994; Ito et al., 1990). The thermal anomalies associated with the average depression and uplift reported above would be 60 - 115 K and 138 - 276 K, respectively, for these slopes. However, this does not affect our interpretation of upwellings and downwellings based on the topography of the discontinuities and body wave tomography (Bodmer et al., 2018).

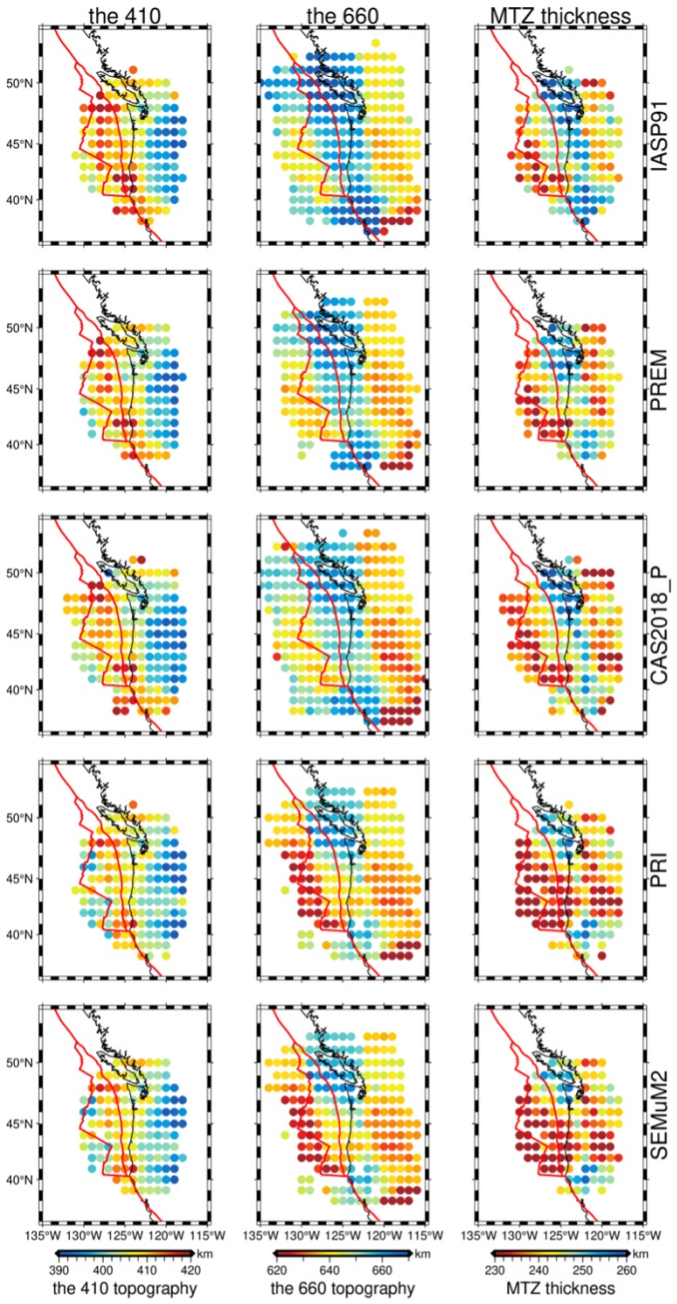

Figure 2.3 Migration tests. Topography maps of the 410, the 660, and MTZ thickness from migration using 1-D mantle models from IASP91 (Kennett et al., 1995) (top), PREM (Dziewonski & Anderson, 1981) (second row), the 3-D dVp CAS2018_P (Bodmer et al., 2018) anomaly

model related to absolute P-velocity assuming IASP91 for the reference model and calculating S-wave velocities assuming the Vp/Vs values from IASP91 (third row), 3-D Vs model SEMuM2 (French et al., 2013) with Vp/Vs ratio from IASP91 (bottom), and 3-D Vp and Vs models from PRI (Montelli et al., 2006) (fourth row).

2.4 Results

The main phases that we image are positive phases, or velocity increases caused by the 410 and 660 discontinuities, and these are imaged across the study region. We also image negative phases at ~ 370 km depth, strongest in discrete locations beneath the Mendocino Fracture Zone and the north-central Juan de Fuca Plate (Figure 2.4 a, c). Time-domain deconvolution tests suggest that the strongest supra-410 phases are not sidelobe artefacts but rather robust features (Figure A.2, A.3). We image strong positive phases beneath the 660 at ~ 750 km depth east of 122° W and north of 47° N (Figure 2.4c). Similar phases were detected in this region by a previous RF study and interpreted as a region of high basalt content (Frazer & Park, 2021). We do not interpret these phases further, nor do we interpret the negative phases between the 660 and the positive phases at ~750 km depth, given the proximity of those depths and the potential for the interference of sidelobes. Strong negative phases beneath the 410 are imaged but at the very southeastern corner of our study area (Figure 2.4 a). These could potentially be related to the edge of the slab, although, dipping structures can cause complex receiver function imaging, making definitive interpretation challenging (Lekić & Fischer, 2017). Therefore, we do not interpret further since the phases are not the topic of this work.

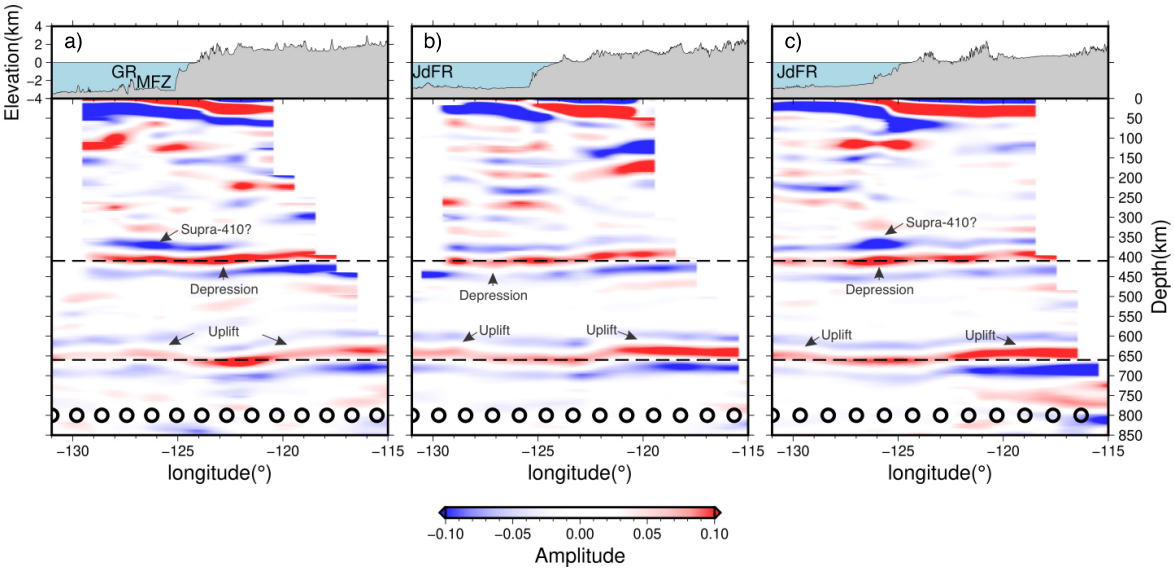

Figure 2.4 Vertical cross-sections. a) Top: bathymetry/topography along 40.5° N from 131° W to 115° W. Bottom: Vertical cross-section from 3-D migrated RFs along 40.5° N with location shown in Figure 2.1. Dashed black lines indicate 410 km and 660 km depths. Black circles along the cross sections correspond to a spacing of 100 km. Black arrows indicate supra-

410 phases. Small black arrows indicate significantly depressed 410 and uplifted 660. b) and c) are the same as a) but along 45° N (b) and 47.5° N (c), respectively. The plate boundaries are labelled as follows: Gorda Ridge (GR), Mendocino Fracture Zone (MFZ), and Juan de Fuca Ridge (JdFR).

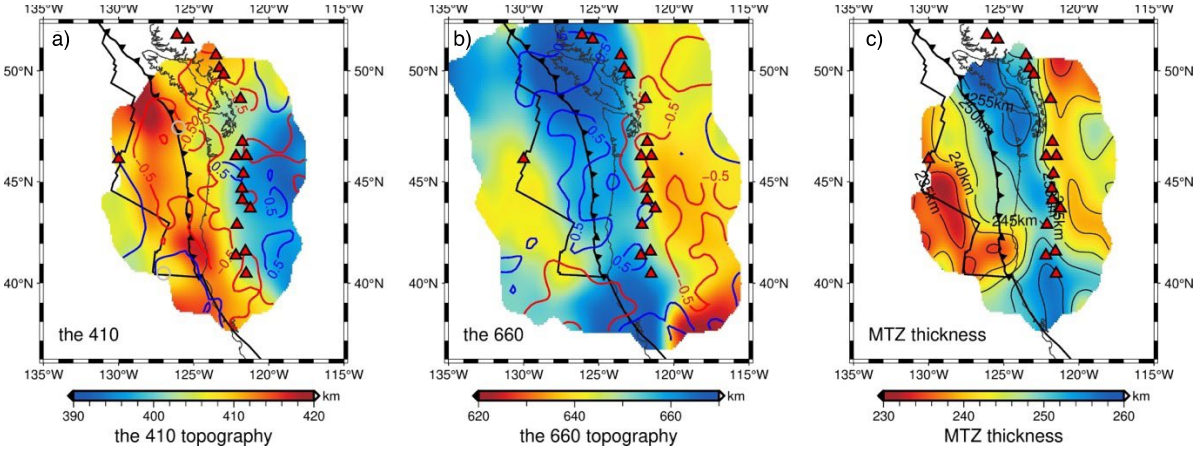

Figure 2.5 Maps of the 410 topography and the 660 topography and the thickness of MTZ. a) Colours show the depths of the 410. Thick black lines represent plate boundaries, and the serrated line shows the trench. Red triangles indicate the locations of major volcanos of the Cascadia Arc and the Axial Seamount. Red contours show -0.5% P-wave velocity anomalies, and blue contours show +0.5% P-wave velocity anomalies from body wave tomography (Bodmer et al., 2018). Grey circles indicate the locations of bins used for time-domain tests (Figure A.3). b) Same as a), but for the 660. c) Similar to a), but for the MTZ thickness. Thin black lines show contours of MTZ thickness.

The average thickness of the mantle transition of our study area is 245 ± 1 km in agreement with the global average observations of 242 ± 2 km from Ps RFs (Lawrence & Shearer, 2006), 242 ± 20 km from SS precursors (Gu & Dziewonski, 2002; Lawrence & Shearer, 2008), and also the theoretical 250 km thickness, with a total range between 231 and 258 ± 6 km. East of the Cascadia Volcanic Arc, the MTZ is thinned by 5 to 10 km in comparison to the theoretical. In the middle of our research area, roughly along the coast, the MTZ is of normal thickness with zones of slight thickening, up to 10 km, in the north beneath south Vancouver Island to the Olympic Peninsula and in the south beneath the Cascadia Arc in northern California. The thickening is mainly because of the depression of the corresponding 660. The greatest amount of thinning (15 - 20 km) is located beneath the ridges and transform fault system in the west from the junction of the Gorda Ridge and the Mendocino Fracture Zone to the inner corner of the intersection of the Juan de Fuca Ridge and the Blanco Transform Fault. We do not observe focused thinning, uplifted 660 or depressed 410 directly beneath the Cobb hotspot. The 660 topography is uplifted by up to 15 ± 4 km in the west and 10 - 20 ± 3 km in the east. The 410 is normal to slightly uplifted (4 km ± 2 km) in the west of our research area and uplifted by 10 km to 15 ± 2 km in the east. The 410 is depressed in the central parts of our study area, most

notably by up to 13 ± 3 km in the northernmost section in a region below the trench and the ridge and by up to 11 ± 3 km in the south beneath the trench east of the Gorda Ridge (Figure 2.5). The depression of the 410 is 5 ± 2 km on average. The thickened MTZ (by 2 - 12 km) in the centre of our study region, primarily related to a depressed 660, corresponds to subtle P-wave velocity anomalies (0.5%) (Figure 2.5 b). Since this is > 600 km east of the slab inferred from body wave tomography, it would need to be an ancient torn piece of Farallon slabs (Bodmer et al., 2018). This is not a major feature of our model and we have no strong interpretation of it.

2.5 Discussions

The most prominent anomaly in our result, the thinned MTZ beneath the western portion of our study area by 10 - 20 km agrees with thinning of 16 km reported in this region by a previous global SS precursors study (Huang et al., 2019). Finer scale variability in our MTZ discontinuity topography is not likely resolved by the global study. The MTZ discontinuities have been imaged beneath western North America by multiple RF studies with similar resolutions as ours. Overall, the magnitudes and patterns of the discontinuity topographies and MTZ thickness are variable among these studies, likely owing to differences in data and/or approach, such as data selection (manual vs. automatic) and/or migration assumptions (Eagar et al., 2010; Gao & Liu, 2014; Schmandt et al., 2012; Zhou, 2018). However, we do find some general agreement with previous studies. For instance, two studies found MTZ thinning of 5 - 10 km in the eastern part of our study region in agreement with the 5 - 20 thinning observed in our result (Eagar et al., 2010; Schmandt et al., 2012).

2.5.1 Abnormal discontinuity topography and estimated temperature anomalies

The 410 and 660 depths may be affected by temperature and/or composition (Ghosh et al., 2013; Hirose, 2002; Ito & Katsura, 1989; Katsura & Ito, 1989; Smyth & Frost, 2002). However, we do not find particularly strong evidence for compositional effects in general, e.g., uplifted 410 or depressed 660 accompanied by slow seismic velocities for water, or very depressed or broad 660 for basalt. Instead, the variations of the 410 and the 660 depths are in good agreement with the seismic tomography, i.e., the locations of depressed the 410 correspond to low-velocity anomalies, the uplifts and depression of the 660 correspond to low-velocity anomalies and high-velocity anomalies (Figure 2.5 a, b), which is more consistent with thermal anomalies caused by upwellings or downwellings.

There is a small region on the eastern side of our study area that is characterized by an uplifted 410 and slow velocities in the transition zone (Figure 2.6 b, c), i.e., indicative of hydration. This could be a possible explanation. However, the thickening could also be related to the nearby slab. If the uplifted 410 in the eastern section of the study area is caused by the slab it would correspond to an

anomaly of 121 - 181 K (Figure 2.5 a, 2.6). We do not find a corresponding depressed 660 in the east, likely because the slab is located outside our study region at those depths, as suggested by the body wave tomography anomalies (Figure 2.6) (Bodmer et al., 2018). Given the ambiguity of the slab location, we do not have a strong interpretation of the observed uplifted 410.

Very large depressions on the 660 are thought to be caused by very high temperatures or basalt contents, e.g., where garnet would dominate over olivine at the 660 at 200 - 300 K above the global average mantle temperature (Hirose, 2002). This has been observed for instance beneath Iceland (Jenkins et al., 2016). However, we do not observe this, nor do we necessarily expect very large temperatures or basalt contents.

Therefore, we proceed assuming the temperature-sensitive olivine phase changes with the Clapeyron slope (Bina & Helffrich, 1994), and that compositional effects on the remainder of the study area besides the eastern portion, if any, are minimal.

The thickened MTZ (by 2 - 12 km) in the centre of our study region, primarily related to a depressed 660, corresponds to subtle P-wave velocity anomalies (0.5%) (Figure 2.5 b). Since this is > 600 km east of the slab inferred from body wave tomography, it would need to be an ancient torn piece of Farallon slabs (Bodmer et al., 2018). This is not a major feature of our model and we have no strong interpretation of it.

The lack of strong MTZ thinning beneath the Axial seamount, the volcanically active surface realization of the Cobb Hotspot, could be explained by a variety of possibilities. A conduit that is less than ~100 km in diameter, the size of one of our bins, is below our resolution. The anomaly could also be muted in magnitude. Gravity arguments have been used to suggest it has an excess temperature of 30 °C - 40 °C (Hooft & Detrick, 1995), which would correspond to a 3 - 5 km transition zone thickness anomaly, i.e., near the size of our error bars and at the edge of resolution. Alternatively, the hotspot may take a non-vertical path through the upper mantle, crossing the 410 at the location of our anomaly 100 km to the northeast.

2.5.2 Dynamics

Several global tomography models also support deep upwellings in this region, finding slow velocities at 660 - 1000 km depth (Figure A.6). The variations of the 660 topography contribute more to the MTZ thickness differences as they are correlated at 0.73 with the MTZ thickness (Figure 2.7). The thinned MTZ and uplifted 660 in our study area suggest that material upwells from the lower mantle beneath the intermediate spreading ridges in Cascadia and beneath the base of the Cascadia slabs. This expands the interpretation that upwelling occurs beneath slow-spreading environments (Agius et al., 2021) to intermediate-spreading environments. It suggests that sub-slab upwelling inferred

from slow velocity anomalies needs not necessarily be an artifact of tomography resolution e.g., (Bezada et al., 2016; Bodmer et al., 2020). While many geodynamic models predict downwelling sub-slab material, some also suggest that buoyant upwelling material may be possible beneath a subducting slab, which could potentially uplift the 660 (Yang & Faccenda, 2020).

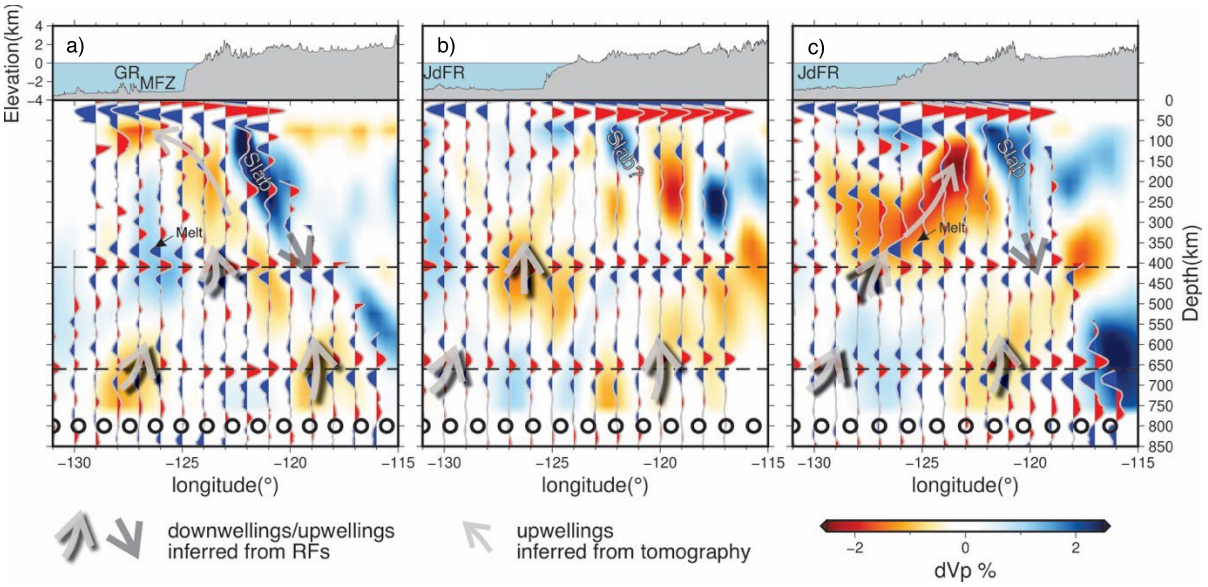

Figure 2.6 Vertical cross-sections compared to anomalies from tomography and inferred dynamics. a) Top: bathymetry/topography along 40.5° N from 131° W to 115° W. Bottom: Vertical cross-section from 3-D migrated RFs (grey wiggles) along 40.5° N. Background colours are P-wave velocity anomalies from CAS2018_P (Bodmer et al., 2018). Semi-transparent grey and black arrows with shades indicate inferred pathways of upwellings and downwellings (slabs). Semi-transparent grey arrow shows suggested upper mantle upwellings (Bodmer et al., 2018). b) and c) are the same as a) but along 45° N (b) and 47.5° N (c), respectively. Plate boundaries are labelled as follows: Gorda Ridge (GR), Mendocino Fracture Zone (MFZ), and Juan de Fuca Ridge (JdFR). Black circles at 800 km depth are plotted every 100 km along the cross-sections and correspond to those plotted in Figure 2.1.

Surprisingly, the 410 depressions do not correspond to the locations of the uplifted 660, and instead, occur roughly between the uplifted 660 regions. This observation is consistent with a non-vertical ascent through the MTZ, which is much different from the typical paradigm of the simple vertical ascent of material through the MTZ (Morgan, 1971). However, the observation agrees with observations from the Mid-Atlantic Ridge where the peak 410 topography was offset from that of the 660 (Agius et al., 2021). In our study region, the strongest 410 depressions occur in the north and the south, suggesting a more 3-D flow. In the south, the 410 depression and the eastern 660 uplift occur just beneath the slab region as defined by the 0.5 % fast contour from body wave tomography (Bodmer et al., 2018) (Figure 2.5). In the northern sections, the 660 is uplifted beneath the slab but

the 410 depression occurs roughly midway between the ridge and the slab, i.e., ~500 km west of the base of the slab. One possibility is that the upwellings from the lower mantle in our study region stagnate within the MTZ before reaching 410. The stagnation could occur because the upwellings dehydrate during ascent through the MTZ, as predicted by geodynamics (Long et al., 2019).

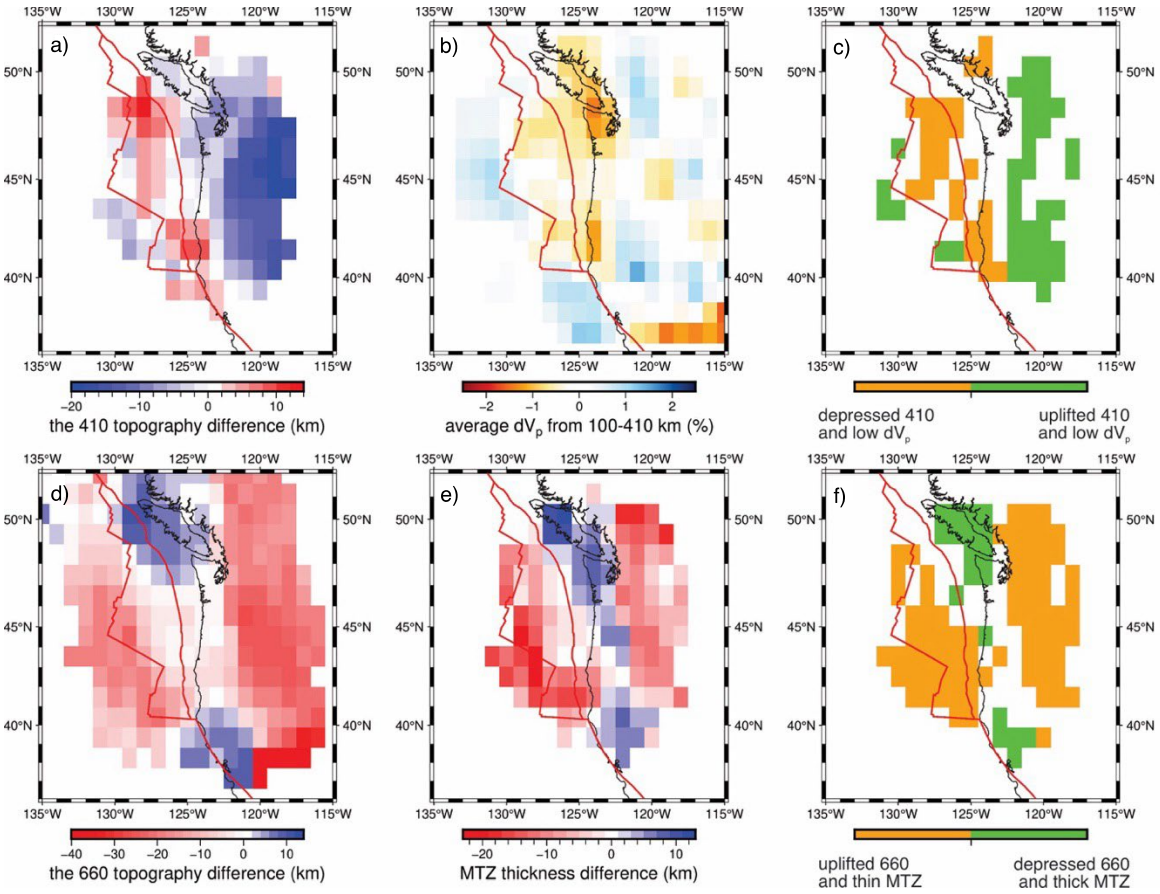

Figure 2.7 Maps of the 410 and the 660 differential topography, the differential thickness of MTZ, and average P-wave velocity anomalies and their correlations. a) The 410 topography difference compared to 410 km. b) Average P-wave anomalies (dVp) from 100 to 410 km (Bodmer et al., 2018). c) Regions of 410 depressions and slow average Vp from 100 to 410 km depth (orange) and regions of uplifted 410 and fast average Vp from 100 to 410 km depth (green). d) The 660 topography difference compared to 660 km. e) MTZ thickness difference compared to 250 km. f) Regions of MTZ thinning and uplifted 660 (orange) and regions of MTZ thickening and depressed 660 (green).

Instead, the locations of thermal upwellings suggested by our 410 depressions are coincident with the locations of slow seismic velocity anomalies from the body wave tomography (Figure 2.7). The slow velocities were interpreted as buoyant upper mantle flow at < 100 - 350 km depth. In the north, the inferred flow originates from the west, bending eastward toward the slab as it nears the surface (Figure 2.6, light grey arrows) (Bodmer et al., 2018), which is also generally consistent with west-east shear wave splitting directions reported east of the Cobb Hotspot (Martin-Short et al., 2015). In the south, the flow occurs from east to west up the base of the slab (Figure 2.6, light grey

arrows) (Bodmer et al., 2018), which could also be consistent with complex shear wave splitting directions reported from the eastern side of the Blanco Fracture Zone. Our 410 depressions are coincident with deeper realizations of the slow anomalies associated with the interpreted flow, suggesting that the flow originates from within the mantle transition zone (Figure 2.6, arrows pointing upwards at 410 km depth).

There are a few possible causes for the inferred reversed flow direction in the north in comparison to the south. The difference may be related to additional buoyancy from the Cobb Hotspot (Bodmer et al., 2018). Neither our MTZ discontinuity depths nor the body wave tomography detects a strong hotspot anomaly. However, we cannot preclude the possibility that the hotspot causes the variation in dynamics with latitude. An alternative is that the difference in flow direction occurs because the southern edge of our study area is located near the hypothesized southern edge of the Gorda slab, as inferred from tomography (Bodmer et al., 2018). Toroidal flow around the slab edge could result in more complex mantle flow in the region (Eakin et al., 2010).

The intermittently imaged negative discontinuities at 365 - 385 km depth may be caused by conversions from the top of a supra-410 melt layer. In the north, the negative phase is strongest directly above the inferred location of upwelling based on 410 topography. In the south, the negative phase exists just to the west of the location of inferred upwelling. Supra-410 melt is predicted to occur when hydrous material upwells from the MTZ into the less-soluble overlying mantle (Bercovici & Karato, 2003), and discontinuities related to such a layer have been imaged by a variety of studies (Frazer & Park, 2021; Wei & Shearer, 2017). The observations are consistent with this model and suggest that upper mantle flow may enter the MTZ and entrain hydrous material to shallower depths. A supra-410 discontinuity is not imaged above the inferred upwelling based on the 410 topography at middle latitudes (Figure 2.4 b). Therefore, MTZ hydration may be variable and/or supra-410 melt may be transient in time and/or space possibly owing to melt migration (Hier-Majumder et al., 2021). Either could explain the wide variety of hypothesized preferential tectonic locations and/or sporadic imaging of supra-410 melt layers (Bercovici & Karato, 2003; Wei & Shearer, 2017). We note that although our testing indicates the supra-410 phases persist regardless of the deconvolution method and migration models (Figure A.3, A.7), the melt-layer discontinuities are not necessarily required to support the conclusions of this paper, although they are intriguing and aligned with our interpretation.

2.6 Conclusions

We use extended-time multi-taper Ps RFs to image the MTZ discontinuities beneath the Cascadia region using an amphibious dataset. We interpret phases that are above the formal error bars of the stack, away from the far edges of the model, and at depths deeper than those contaminated by

crustal reverberation artefacts. Although migration model assumptions can impact the absolute depths of the imaged discontinuities, the existence of the MTZ phases and the trends of the MTZ discontinuity depths and MTZ thicknesses that we interpret are robust regardless of migration model assumptions.

The MTZ is thinned beneath the Juan de Fuca and Gorda Ridges and beneath the Cascadia Slabs and corresponds to the locations of the uplifted 660. The most depressed 410 lies beneath the northern Juan de Fuca plate and beneath the Gorda plate, offset from where the 660 is largely uplifted. The depths of the 410 and the 660 beneath the Cascadia are not anticorrelated as in classical diagrams for regions where ascending/descending happens. However, the variations of the 410 and the 660 topography are in good agreement with thermal predictions based on previous seismic tomography observations. We do not find strong evidence for compositional effects in the central portions of our study region and the locations where our interpretations are focused.

Overall, this suggests that deep upwellings from the lower mantle may occur beneath tectonic locations other than hotspots, including beneath ridges and beneath slabs. However, the upwellings are sluggish and may stagnate in the MTZ, possibly owing to dehydration, instead of continuing to ascend vertically. Instead, upper mantle convection can interact with the shallow MTZ, entraining hydrated MTZ material and transporting it into the mantle above. This provides a new transport mechanism for the redistribution of hydration into the mantle above the MTZ. It suggests that in regions distant from a major hotspot like Hawaii and Iceland, i.e., the majority of the Earth, upper mantle dynamics may play a larger role in dictating material transfer from the MTZ into the upper mantle.

Chapter 3 A global SS precursor method for imaging discontinuities: the Moho and beyond

3.1 Abstract

Imaging seismic velocity discontinuities within the Earth's crust and mantle offers important insight into our understanding of the tectonic plate, associated mantle dynamics, and the evolution of the planet. However, imaging velocity discontinuities in locations where station coverage is sparse, is sometimes challenging. Here, we demonstrate the effectiveness of a new imaging approach using deconvolved SS precursor phases. We demonstrate its effectiveness by applying it to synthetic seismograms. We also apply it to ~1.6M SS precursor waveforms from the global seismic database (1990 – 2018) for comparison with CRUST1.0. We migrate to depth and stack the data in circular 6° bins. The tests demonstrate that we can recover Moho depths as shallow as 20 km. The Moho is imaged at 21 – 67 km depth beneath continental regions. The Moho increases in depth from 21 km ± 4 km beneath the continental shelf to 45 – 50 km beneath the continental interiors and is as deep as 67 ± 4 km beneath Tibet. We resolve the Moho in 77 % of all continental bins within 10 km of Crust 1.0, with all outliers located in coastal regions. We also demonstrate the feasibility of using this method to image discontinuities associated with the mantle transition zone with both synthetic and real data. Overall, the approach shows broad promise for imaging mantle discontinuities.

3.2 Introduction

Earth's radial structure is characterized by distinct boundaries associated with variations in seismic velocity and density (Dziewonski & Anderson, 1981). Various physical and chemical processes are attributed to these variations. The shallowest of these boundaries include, for instance, the Moho, the lithosphere-asthenosphere boundary, and the transition zone discontinuities. The Moho (Mohorovičić, 1910) defines a boundary between the chemically distinct and seismically slow crust from the faster mantle beneath. The lithosphere-asthenosphere boundary represents the transition from a rheologically strong and seismically fast lithosphere, comprised of the crust and a section of the upper mantle, to the deeper, weaker, and seismically slower asthenosphere (Artemieva, 2011; Eaton et al., 2009; Fischer et al., 2010; Rychert et al., 2020; Rychert et al., 2018b; Rychert & Shearer, 2009). The lithosphere is colder than the asthenosphere, and it may also be chemically distinct and/or partial melt may exist in the asthenosphere, further distinguishing the layers. The transition zone discontinuities are characterized by velocity increases with depth. They are typically interpreted as the pressure-induced solid-state transformation of olivine grains into denser crystal structures, or

phase changes, predicted by laboratory experiments (Ringwood, 1975): α olivine to β-spinel (wadslyite) at ~410 km, β-spinel to ringwoodite at ~520 km and ringwoodite to silicate perovskite and magnesiowüstite at ~660 km (Ringwood, 1975).

Imaging seismic velocity discontinuities globally can help us better understand the tectonic plate, mantle convection, and the evolution of the planet (Bostock, 1999; Rychert et al., 2007; Rychert & Shearer, 2011; Shearer, 1991; Tharimena et al., 2017b); although, tight constraints on these discontinuities globally and self-consistently can be challenging. For example, both surface wave and body wave seismic tomography provide important constraints on the seismic velocity of the crust and the mantle (Harmon et al., 2009; Masters et al., 1996; Montagner & Tanimoto, 1991; Ritsema et al., 2011), but the models have more difficulty resolving the exact location and character of sharp seismic discontinuities (Rychert et al., 2005a; Rychert et al., 2007). Receiver functions offer tighter constraints on the sharpness of velocity discontinuities but lack resolution in regions with sparse or no station coverage (Rychert et al., 2010). The highest resolution constraints come from active source studies, although these are limited in terms of spatial extent and also the depth to which they can image, with only very few studies imaging lithosphere-asthenosphere depths (Mehouachi & Singh, 2018; Roy Chowdhury, 2020; Stern et al., 2015).

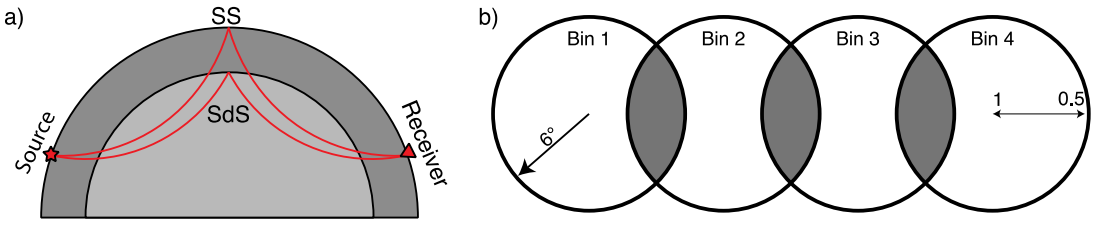

Figure 3.1 a) Schematic showing ray paths of the SS and the SdS phases, which are sensitive to the structure beneath the bounce point, roughly halfway between the source and the receiver. SdS refers to the underside reflection of the S wave at a discontinuity, located at 'd' km depth, e.g. Moho, 410, 660. b) Schematic representation of bins in the grid binning schemes. The shaded area shows the region of overlap between bins. The '1' and '0.5' labels indicate the weighting that is applied to the data, which varies linearly from 1 at the centre of the bin to 0.5 at the edge of the bin.

SS phases are shear waves that have bounced once off the surface of the Earth roughly mid-way between the source and the receiver. SS precursors are underside reflections from discontinuities that arrive just before the main SS phases, which are sensitive to the region of their bounce point (Figure 3.1). These are referred to as SdS, where 'd' indicates the discontinuity of interest, for instance, SmS would refer to the SS reflection from the Moho. The advantage of these phases is that they offer resolution in locations where station coverage is sparse. However, SS waveforms and their precursors are relatively long-period waveforms. Precursors reflected from shallow discontinuities like the Moho and the lithosphere-asthenosphere boundary typically interfere

with the surface-reflected SS waveforms, making them difficult to distinguish. Therefore, SS precursors have mostly been used to image deeper discontinuities such as the transition zone discontinuities (Flanagan & Shearer, 1998; Frazer & Park, 2023; Houser et al., 2008; Huang et al., 2019). To minimize waveform interference Schmerr (2012) considered acceleration seismograms, which are effectively filtered to higher frequencies and carefully selected data. The waveforms were stacked in bins and a discontinuity was detected approximately at lithosphere-asthenosphere depths (40 – 75 km) intermittently across the Pacific. In another approach Heit et al. (2010) deconvolved the SS waveform from itself before migrating and stacking in bins, imaging a discontinuity related to the Moho and the lithosphere-asthenosphere boundary beneath Asia. Rychert and Shearer (2010b) developed a strategy to image discontinuities using SS-precursors by performing waveform modelling on the sidelobes of the stacked SS-waveforms. Synthetic waveforms were calculated by convolving a reference SS stack with impulse operators corresponding to a variety of discontinuity depths and characters, and the best-fitting discontinuity was determined via a grid search approach. They validated the method at shallow Moho depths by demonstrating agreement with the CRUST2.0 (Bassin et al., 2000) and Mixture Density Network (MDN) (Meier et al., 2007) models in bins across Asia and extended the method to image the lithosphere-asthenosphere boundary across the Pacific using an attenuated S-wave as the reference waveform (Rychert & Shearer, 2010b). Tharimena et al. (2017b) followed a similar procedure as Rychert and Shearer (2011) to image lithosphere-asthenosphere structure beneath the Pacific but implemented a differential evolution algorithm (Price et al., 2005; Storn & Price, 1997) to minimize both the model storage size and computation time in comparison to a typical grid search. The inclusion of 7 additional years of data (1990 – 2014 instead of 1990 - 2007) yielded a three-fold increase in the number of waveforms and a higher resolution result in which greater numbers of parameters could be explored. The study found discontinuities consistent with Schmerr (2012) and Rychert and Shearer (2011) but also found evidence for locations where either two discontinuities exist in depth and/or lithosphere-asthenosphere boundary depths vary laterally within a Fresnel zone of the waveforms.

Here we develop an approach to clearly image seismic discontinuities via deconvolution. We also incorporate an additional 4 years of data in comparison to Tharimena et al. (2017b). We focus on the SS precursor phases that reflect at the Moho (SmS) for validation purposes. We demonstrate the validity of our approach by applying it to synthetic seismograms. We also validate our approach by comparing the recovered global Moho depths with those from the CRUST1.0 model (Laske et al., 2012). Finally, we discuss the potential of this method for imaging other discontinuities.

3.3 Methods

3.3.1 SS Data

We use the Incorporated Research Institutions for Seismology (IRIS) broadband dataset from 1990 to 2018, with event-to-station (epicentral) distances of 85° – 150°, for events with Mw > 5.5. Previous work has used a slightly more restricted range, e.g., 90° - 140° (Rychert & Shearer, 2010b). However, this choice does not appear to strongly contaminate our resolution, as we will describe in the results and discussion section. We restricted our analysis to raw data from broadband channels (20 – 40 samples per second), and events with source depth < 75 km to minimize complications from depth phases. The seismic records are corrected to remove instrument responses and then rotated to radial and transverse components. We consider only the transverse components.

We convert all seismograms from displacement to acceleration and then Hilbert transform them to produce symmetric SS pulses (Oppenheim & Schafer, 1975b; Rychert & Shearer, 2010b). The waveforms are resampled to 10 samples per second and band-pass filtered with corners at 0.02 Hz and 0.5 Hz. However, given the frequency content and dominant period of SS waves (~15 seconds), there is not much frequency content above this in the waveforms (Rychert & Shearer, 2011). An automated procedure is used to eliminate incomplete seismic records. We also use an automated procedure to centre the waveforms on the SS phase, which is picked as the maximum positive or negative amplitude in a 10-second time window before and after the theoretical SS arrival time. The amplitude of the centred waveform is normalised to unit amplitude. We compute the signal-to-noise ratio (SNR) for each record as the ratio of the maximum amplitude of the seismic phase to the standard deviation in a time window 270 s to 30 s preceding the SS pulse. Visual inspection of a random sample of 2000 waveforms shows that the waveforms are generally poor quality for SNR < 3. Therefore, waveforms with SNR < 3 are rejected. In addition, seismic records with amplitude > 1 within a 90 s window preceding the normalised SS pulse are rejected. Finally, records with long-period noise evaluated as those with zero-crossings that occur at > 20 s intervals are also rejected. We obtain 4,962,579 seismic records that fit the source parameters described above, 1,648,704 of which also fit the signal-to-noise criteria. Our data provides improved spatial coverage over previous studies (Figure 3.2).

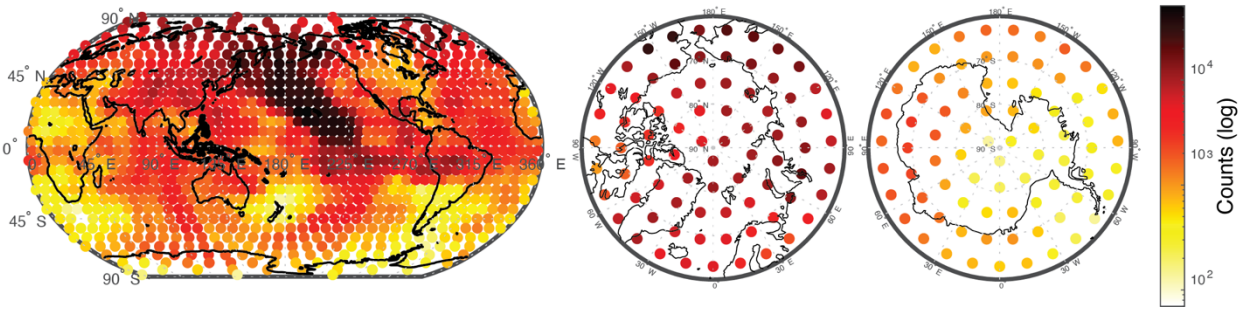

Figure 3.2 Maps showing the number of waveforms with SS phases and precursors in each bin that satisfy our requirements. Most of the Earth is shown (left) with the northern (central) and southern (right) hemisphere projections shown. 1,648,704 SS waveforms that satisfy our selection criteria are shown here.

3.3.2 Binning Schemes

Here, we define a global binning scheme (Figure 3.2) for stacking waveforms. We divide the surface of the Earth into evenly distributed 6° circular bins with 30% overlap, resulting in 1146 bins.

SS precursors have saddle-shaped Fresnel zones (Tharimena et al., 2016). However, this effect can be mitigated by stacking waveforms along different azimuths, which results in a more circular region of sensitivity centred on our bins and the sensitivity region of the precursors (Figure 3.1). The large number of waveforms (>1000) and better azimuthal coverage in each bin compared to our previous work minimizes the effect of off-axis structures in our study. In addition, we also linearly weigh the waveforms depending on their distance from the bin centre. We assign the highest weight of 1 to waveforms with bounce points closest to the bin centre and a weight of 0.5 to waveforms with bounce points on the edges of the circular bin. This further ensures that the SS precursor stacks are more sensitive to the structure beneath the bounce points.

3.3.3 S Data and processing source wavelets

The SS phases are Hilbert transformed relative to the S phases (Choy & Richards, 1975). Therefore, the deconvolution of stacked source S phases from Hilbert-transformed SS phases has the potential to separate the SS and SdS responses (Figure 3.3). We create event S-wave source stacks that will be deconvolved from the SS waveforms (Rychert & Shearer, 2011; Tharimena et al., 2017a; Tharimena et al., 2017b; Tharimena et al., 2016). We follow similar processing steps described above for the SS. We use seismic records from 1990 – 2018, with epicentral distances of 25° – 80°, for events with magnitudes Mw > 5.5, and source depths < 75 km. We resample the data to 10 Hz and then apply a band-pass filter with corners at 0.02 Hz and 0.5 Hz. We use an automated approach to pick the seismic *S* phase as the maximum positive or negative amplitude pulse in a 10-second window before and after the theoretical S arrival time. The signal-to-noise ratio for each seismic record is calculated

by comparing the maximum absolute value to the standard deviation in a time window 100 s – 20 s before the S phase. Waveforms with SNR < 2.8 are generally found to be of poor quality, with seismic coda before the S phase containing amplitudes as large as or greater than the S phase, and therefore they are rejected. The seismic records are then cut to a 40 s window centred on the picked S phase. The records are normalised to unit amplitude, and a 5 s cosine taper is applied to the ends of the wavelet. Finally, the source wavelets from all global receivers for a particular seismic event are stacked, scaling by individual SNRs to produce source stacks. We obtain 11,484 unique source stacks for the events from 1990 – 2018 in our study.

3.3.4 Deconvolution, Migration, and Stacking *SS* Waveforms

We deconvolve the S wavelet stack of the corresponding event from each SS waveform using an extended time multi-taper frequency domain deconvolution method (Helffrich, 2006; Rychert et al., 2012b) (Figure 3.3). The deconvolution method is a hybrid between multi-taper deconvolution and Welch's method for spectra estimation. Specifically, the method sums multi-taper cross and auto spectral estimates on several overlapping windows across the records and then performs the deconvolution. We use a 30-second window, with a 50% overlap on each window, a time-bandwidth product of 3 that translates to a frequency bandwidth of permissible spectral leakage of 0.2 Hz and 4 tapers (Shibutani et al., 2008). This results in an impulse response function that corresponds to the discontinuity structure beneath the bounce point. Deconvolutions of individual waveforms are normalised to the SS phase amplitude. The normalised impulse response functions with amplitudes larger than 1 in precursor sections are rejected.

The impulse response functions are then migrated to depth, stacked, and Moho depths are estimated. For the crust, we use a smoothed version of CRUST1.0, corresponding to the average thickness and velocity within the 6° bin. For the mantle we use the IASP91 model, beginning at sub-crustal depths. Finally, we stack the migrated impulse response functions scaled according to their signal-to-noise ratio and distance from the bin centre. We then search automatically for the peak in the stack arriving before the main SS pulse, which is likely related to the Moho discontinuity.

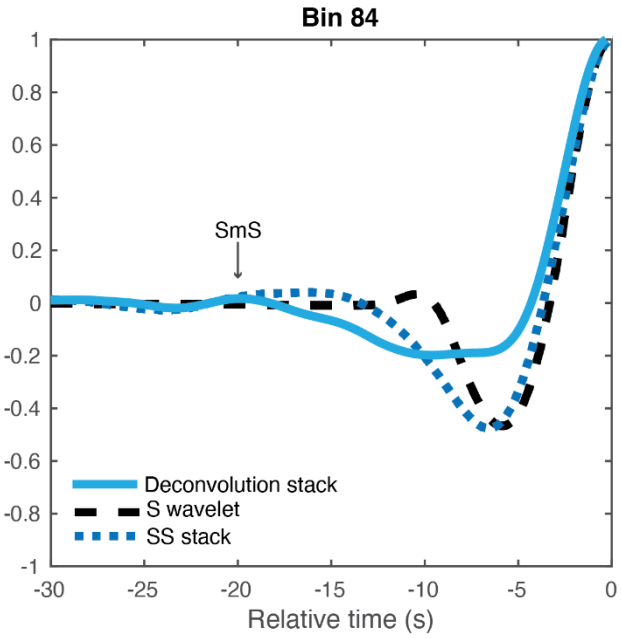

Figure 3.3 Deconvolutions of real data, Stacked S wavelet of an earthquake of Mw 6.9 that occurred at 06:48:10, Feb. 19, 1990, west of Luganville, Vanuatu, which contributes 30 waveforms to Bin 84, and all SS waveforms and deconvolutions stacked from Bin 84, located in North America. SmS phases are indicated by arrows.

3.3.5 Validation

We validate our approach by applying it to synthetic seismogram data calculated using the spectral element solver AxiSEM (Nissen-Meyer et al., 2014), which creates full waveform synthetics assuming a spherically symmetric Earth model. AxiSEM separates the problem of wave propagation in a symmetric medium into an analytical solution of the problem in the azimuthal (φ) direction perpendicular to the source-receiver plane and a numerical spectral-element discretization within the in-plane r, θ, which reduces the numerical cost to that of about a 2-D method (Nissen‐Meyer et al., 2007) and includes attenuation and anisotropy. We used a source with the following focal mechanism parameters: M0=1e21, strike=32, dip=62. We then generate wavefields for the 1-D velocity models modified from the reference earth model PREM (Dziewonski & Anderson, 1981) including a velocity increase at a range of potential Moho depths: 10, 20, 30, 40, and 60 km and one without crust. For models with Moho depths at 10 and 20 km, we replace the upper crust layer (≤ 15 km) in the PREM model with lower crust parameters and set the Moho at corresponding depths. For other models with deeper Mohos we extend the deeper crustal layer to the corresponding Moho depths. We process the synthetics in the same way we process the data and use the input model to translate the resulting receiver functions to depth.

Instaseis (van Driel et al., 2015), a Python package, is used to reconstruct seismograms for a source defined by moment-tensor and receiver locations using the precalculated wavefield databases. This

is possible due to the reciprocity of the Green's function which permits switching the location of source and receiver of a seismic wavefield. Instaseis uses the stored displacement wavefield to calculate strain, which enables the simulation of arbitrary moment tensors and source time functions.

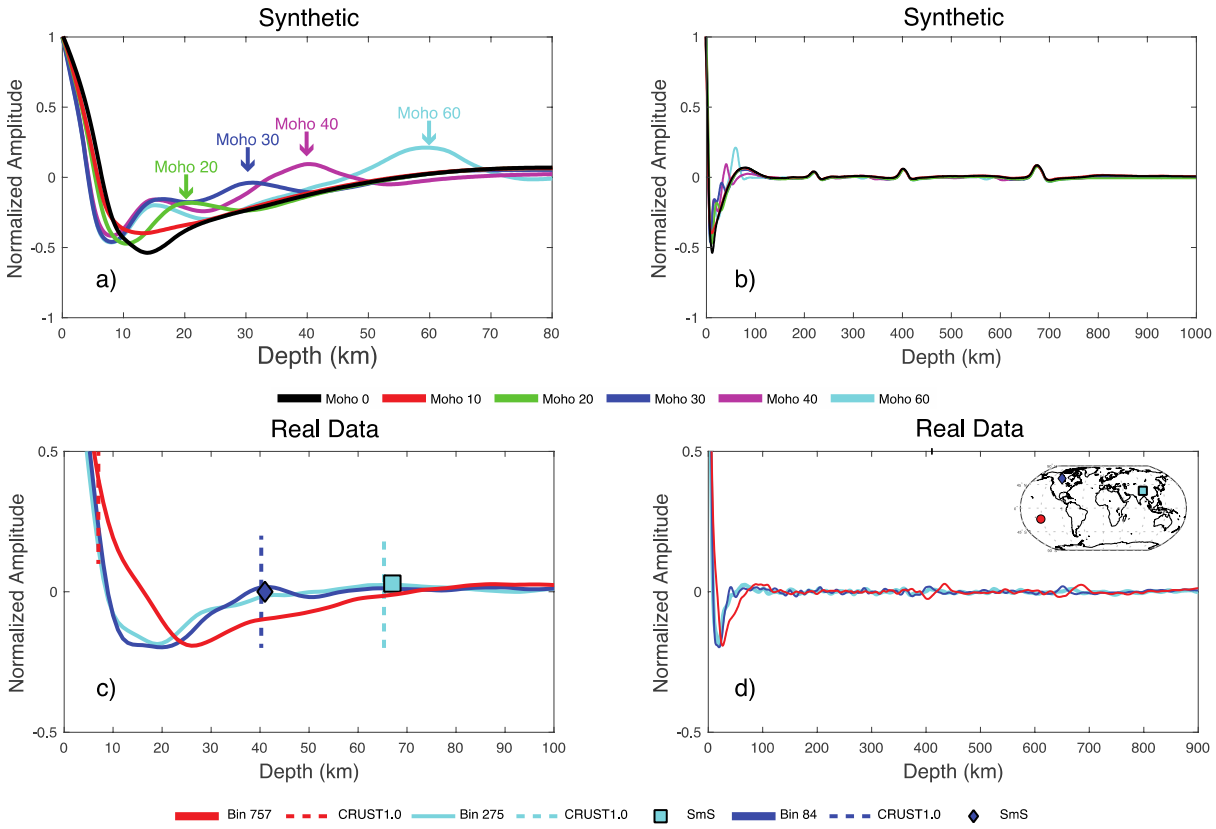

Figure 3.4 Synthetic and real examples. a) SS synthetics were calculated for models modified from PREM to incorporate a Moho at 10, 20, 30, 40, and 60 km depth and a model without a Moho. The synthetics were processed in the same way we process the data. We calculated waveforms from a range of epicentral distances (each degree from 85° - 150°) and stacked the resulting waveforms on the SS phase and migrated to depth. The resolved corresponding Moho depths are marked by arrows. b) Same as a) but in a longer depth window. c) Examples of real data in Bin 84, 757, and 275. Bin 757 represents an oceanic region where we failed to resolve the Moho. Bin 84 represents normal crust in North America and bin 275 represents a bin with thick crust in Tibet, which we resolve (diamond and square) in comparison to CRUST1.0 (dashed line). d) Same as c) but in a longer depth window. Markers in the inset map show the locations of these three bins, blue diamond for Bin 84, cyan square for Bin 275, and red circle for Bin 757.

We also compare the depth of SmS phase in each data bin to CRUST1.0. The standard deviation of error between resolved crustal thickness and CRUST1.0 is 4 km, which is the value we report as the error here.

3.4 Results and Discussion

The resolution testing with synthetics shows that we can resolve discontinuities as shallow as 20 km depth (Figure 3.4). We also resolve phases at 15 km depth for the synthetic models with Mohos at ≥ 30 km, since this discontinuity exists in the PREM model (Figure 3.4 a). However, it does not impact the resolution of the deeper Moho depths.

For real data, regions with Moho depths < 20 km are not well resolved. Therefore, we focus only on discontinuities at ≥ 20 km depth. This includes 397 bins out of 415 bins with continental crust according to the 3SMAC (Nataf & Ricard, 1996) classification.

Our SS precursor method applied to the data resolves the Moho globally beneath the continents well. We image a Moho at 21 – 67 km depth beneath the continents. The thickest crust, 67 ± 4 km depth, is imaged beneath the Himalayan region of Asia.

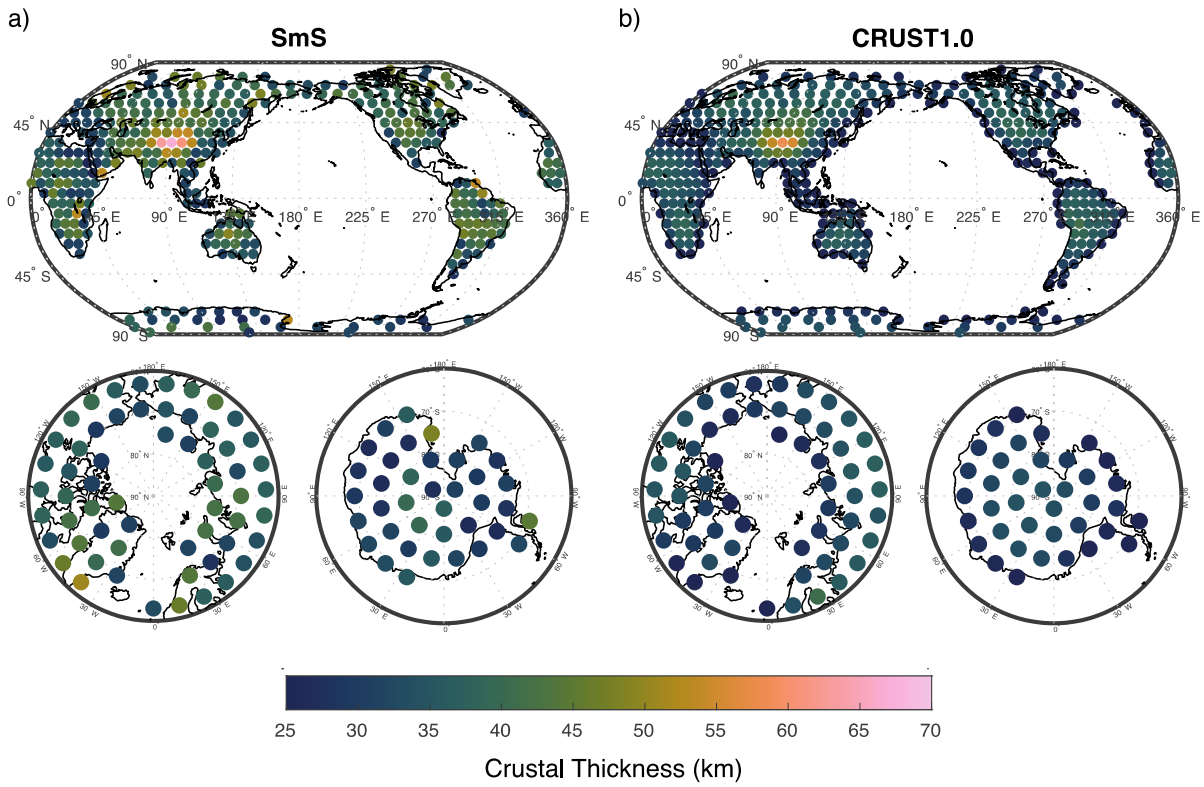

Figure 3.5 Crustal thickness. a) Crustal thickness measured from SmS phases. Top: global view; Bottom left: Antarctic view; Bottom right: Arctic view. b) Same as a), Crustal thickness from CRUST1.0 model.

Our results are in excellent agreement with crustal thickness from CRUST1.0 averaged over our bins in continental regions (Laske et al., 2012) (Figure 3.5). Our result is a minimum of 9 km shallower than CRUST1.0 in all locations (Figure 3.6). Our result is over 10 km deeper than CRUST1.0 in 19 % of bins with Crust > 20 km. The outliers are all located in coastal areas except for 1 bin in Africa. The reason for this asymmetry and the fact that SS cannot resolve the coastal bins is that the depths of

the CRUST1.0 model averaged over the bin areas are relatively shallow, given the nearby oceanic crust. However, shallow, oceanic Moho phases fall within the main SS pulse and do not affect its sidelobe or resulting Moho depth (Rychert & Shearer, 2010b). Therefore, the only resolved SS Moho in these coastal regions is from the thicker continental regions. In addition, thick sediments near coastal regions could add greater complexity (Wang et al., 2022). Excluding the 76 outlier coastal bins, observed crustal thicknesses of the remaining 321 bins are correlated with the CRUST1.0 model at 0.81, and 70 % of those bins are resolved within 5 km of CRUST1.0, with a correlation coefficient of 0.93. This verifies that this method can be used to resolve discontinuities, although we do not believe that it supersedes CRUST1.0.

Overall, the increase in data quantity and improved method demonstrate enhanced resolution capabilities in comparison to previous work (Rychert & Shearer, 2010b). Rychert and Shearer (2010b) resolved the Moho in 30 10° bins beneath Asia and at depths > 25 km, a region of particularly large bounce point coverage and deep Moho depths and found Moho depths correlated with CRUST2.0 at 0.82. However, we resolve the Moho beneath 321 bins in continental regions at depths as shallow as 20 km. Negative phases at sub-Moho depths may cause artificial LAB phases and/or interfere with LAB phases. Therefore, future work is required to assess the viability of this approach for the LAB; however, this method will be useful for other deeper discontinuities such as those of the mantle transition zone. From synthetic testing, despite variations of crustal thickness, the discontinuities at 200 km, 400 km, and 670 km in the PREM models were well resolved. Moreover, we also find clear phases associated with the mantle transition zone in real data even though the parameters, e.g. epicentre distances, and bandpass, used in this work may not be ideal to image them (Figure 3.4).

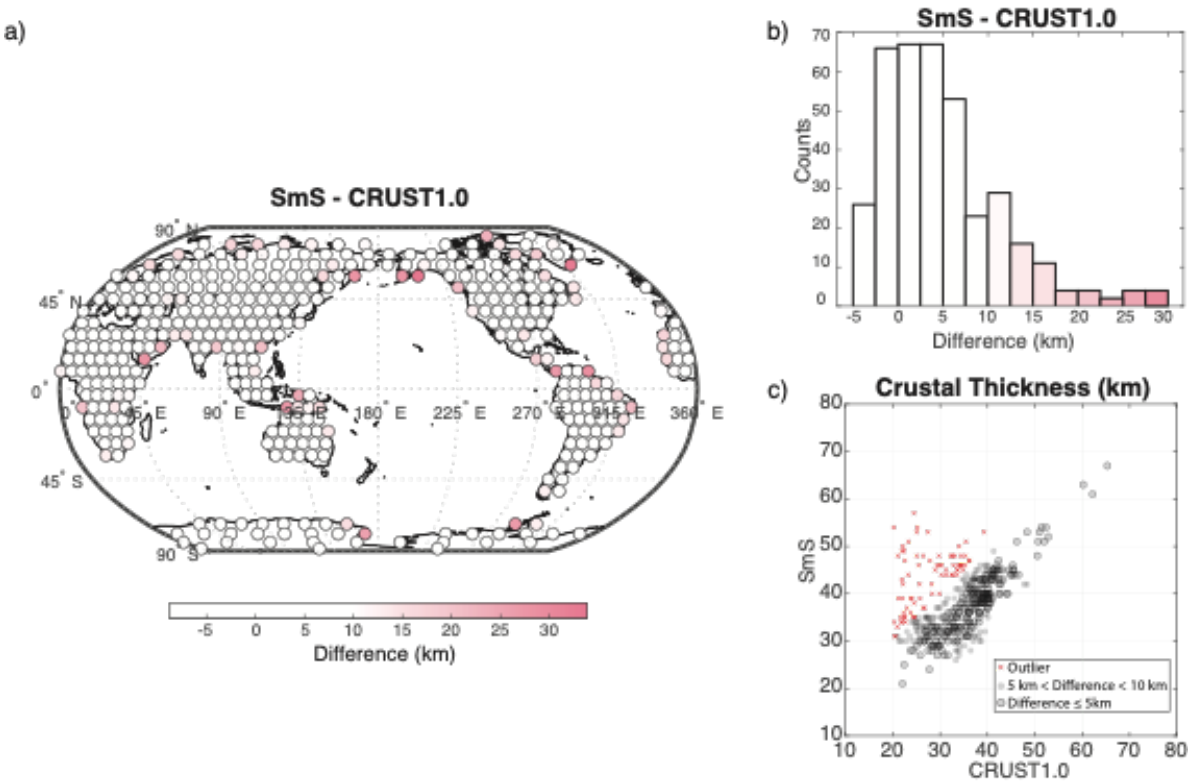

Figure 3.6 Comparisons to CRUST1.0. a) Differences between Crustal thickness from SS precursors, SmS phases, and CRUST1.0 model. b) Histogram of different crustal thicknesses between SmS and the CRUST1.0 model. c) Comparisons of Crustal thickness from SmS phases and the CRUST1.0 model. Semi-transparent dots show cases with differences of 5 - 10 km from CRUST1.0. Semi-transparent dots with outlines show cases with differences of ≤ 5 km from CRUST1.0. Red crosses show data with differences larger than 10 km, shown as pink dots in a), which are primarily in coastal regions.

3.5 4. Conclusion

We developed a new SS precursor imaging method that achieves high-resolution imaging, 6° X 6°, of discontinuities as shallow as 20 km depth. We verified that the method resolves structures as shallow as 20 km depth by applying it to AxiSEM synthetics calculated for a PREM model modified to include velocity increases at potential Moho depths between 10 and 60 km depth. We also validated the method by comparing the Moho resolved by data stacked in 6° bins to CRUST1.0. We find that we can resolve Moho depths ≥ 20 km from CRUST1.0 within the continental interior in all cases, and in 77 % of all continental regions, with outliers in coastal regions. Both synthetic and data examples demonstrate mantle transition zone discontinuities are also well resolved. Overall, this approach shows much promise for imaging discontinuity structure of other discontinuities at high resolution in the future.

Chapter 4 Global Imaging of the Mantle Transition Zone using SS precursors

4.1 Abstract

Central to our understanding of mantle convection and inner Earth material transport is the mantle transition zone. Constraints on the mantle transition zone reflect the locations and degree of material transport between the upper mantle and lower mantle. Therefore, it's essential for our knowledge of geochemical reservoirs, hydration cycles, and the evolution of the Earth. We use SS precursors to image the mantle transition zone discontinuities using seismic data from 1990 – 2021, providing excellent global data coverage. We obtain results that are in good agreement using a variety of different migration models. The major features of MTZ topographies are robust regardless of the choice of migration model. We find a thickened mantle transition zone of ~ 255 - 270 km beneath subduction zones coincident with the locations of high-velocity anomalies from tomography models. The mantle transition zone is thinned beneath oceans, although there is no apparent systematic anomalous thinning beneath hotspot regions. The 660 topographies closely resemble the mantle transition zone thickness variations, and this signal likely dominates the transition zone thickness signal. The 410 topographies do not show relationships with MTZ thickness or the 660 depths that might be expected for vertical upwellings or downwellings. This is likely because these occur at smaller lateral scales than resolved by or study, and/or convection processes are more complex than simple vertical upwellings at hotspots and downwellings at subduction zones.

4.2 Introduction

Mantle convection has broad implications for the evolution of the Earth as it drives and enables plate tectonics to occur (Landuyt & Bercovici, 2009) by slowly recycling material from the surface to the depth and vice versa. The mantle transition zone (MTZ) is the region of the mantle bounded by two prominent seismic discontinuities at approximately 410 km (the 410) and 660 km (the 660) (Dziewonski & Anderson, 1981). For several reasons, the properties of the MTZ are central to our understanding of mantle convection. 1) Separating the upper mantle and lower mantle, the MTZ could act as a filter for any material moving in between (Bercovici & Karato, 2003). 2) Meanwhile, the MTZ has the capacity to store huge amounts of water up to several oceans worth (Hirschmann & Dasgupta, 2009). 3) With a higher water solubility in the MTZ, the top of the MTZ (and/or the shallow lower mantle) may be a region of widespread deep melts (Bercovici & Karato, 2003; Schmandt et al.,

2014), which may act as geochemical reservoirs and/or alter mantle viscosity. Despite its importance, placing tight constraints on the MTZ is challenging.

The precise amount and location of material transfer between the upper mantle and lower mantle is debatable. Seismic observations have generally provided evidence for massive material transport across the MTZ (e.g., Grand et al., 1997; Nolet et al., 2007; Shearer, 1993), though the geochemical differences between ocean island basalt from the lower mantle in comparison to mid-ocean ridge basalt from the upper mantle were classically used to argue little material transfer between the upper and lower mantle (e.g., Hofmann, 1997; Kellogg et al., 1999).

The two seismic jumps that bound the MTZ are typically interpreted as the pressure-induced transformation of olivine grains into denser crystal structures, as predicted by laboratory experiments: in general, α olivine to wadsleyite at the 410 with a positive Clapeyron slope (Bina & Helffrich, 1994)and ringwoodite to bridgmanite and magnesiowüstite at the 660 with a negative Clapeyron slope (Ringwood, 1975). Therefore, the topography of the MTZ boundaries and the thickness of the MTZ reflect the corresponding thermal conditions. The typical paradigm includes a thin MTZ in hot regions where upwellings occur and a thick MTZ in cold regions where downwelling occurs (Houser, 2016; Tauzin & Ricard, 2014).

Hotspots and subduction zones are typically regarded as the places where material transfer between the upper and lower mantle occurs, with vertical upwelling beneath hotspots and vertical or sub-vertical descending beneath subduction zones. Seismic tomography models also find slow velocities interpreted as ascending material beneath hotspots and fast velocities associated with descending material beneath subduction zones (Nolet et al., 2007). Some seismic imaging of MTZ discontinuities generally reflects classical mineral physics predictions for thickening beneath subduction zones and thinning beneath hotspots (Gu & Dziewonski, 2002; Houser et al., 2008; Lawrence & Shearer, 2006; Lawrence & Shearer, 2008).

Nonetheless, geochemical evidence, including isotopic differences between ridges and hotspots and bulk compositional discrepancies between the predictions and observations of Earth's interior layering and atmosphere (Hofmann, 1997) suggest greater complexity than large, long-lived full mantle convection, i.e. a well-mixed mantle. Pockets of enrichment, chemical piles, layering of stagnant slabs (Ballmer et al., 2017; Jellinek & Manga, 2004; Kellogg et al., 1999; Marquardt & Miyagi, 2015; Morgan & Morgan, 1999), or stable high-viscosity lower-mantle convective cells (Ballmer et al., 2017) are possible explanations.

Seismic observations have also been used to argue for greater complexity than the simple vertical ascent of material beneath hotspots. Some global seismic tomography images have been inferred to reflect deflected upwellings or tree-like upwelling structures (French & Romanowicz,

2015; Tsekhmistrenko et al., 2021). Seismic imaging of slow velocity regions or MTZ thinning in alternative locations away from hotspots has been used to argue for alternative locations of material ascent (Agius et al., 2021; Dai et al., 2023; Inoue et al., 2006; Suetsugu et al., 2006). However, it has also been suggested that some of the observations may also be related to nearby plume material (Portner et al., 2017; Zhao et al., 2013) or be artefacts of tomographic inversion (Bezada et al., 2016). Alternatively, the mantle may pervasively rise across the MTZ but typically be compositionally filtered during the process (Bercovici & Karato, 2003). However, since more intricate convection and alternative locations of material transfer across the MTZ may be implied, tight constraints on the MTZ are required.

The SS phase and its precursors S410S and S660S correspond to S-wave reflections at the surface and corresponding MTZ discontinuities, respectively. Sampling the mid-point of the ray path, they provide excellent global coverage, especially for the oceans that cover ~ 70% of the Earth's surface, where the instrument coverage is sparse. Taking advantage of SS precursors and the seismic observations from the past decades, we image the global MTZ discontinuities and compare them with different seismic tomography models.

4.3 Data and Method

4.3.1 Data

We used records from global broadband seismometers (9165 stations) deployed over the past three decades. The data set incorporated a global catalogue of earthquakes (6111 events) with magnitudes larger than 5.5 M_w and with source depths no larger than 30 km from 1990 to 2021 (Figure 4.1a). We removed the instrument responses from the seismograms and rotated them to radial and transverse components. We considered only the transverse components. To avoid the strong interferences of topside reflections such as Ss410s and Ss660s, we restricted the event-to-station epicentral distance to between 120° and 170°.

We followed the work of Dai et al. (2024) to process the data, as summarised here. We converted all transverse seismograms from displacement to acceleration, and then Hilbert transformed them to produce symmetric SS pulses (Oppenheim & Schafer, 1975a; Rychert & Shearer, 2010a). We applied a bandpass filter from 0.05 Hz to 0.2 Hz to all data. We centred the waveforms on the SS phase, which was picked as the maximum positive or negative amplitude in a 10-s time window before and after the theoretical SS arrival time. The amplitude of the centred waveform was normalised to unit amplitude. We computed the signal-to-noise ratio (SNR) for each record as the ratio of the maximum amplitude of the seismic phase to the standard deviation in a time window 270

s to 30 s preceding the SS phase. Incomplete records and records of SNR smaller than 2.5 were discarded.

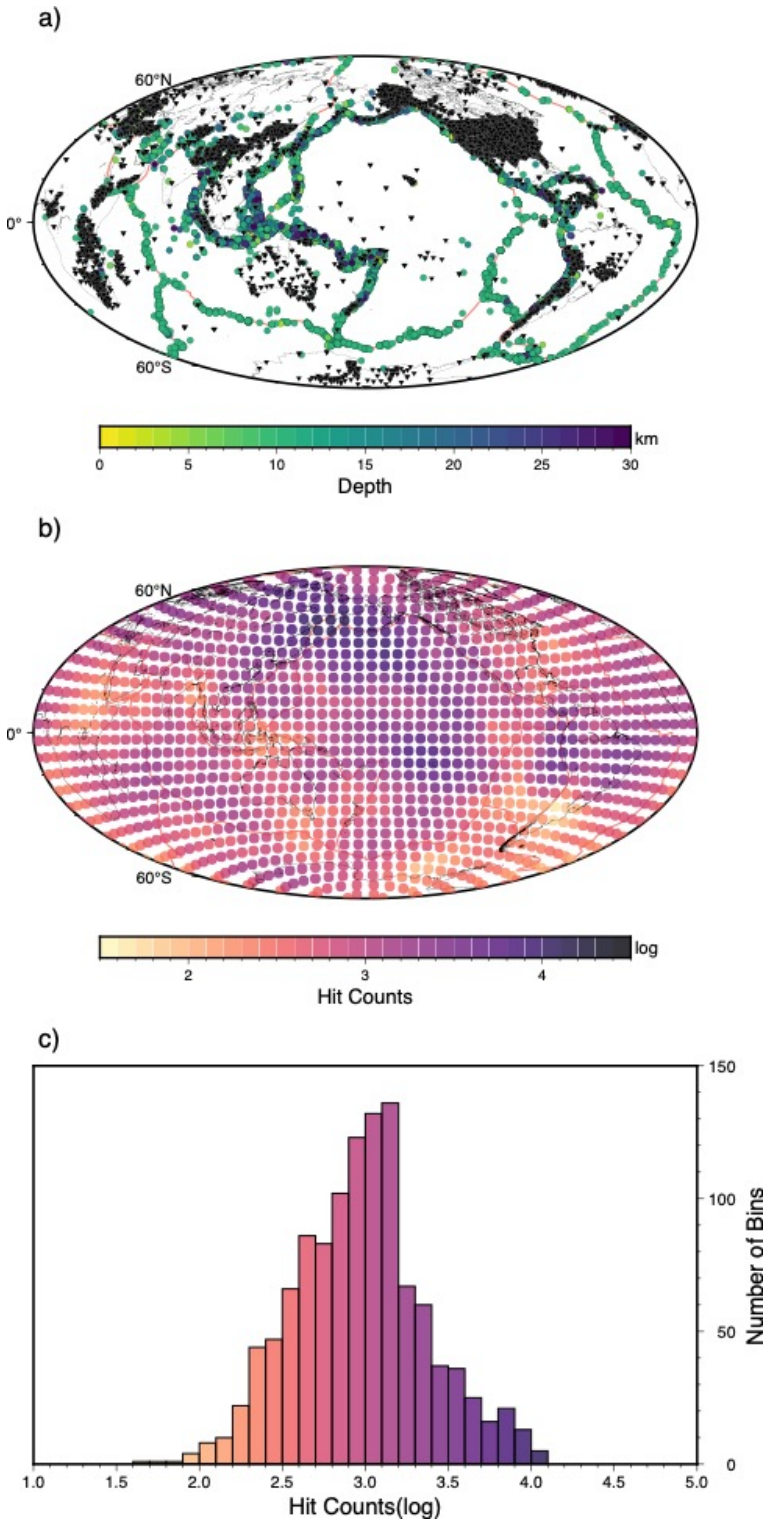

Figure 4.1 Data and coverage. a) Inversed black triangles show broadband seismic stations, and circles represent earthquakes with colours showing their source depths. Orange lines show plate boundaries (Bird, 2003), same as in b). b) The bin scheme used for stacking processed SS precursors and colour shows the number of bounce points in each bin used for the final imaging. c) Histograms of hit counts in bins.

4.3.2 Deconvolution

To sharpen the precursors, we deconvolved the stacked source *S* phases from the above processed *SS* waveforms as the *SS* phases are Hilbert transformed relative to the *S* phases (Choy & Richards, 1975). We created event *S*-wave source stacks for each event that would be deconvolved from the corresponding individual *SS* waveforms (Rychert & Shearer, 2011; Tharimena et al., 2017a; Tharimena et al., 2017b; Tharimena et al., 2016). We followed similar processing steps described above for the *SS* phases to process the *S*-wave source stacks. We used seismic records from 1990 to 2021, with epicentral distances of 25° - 80°, for events with magnitudes $M_w > 5.5$, and source depths < 75 km. We resampled the data to 10 Hz and then applied a band-pass filter with corners at 0.02 and 0.5 Hz as well. Waveforms with SNR < 2.5 were rejected. We centred the signals at the *S* phase and normalised them to unit amplitude. Finally, we stacked the source wavelets from all global receivers for a particular seismic event to produce the source stacks. We performed the deconvolution using an extended time multitaper frequency domain deconvolution method (Helffrich, 2006; Rychert et al., 2012a; Shibutani et al., 2008).

4.3.3 Migration and stacking

We converted each impulse response from the time domain to the depth domain. We tested 2 1-D mantle models, 1-D reference model IASP91(Kennett & Engdahl, 1991) with and without crustal corrections from CRUST1.0 (Laske et al., 2013). We also applied the crustal correction and used four 3-D tomography models, including models SP12RTS (Koelemeijer et al., 2016), S362ANI+M (Moulik & Ekström, 2014), SGLOBE-rani (Chang et al., 2015), and SEISGLOB2 (Durand et al., 2017) , which shared the same normal mode and overtone data combined with different types and combinations of surface wave and body wave data and tomography methods to resolve the entire mantle. We calculated the theoretical ray paths using IASP91 via the TauP toolkit (Crotwell et al., 1999) and extracted velocities along the ray paths. Then, we computed the differential travel times of the SS phase and S410S/S660S to migrate the deconvolutions to the depth domain.

We divided the surface of the Earth into evenly distributed 6° circular bins, resulting in 1146 bins. For each bin, we stacked SS waveforms of bounce points within 10°, roughly the size of the first Fresnel zone of SS waveforms, from the centre of the bins, resulting in roughly 30% overlap among the bins. We required the migrated deconvolution signals of high similarity (with average Euclidean distance between waveform pairs < 4) within each other to construct the SS stack. In total, we used 192,981 seismic records, giving an improved spatial coverage over previous studies (Figure 4.1b, c). Each bin stack consisted of 41 – 11,208 signals, and more than half of them were constructed by more than 900 signals. Then, the depths of the 410 and the 660 were determined by searching for

the nearest positive peaks around the nominal discontinuity depth in a 100-km window. Figure 4.2 shows a stacking profile along 45° N.

We examined spatial relationships between transition zone structure with surface tectonic features such as subduction trenches and mid-ocean ridges to determine the extent where shallow mantle downwelling and upwelling are linked to transition zone upwelling and downwelling. For subduction zones, we also wanted to examine the relationships with past subduction locations and present-day transition zone anomalies. The hypothesis is that slabs fall mostly vertically through the upper mantle, driven via the negative buoyancy, so the trench location through time should be a good predictor of where slabs stagnate in the mantle transition zone.

We extracted the subduction zone locations from a recent plate reconstruction model over the past 250 Myr in 1 Myr increments (Müller et al., 2019) using GPLATES software (Müller et al., 2018). Present-day mid-ocean ridge locations were determined from a plate boundary model (Bird, 2003) and seafloor ages (Müller et al., 2008). We determined the minimum geodetic distance at the surface of the Earth from a given bin to the subduction trench or ridge location. This distance was then used to bin the data and for hypothesis testing.

We used a paired sample t-test to examine the significance of a difference in the mean of the transition zone thickness, depth of the 410 or depth of the 660 between bins that were within 600 km or one bin distance of a trench or ridge and all other bins further away. We examined each result from the different migration models. If the t-test passed, we would reject the null hypothesis that the means were equal at a given confidence interval. We assumed unequal variances for the populations and used Satterthwaite's approximation (Satterthwaite, 1946) for degrees of freedom.

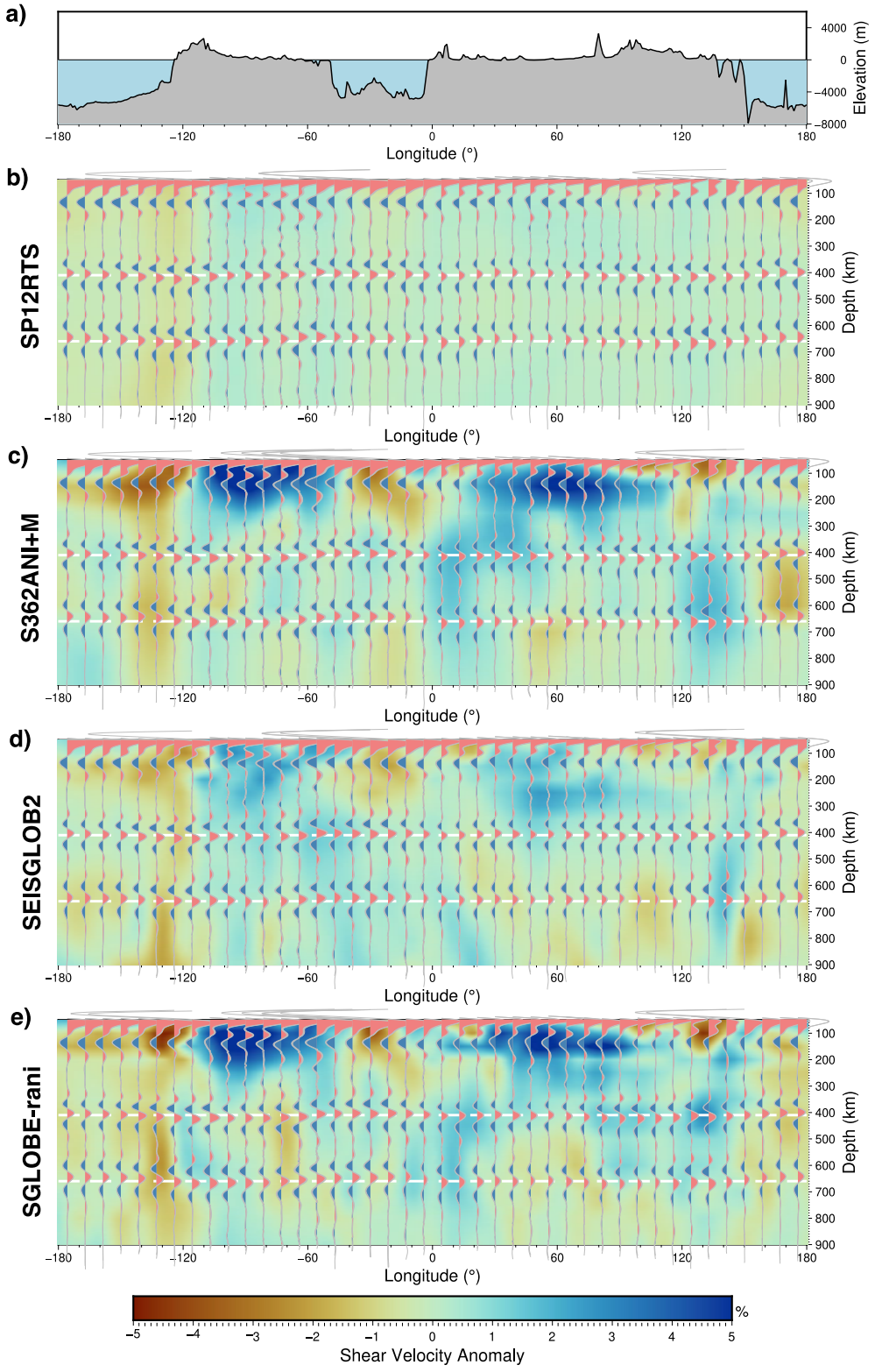

Figure 4.2 Cross sections along 45° N. a) Elevations along 45° N. b) Colours show shear velocity perturbations from SP12RTS. Wiggles show deconvolution stacks migrated with the corresponding 3-D model along the cross-section, with red showing positive amplitudes and blue for the negative, grey showing uncertainty. c) – e) Same as a), but results from S362ANI+M, SEISGLOB2, and SGLOBE-rani, respectively.

4.4 Results

4.4.1 Migration model

The crustal corrections uplift the 410 and the 660 by ~ 2 km on average, whereas the mantle heterogeneity corrections play a bigger role, depressing the 660 by 3 - 7 km on average and the 410 by 7 - 8 km on average compared to the results with crustal corrections only (Figure 4.3 – 4.5).

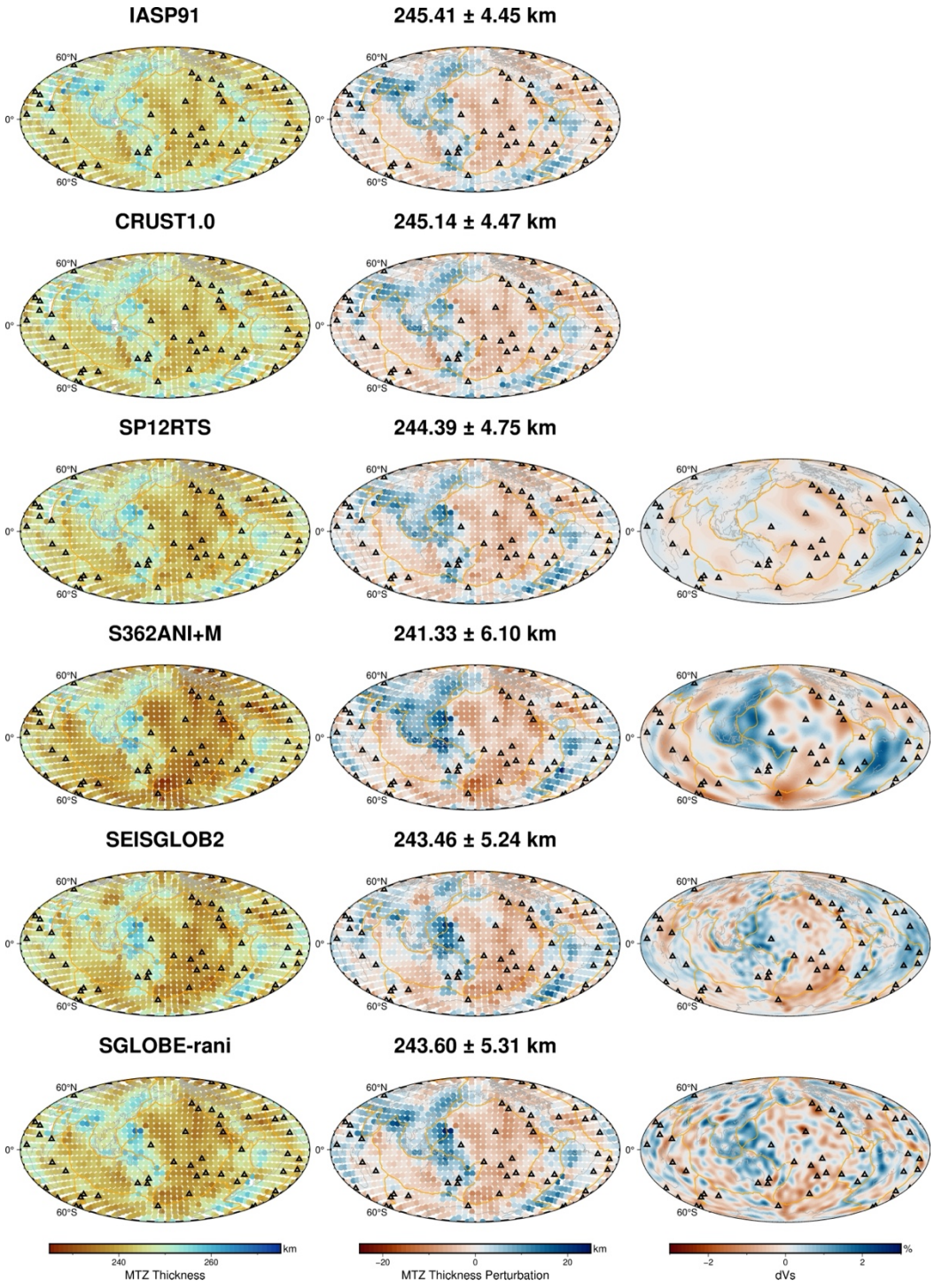

Figure 4.3 Maps of MTZ thickness and shear velocity anomalies. Left panels: coloured dots show the MTZ thickness measured in each bin from migration using only 1-D reference model

IASP91, crustal corrections with CRUST1.0 only, and models with crustal corrections using CRUST1.0 and upper mantle corrections using SP12RTS, S362ANI+M, SEISGLOB2, SGLOBE-rani. Middle panels: MTZ thickness perturbations to the mean (as titled above with its standard deviation) for each model. Right panels: average velocity anomalies from 395 - 690 km from corresponding 3-D velocity models. Orange lines show plate boundaries (Bird, 2003), and black triangles indicate major hotspots (Courtillot et al., 2003).

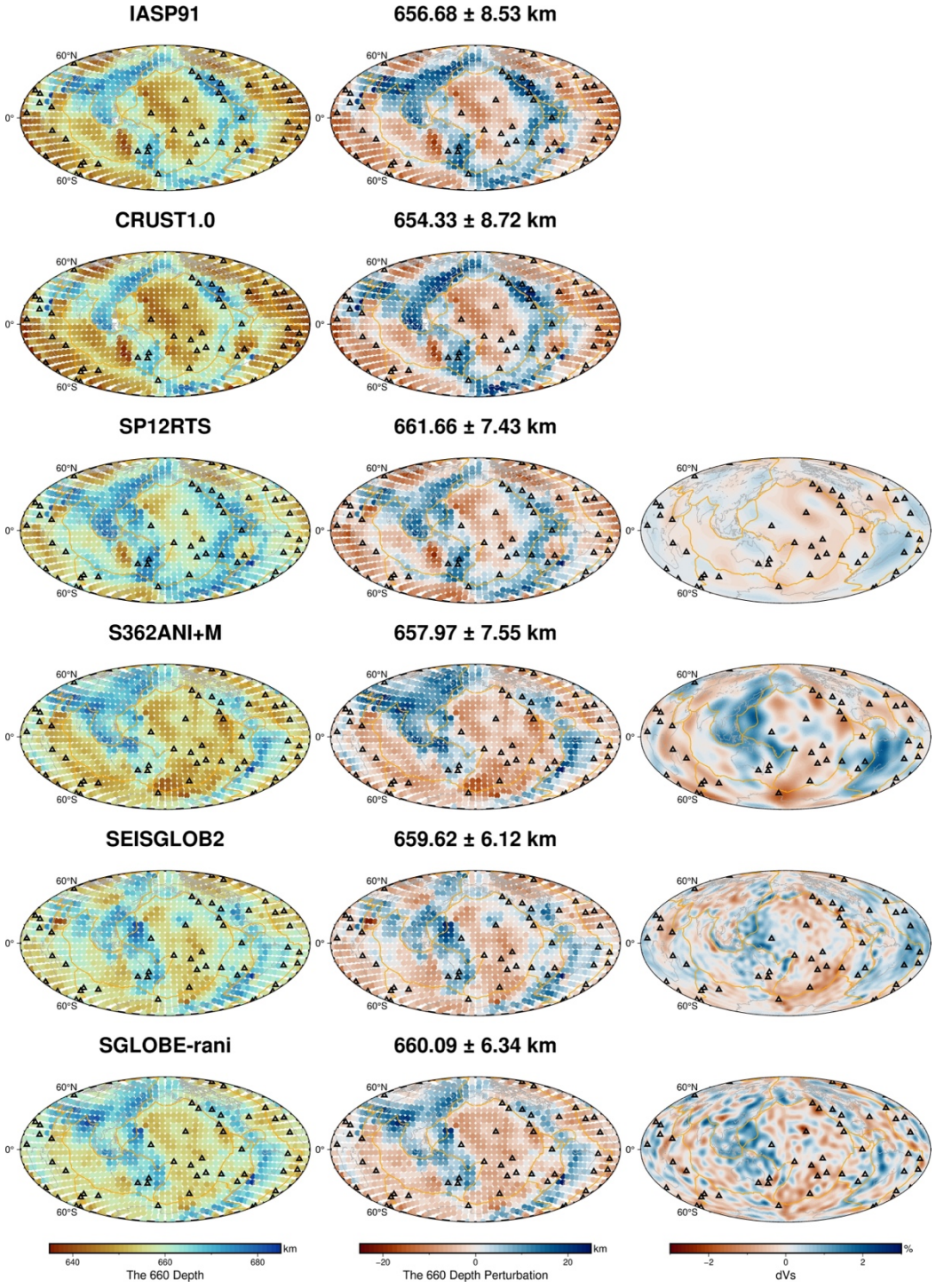

Figure 4.4 Maps of the 660 topography and shear velocity anomalies. Left panels: coloured dots show the 660 depths measured in each bin from migration using only 1-D reference model

IASP91, crustal corrections with CRUST1.0 only, and models with crustal corrections using CRUST1.0 and upper mantle corrections using SP12RTS, S362ANI+M, SEISGLOB2, SGLOBE-rani. Middle panels: the 660 topography perturbations to the mean (as titled above with its standard deviation) for each model. Right panels: average velocity anomalies from 635 - 690 km from corresponding 3-D velocity models. Orange lines show plate boundaries (Bird, 2003), and black triangles indicate major hotspots (Courtillot et al., 2003).

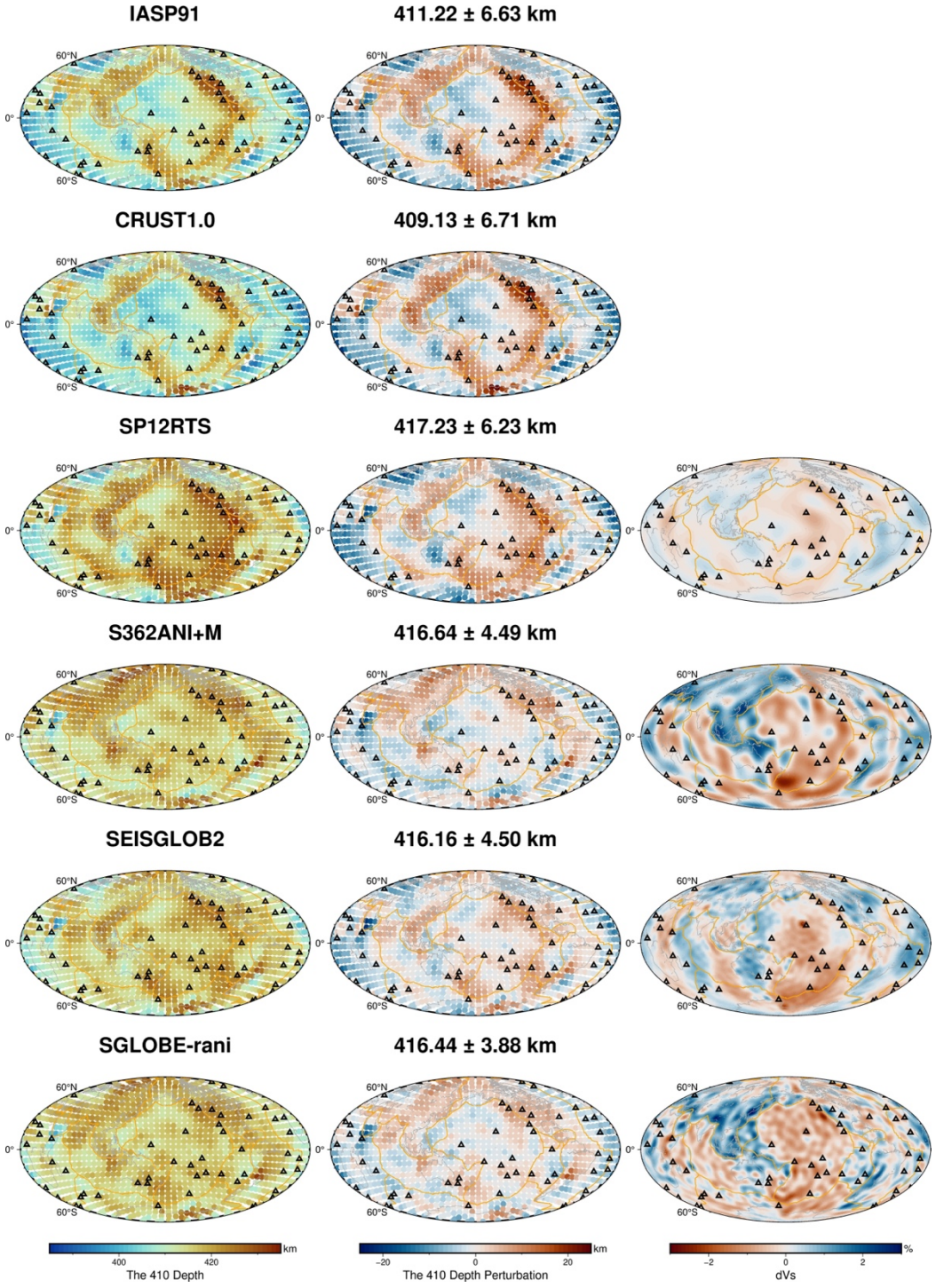

Figure 4.5 Maps of the 410 topography and shear velocity anomalies Left panels: coloured dots show the MTZ thickness410 depths measured in each bin from migration using only 1-D

reference model IASP91, crustal corrections with CRUST1.0 only, and models with crustal corrections using CRUST1.0 and upper mantle corrections using SP12RTS, S362ANI+M, SEISGLOB2, SGLOBE-ani. Middle panels: the 410 topography perturbations to the mean (as titled above with its standard deviation) for each model. Right panels: average velocity anomalies from 395 - 435 km from corresponding 3-D velocity models. Orange lines show plate boundaries (Bird, 2003), and black triangles indicate major hotspots (Courtillot et al., 2003).

The main differences between the absolute discontinuity depths in the 1-D migrations and those in the 3-D migrations occur beneath the oceans, where the MTZ is thinner in the 3-D migration models. However, when the perturbation to the mean MTZ thickness is considered, no systematic difference is apparent between the thicknesses from the 1-D and the 3-D migrations. The main difference between the depths of the 660 from the 1-D migration and those from the 3-D migration is that the oceanic regions are more uplifted, particularly beneath the ridges in the 3-D models, except for SP12RTS, which has the most muted mantle velocity anomalies in comparison to the other models. When the perturbation to the mean is considered, the effect is primarily beneath ridges, which are again shallower in the 3-D migration models. The main difference between the 410 depths from the 1-D and the 3-D migrations is that the 410 is more depressed beneath the oceans in the 3-D models. When the perturbation to the mean is considered, the 410 is shallower beneath the ridges in comparison to the 1-D models, and it is also shallower in general in oceanic regions than the 1-D migration. The overall effect is that the intensities of the 410 relative anomalies are reduced in the 3-D models in comparison to those of the 1-D models.

The discontinuity depths and estimated mantle transition zone thickness are mostly correlated among the 3-D migration models, with thicknesses being best correlated and 410 being least correlated. MTZ thicknesses are correlated among 3-D migration models with coefficients of 0.85 - 0.9 (Figure 4.6). The 660 depths are correlated at 0.5 - 0.9 among the 3-D migration models (Figure 4.7), and the 410 depths are both not well-correlated and correlated among 3-D migration models with coefficients of 0.3 - 0.9 (Figure 4.8).

The 3-D migrations reduce the positive correlation between the 410 and the 660 discontinuity depths. In the 1-D migrations, there are correlations of > 0.8. For the SP12RTS model, which has more muted anomalies than the other 3-D models, the correlation is 0.8. Whereas the correlation coefficient for the remaining 3-D models is 0.5 - 0.6 (Figure 4.9). This makes the 3-D migrations more ideal for discussion purposes because the 3-D migrations have reduced the artificial positive correlation between the discontinuity depths caused by variations in upper mantle structure.

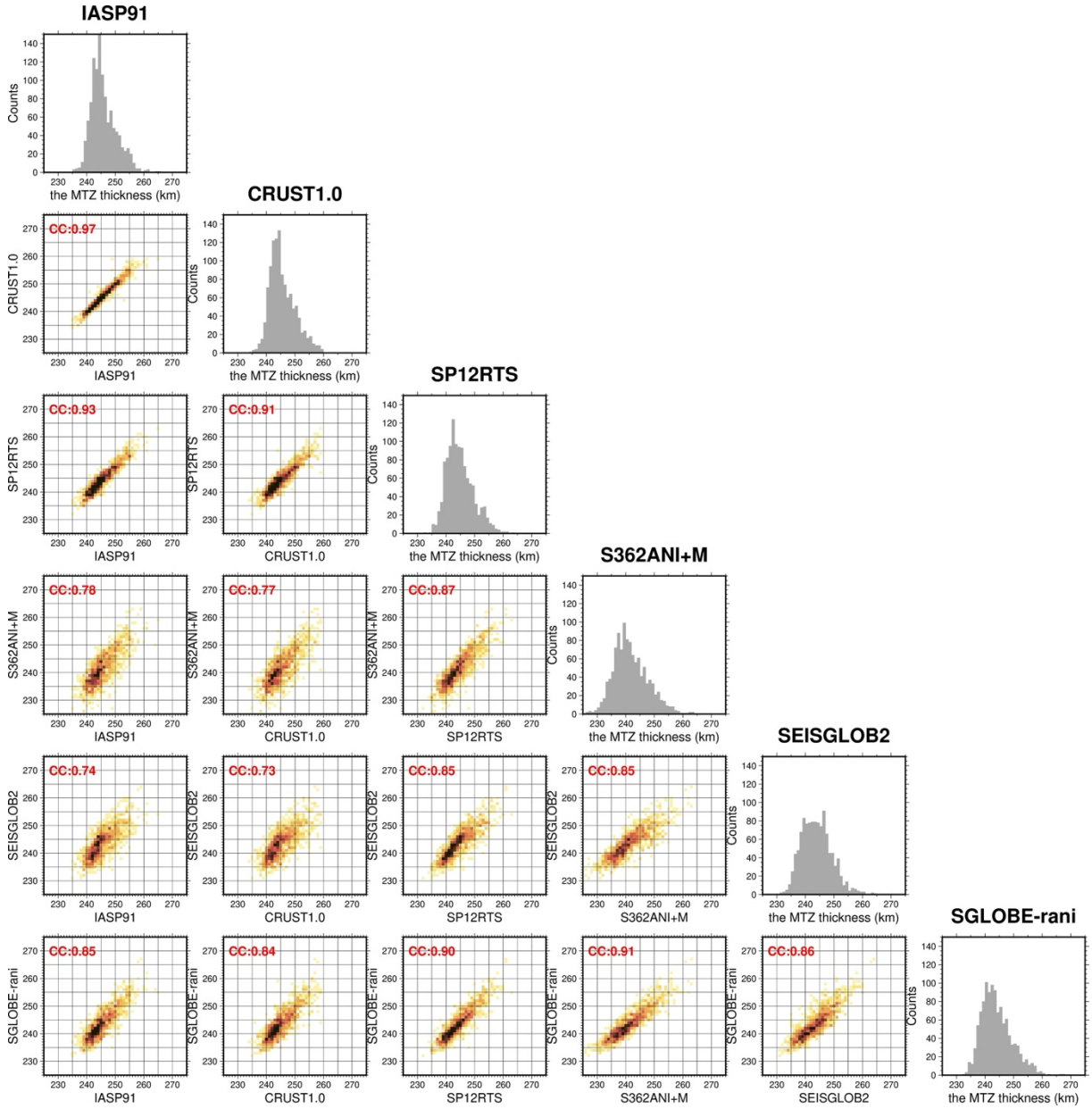

Figure 4.6 MTZ thicknesses comparisons. Diagonal panels show the histograms of the MTZ thicknesses from different models. Panels in the lower triangle show 1 vs. 1 of MTZ thickness from different models. Darker colours show larger counts and vice versa. Pearson correlation coefficients are shown in the top right corner.

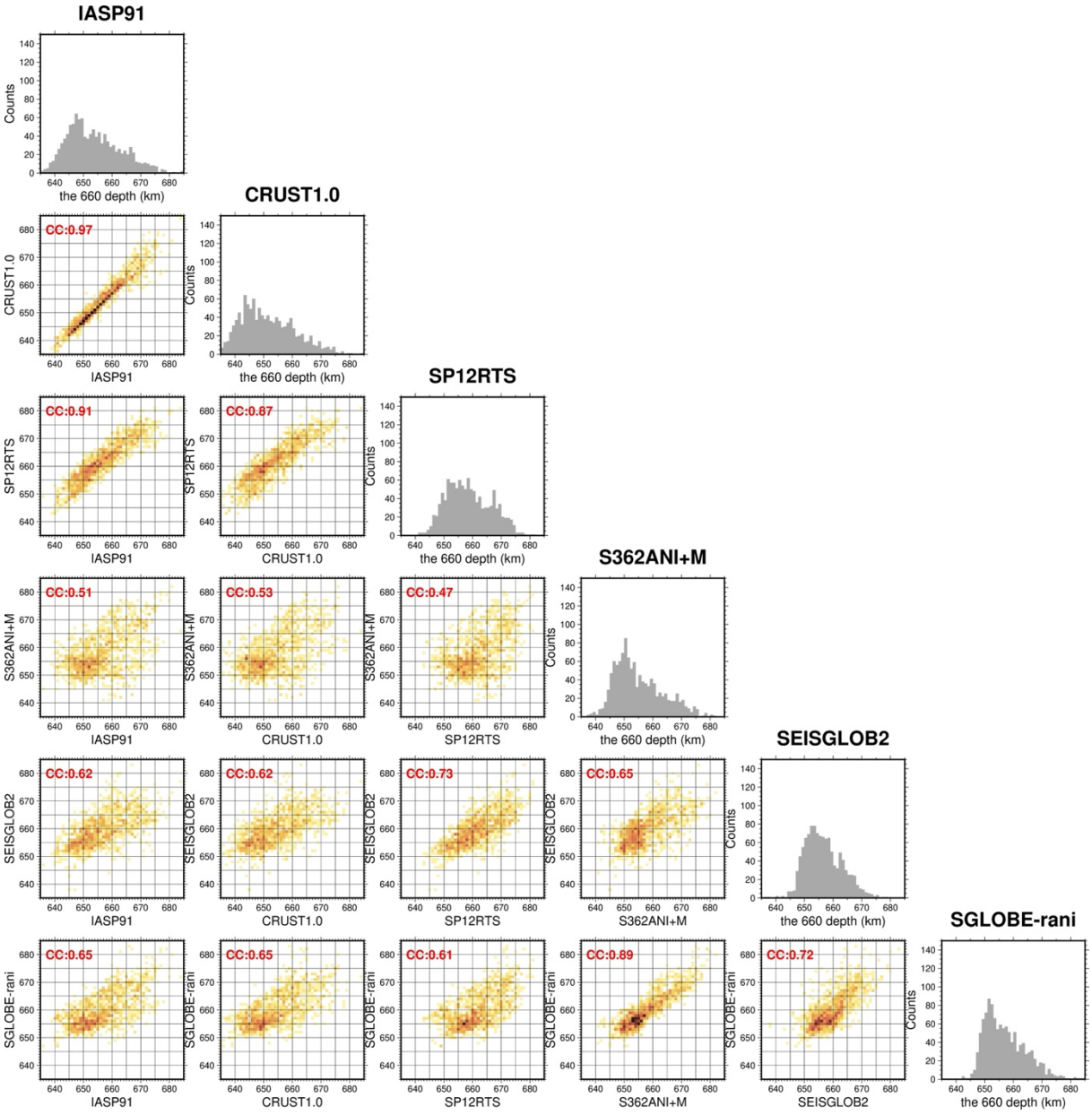

Figure 4.7 the 660 topography comparisons. Diagonal panels show the histograms of the 660 depths from different models. Panels in the lower triangle show 1 vs. 1 of the 660 depths from different models. Darker colours show larger counts and vice versa. Pearson correlation coefficients are shown in the top right corner.

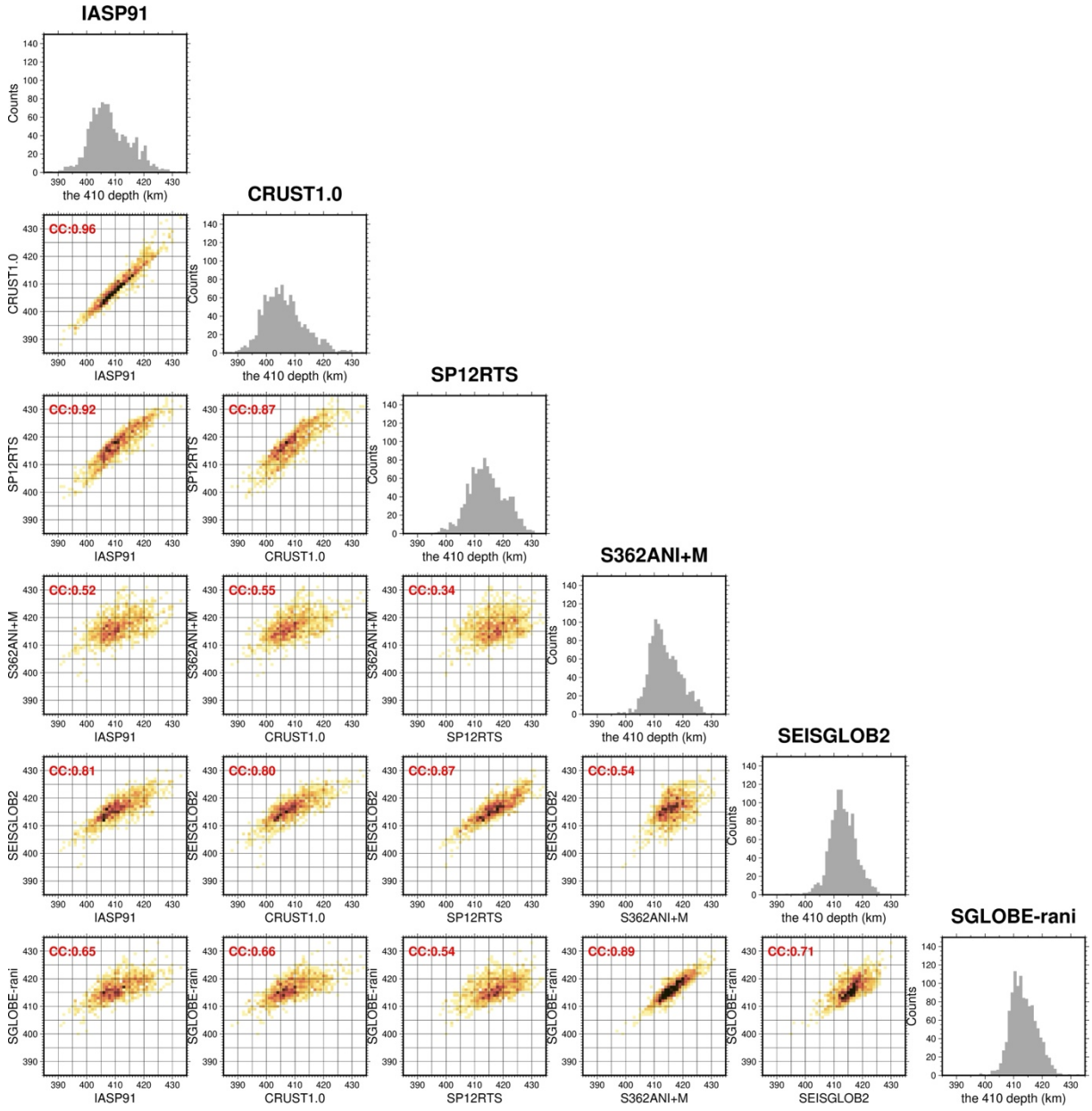

Figure 4.8 the 410 topography comparisons. Diagonal panels show the histograms of the 410 depths from different models. Panels in the lower triangle show 1 vs. 1 of the 410 depths from different models. Darker colours show larger counts and vice versa. Pearson correlation coefficients are shown in the top right corner.

4.4.2 The MTZ thickness

The average MTZ thickness from the 1-D migrations is 245 km ± 4 km using IASP91 and 245 ± 5 km using IASP91 and a crustal correction (Figure 4.3). The average MTZ thicknesses using the 3-D mantle velocity models range from 241 ± 6 km from S362ANI+M to 244 ± 5 km from model SP12RTS, again within error of each other and the 1-D migrations (Figure 4.3). The ranges of the 1-D migrations are 235 - 265 km and 234 - 259 km for IASP91 and IASP91 with a crustal correction, respectively. The ranges for the 3-D models are 232 - 263 km for the S12RTS, 226 - 281 km for S362ANI+M, 231 - 264 km for SEISGLOB2, and 232 - 267 km for SGLOBE-rani.

The MTZ thicknesses and 660 depths share a similar pattern and are correlated at 0.5 to 0.8 for the 3-D model migrations, whereas MTZ thicknesses are not well correlated with the 410, with coefficients of 0.0 - 0.2 (Figure 4.9).

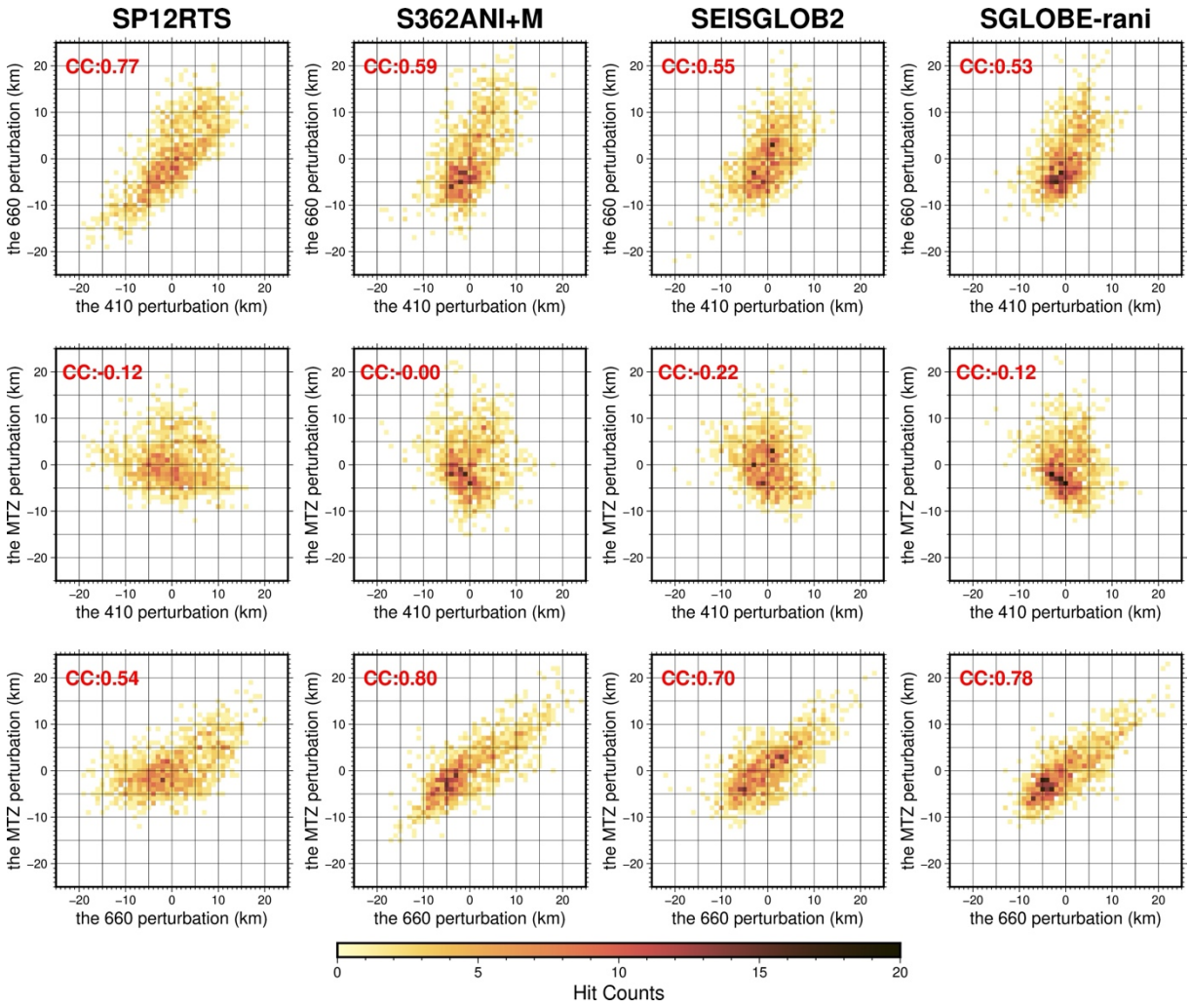

Figure 4.9 1 vs. 1 of MTZ topographies. Top panels: 1 vs. 1 of the 410 and the 660 of individual models with crustal and mantle correction. Middle panels: 1 vs. 1 of the 410 and the MTZ thickness. Bottom panels: 1 vs. 1 of the 660 and the MTZ thickness. Pearson correlation coefficients are shown in the top right corner.

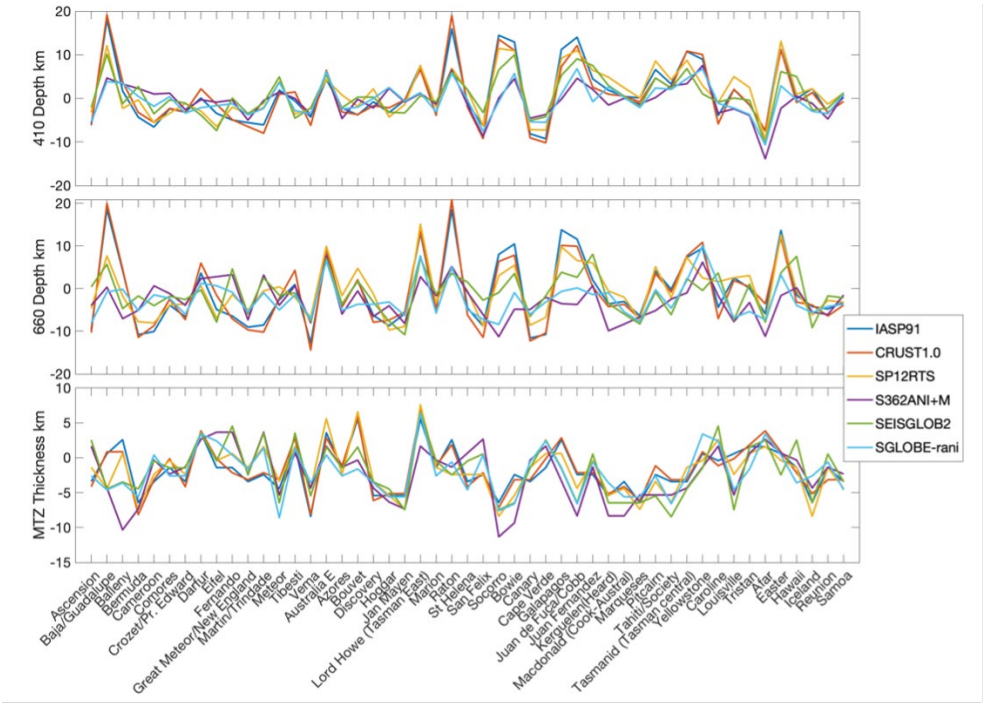

Figure 4.10 Depth and thickness of transition zone discontinuities beneath hotspots relative to the mean. The top panel shows the 410 perturbations for hotspots listed in the Courtillot et al. (2003) compilation. Hotspots are sorted left to right with increasing ranking from Courtillot et al. (2003) , and the coloured lines correspond to the different migration models indicated in the legend. The middle panel shows the 660 perturbations, and the bottom panel shows the MTZ thickness perturbation.

All models show a relatively thin MTZ, 232 - 226 km, beneath the majority of oceans (61% - 72%). The mean thickness in the bins closest to hotspots is within ~2 km of the mean and, therefore not significantly different. The transition zone is also thinner beneath the Mid-Atlantic Ridge than the older seafloor, passing the t-test for all migration models. Whereas the Pacific and Indian oceans only past this test for 3/6 and 2/6 of models, respectively (Figure 4.11 – 4.13).

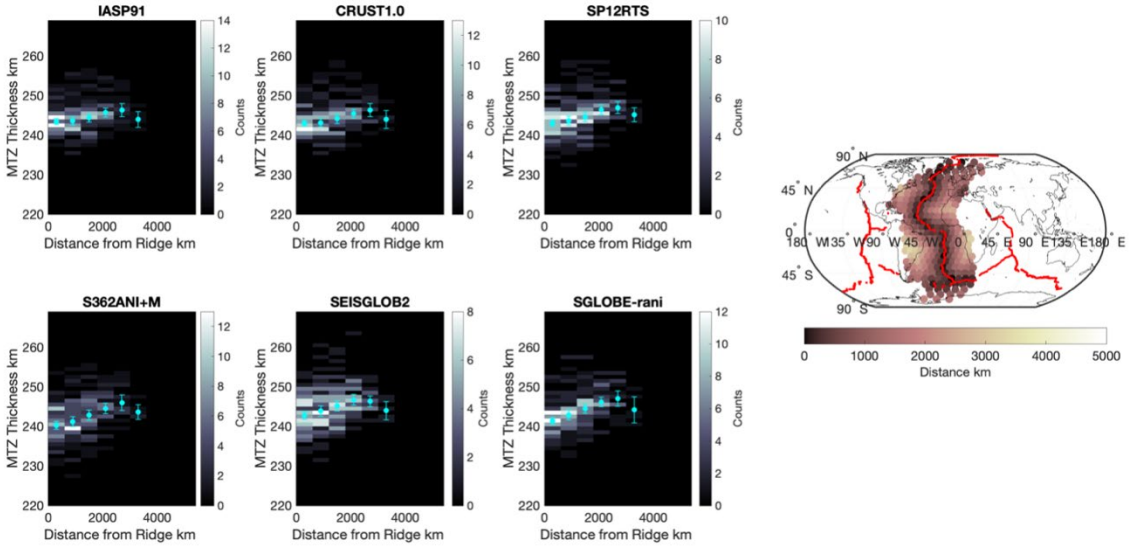

Figure 4.11 Histograms of MTZ thickness vs. distance from the Atlantic mid-ocean ridge for the different migration models. Migration model is indicated above each panel, cyan circles with error bars show the mean and standard error of the mean of each 600 km distance bin. Map on the right indicates the ridge location in red, and the bins coloured by distance to the ridge included in the histograms.

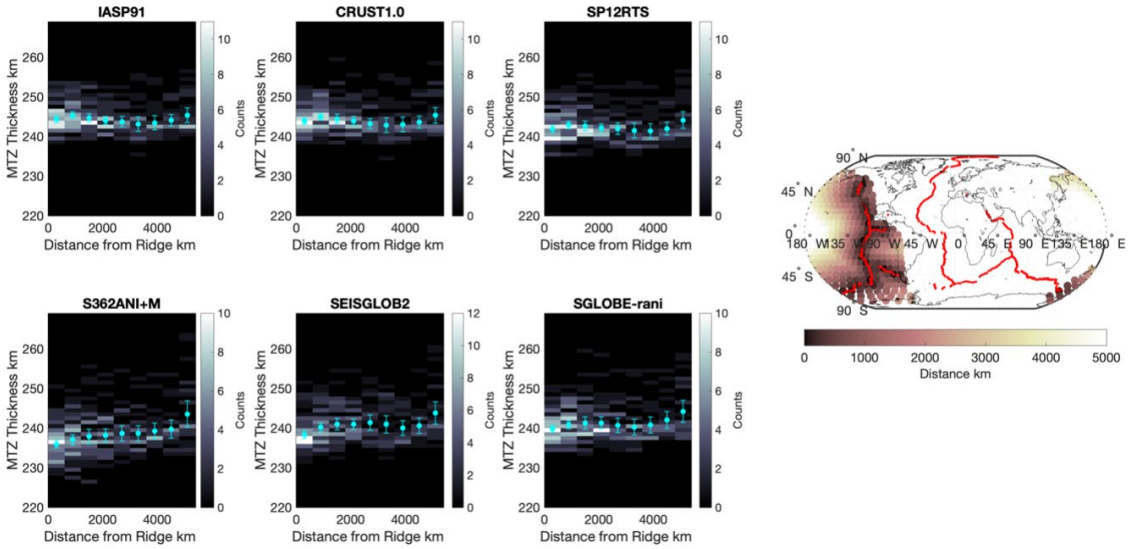

Figure 4.12 Histograms of MTZ thickness vs. distance from the Pacific mid-ocean ridge system for the different migration models. Migration model is indicated above each panel, cyan circles with error bars show the mean and standard error of the mean of each 600 km distance bin. Map on the right indicates the ridge location in red, and the bins coloured by distance to the ridge included in the histograms.

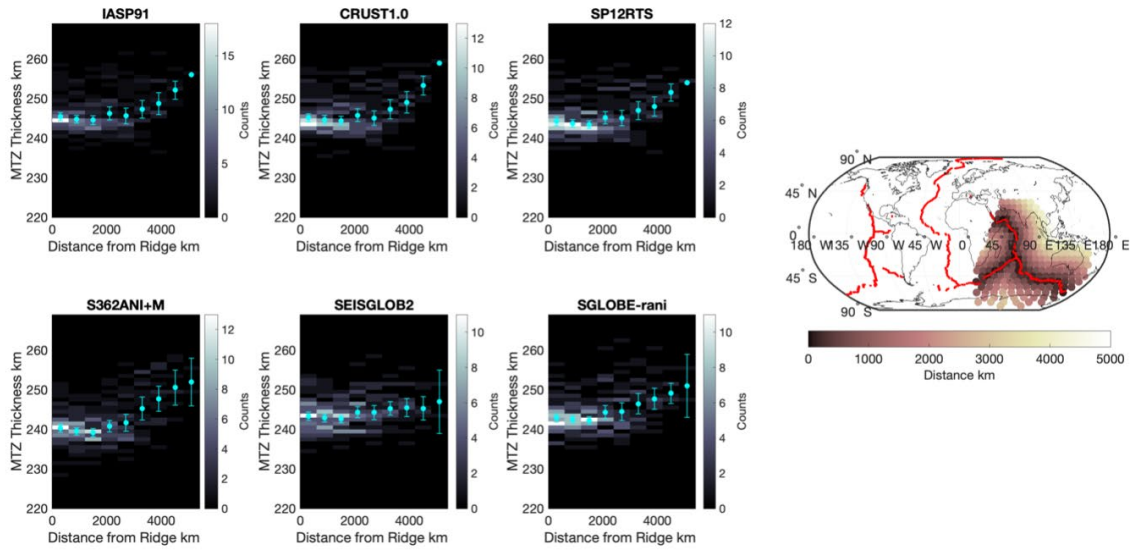

Figure 4.13 Histograms of MTZ thickness vs. distance from the Indian mid-ocean ridge system for the different migration models. Migration model is indicated above each panel, cyan circles with error bars show the mean and standard error of the mean of each 600 km distance bin. Map on the right indicates the ridge location in red, and the bins coloured by distance to the ridge included in the histograms.

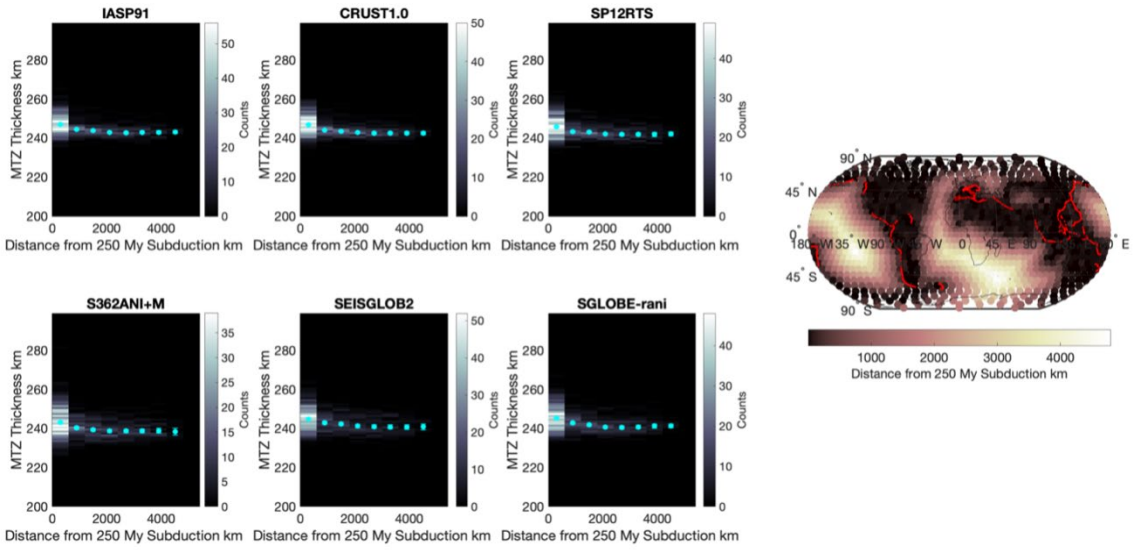

Figure 4.14 Histograms of MTZ thickness vs. distance from the paleo trench locations for the different migration models. Migration model is indicated above each panel, cyan circles with error bars show the mean and standard error of the mean of each 600 km distance bin. Map on the right indicates the current trench location in red, and the bins are coloured by distance to the paleo trenches used in the histograms.

All models show a thick MTZ, 252 - 267 km, beneath ocean-continent subduction zones, including those in South America, the western Pacific, and the Alpine subduction zone (Figure 4.2, 4.13). Thickening beneath Cascadia is absent or less strong or pervasive, depending on the model. The MTZ beneath the Tibetan Plateau and Central Asia is also thickened to ~260 km. Most thickened MTZ bins are located beneath current or paleo trench locations, as follows: IASP91 80%, IASP91 with crustal correction 81%, SP12RTS 73%, S362ANI+M 70%, SEISGLOB2 66%, and SGLOBE-rani 73%. The thick bins that are not located beneath the paleo trenches are located east of South America and beneath western South Africa, with some scattered bins in Antarctica, the Pacific and Europe. All models passed the t-test comparing MTZ thickening nearby current and paleo trenches to more distant locations, suggesting the bins beneath trenches are on average thicker (Figure 4.14).

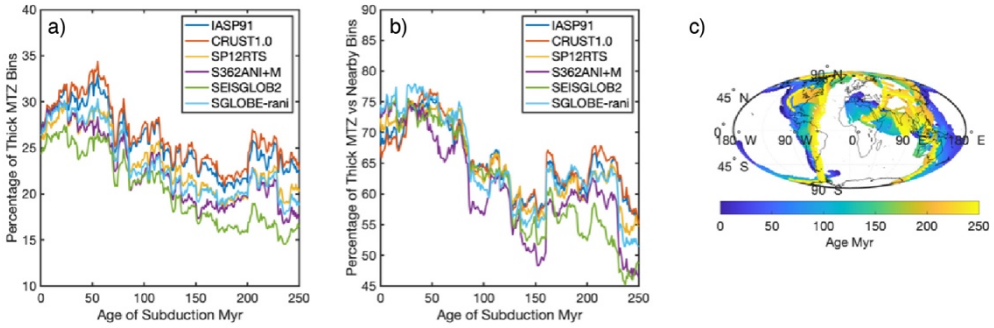

Figure 4.15 Percentages of thicker than average bins relative to the total thicker than average bins a) and relative to the bins nearby (<600 km) a paleo trench b) as a function of age of subduction (or paleo trench age). Coloured lines indicate the migration model used indicated in the legend. c) Paleo trench locations as a function of age.

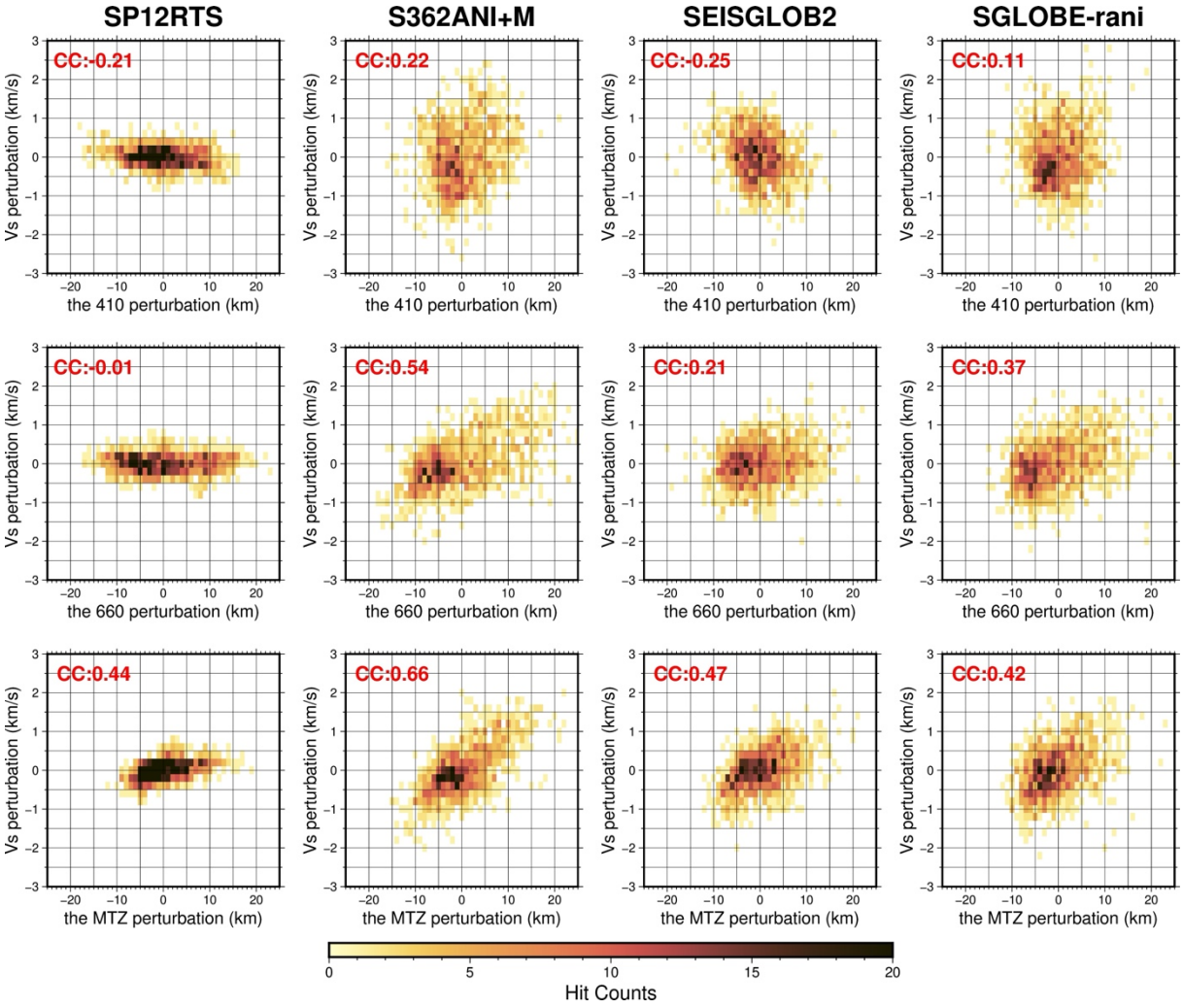

Figure 4.16 Velocity vs. MTZ topography and thickness. Top panels: The 410 vs. velocity anomalies vertically averaged from 395 – 435 km of individual models with crustal and mantle correction. Middle panels: The 660 vs. velocity anomalies vertically averaged from 635 – 690 km. Bottom panels: The MTZ thickness vs. velocity anomalies vertically averaged from 395 – 690 km. Pearson correlation coefficients are shown in the top right corner.

There are locations beneath paleo trenches that do not have thicker MTZs. The number of thicker than average bins relative to the total number of deeper-than-average bins increases from 0 - 10 Myr, plateauing at ~ 28 - 35% depending on the migration model from 10 - 70 Myr, and there is a relatively constant percentage from 19 - 25% depending on the migration model at > 70 Myr (Figure 4.15). The number of thicker than average bins relative to the number of bins nearby current or paleo trench locations of a given age has a similar pattern. The percentages increase from 0 - 10 Myr, with a plateau from 10 - 85 My of 75% to 78% (Figure 4.15). At older ages, the percentages decrease to a minimum of 45% in some migration models but typically range between 50% to 65%. In general, the 1-D models have the highest percentages for a given age.

Vote maps show thicker MTZs near high-velocity zones near the subduction zones (Figure 4.15), even if the depths and velocities are correlated only in some cases, with coefficients of 0.4 –

0.7 (Figure 4.17). MTZ thickness is mildly correlated with seismic velocity, with correlation coefficients of 0.4 - 0.7.

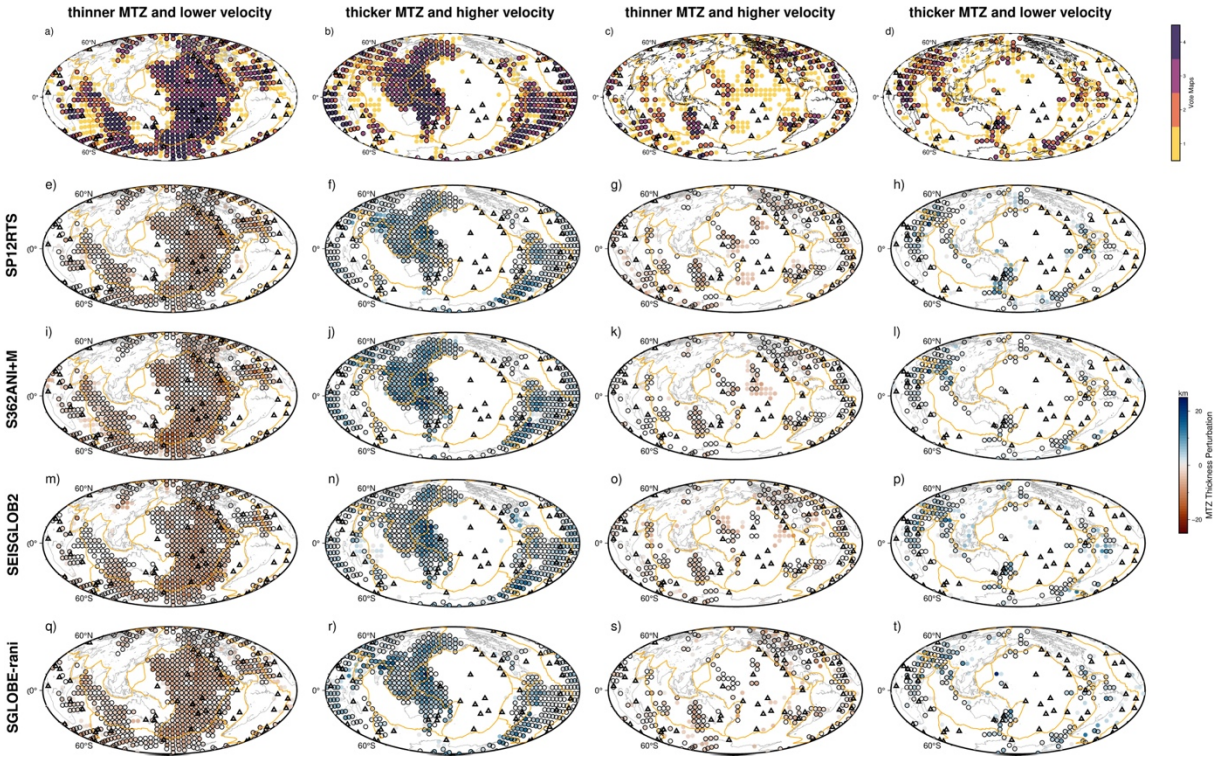

Figure 4.17 Patterns by MTZ thickness perturbations and velocity perturbations. a) vote maps of a thinner MTZ and low-velocity anomaly from 4 models with 3-D crustal and mantle corrections. b) vote maps of a thicker MTZ and high-velocity anomaly. c) vote maps of a thinner MTZ and high-velocity anomaly. d) vote maps of a thicker MTZ and low-velocity anomaly. e) - h), MTZ thickness perturbations to its average of patterns corresponding to a) - d) respectively from model SP12RTS. i) - l), from model S362ANI+M, m) - p), from model SEISGLOB2, q) - t), from SGLOBE-rani. Orange lines show plate boundaries (Bird, 2003), and black triangles indicate major hotspots (Courtillot et al., 2003).

4.4.3 The 660

The average depth of the 660 ranges from 657 ± 9 km - 654 ± 9 km using the 1-D reference models without and with crustal correction, respectively, and 654 ± 8 km (S362ANI+M) to 658 ± 8 km (SP12RTS) using the 3-D models (Figure 4.4). The ranges of the models are as follows: IASP91 636 - 686 km, IASP91 with a crustal correction 635 - 684 km, SP12RTS 643 - 690 km, S362+Ani 641 - 698 km, SEISGLOBE2 638 - 688 km and SGLOBE 647 - 704 km.

The 660 topography maps share a similar pattern with the MTZ thickness maps with correlation coefficients from 0.5 to 0.8 for the 3-D model migrations (Figure 4.7). The 660 depths are positively correlated with the 410, with coefficients of 0.5 to 0.8 using the 3-D migration models (Figure 4.9).

The 660 is uplifted to 650 - 647 km beneath the northwestern and middle Pacific, 658 – 648 km beneath the north Atlantic, and 660 – 648 km beneath the Indian Ocean (Figure 4.4). The 660 is not preferentially uplifted beneath hotspots, and the mean amount of uplift in the bins is between 1 and 3 km (Figure 4.10). However, beneath the Atlantic, 2/6 of migration models (3-D migration models) pass the t-test for a shallower 660 beneath the ridge in comparison to the remaining ocean basin, while beneath the Pacific Ocean, 1/6 of pass and beneath the Indian Ocean, 2/6 pass (Figure 4.18 – 4.20).

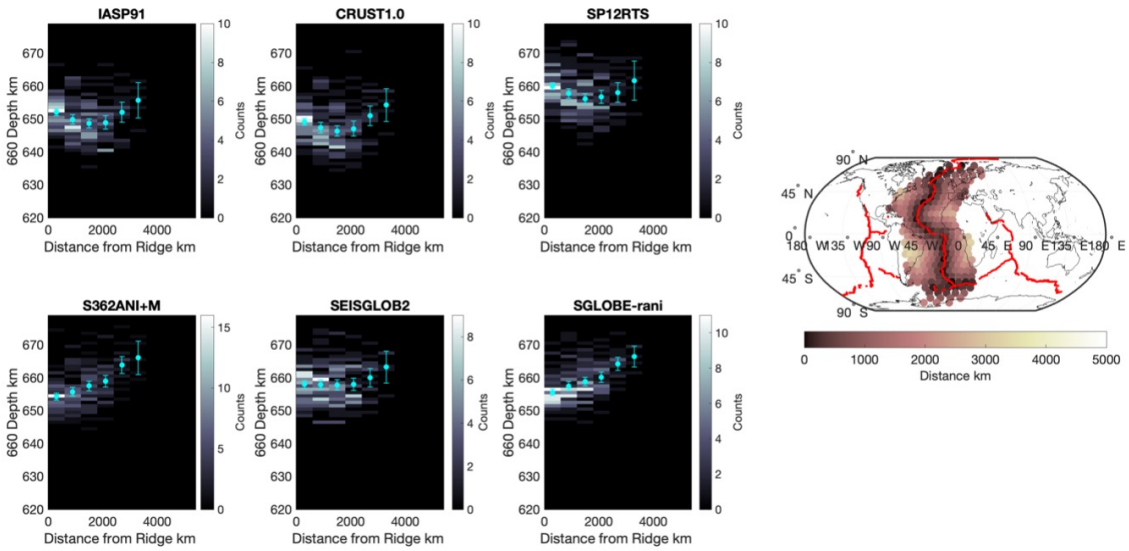

Figure 4.18 Histograms of 660 depth vs. distance from the Atlantic mid-ocean ridge for the different migration models. Migration model is indicated above each panel, cyan circles with error bars show the mean and standard error of the mean of each 600 km distance bin. Map on the right indicates the ridge location in red, and the bins coloured by distance to the ridge included in the histograms.

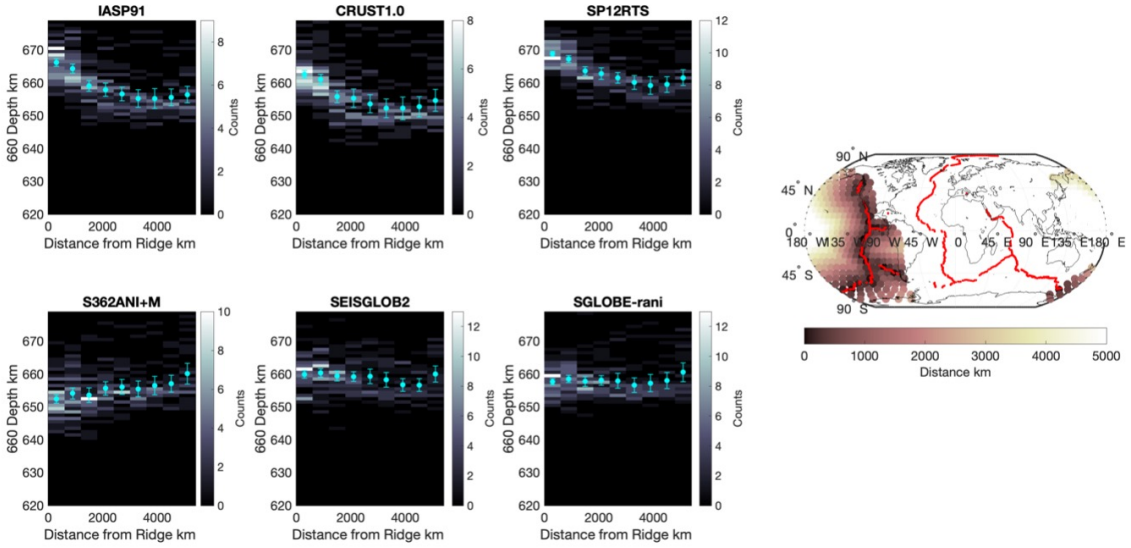

Figure 4.19 Histograms of 660 depth vs. distance from the Pacific mid-ocean ridge system for the different migration models. Migration model is indicated above each panel, cyan circles with error bars show the mean and standard error of the mean of each 600 km distance bin. Map on the right indicates the ridge location in red, and the bins coloured by distance to the ridge included in the histograms.

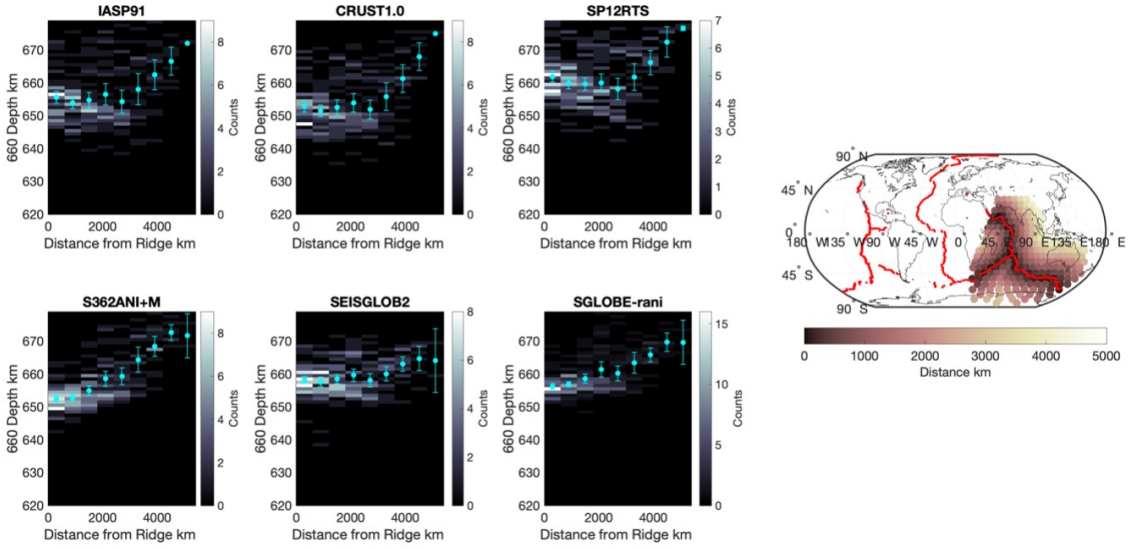

Figure 4.20 Histograms of 660 depth vs. distance from the Indian mid-ocean ridge system for the different migration models. Migration model is indicated above each panel, cyan circles with error bars show the mean and standard error of the mean of each 600 km distance bin. Map on the right indicates the ridge location in red, and the bins coloured by distance to the ridge included in the histograms.

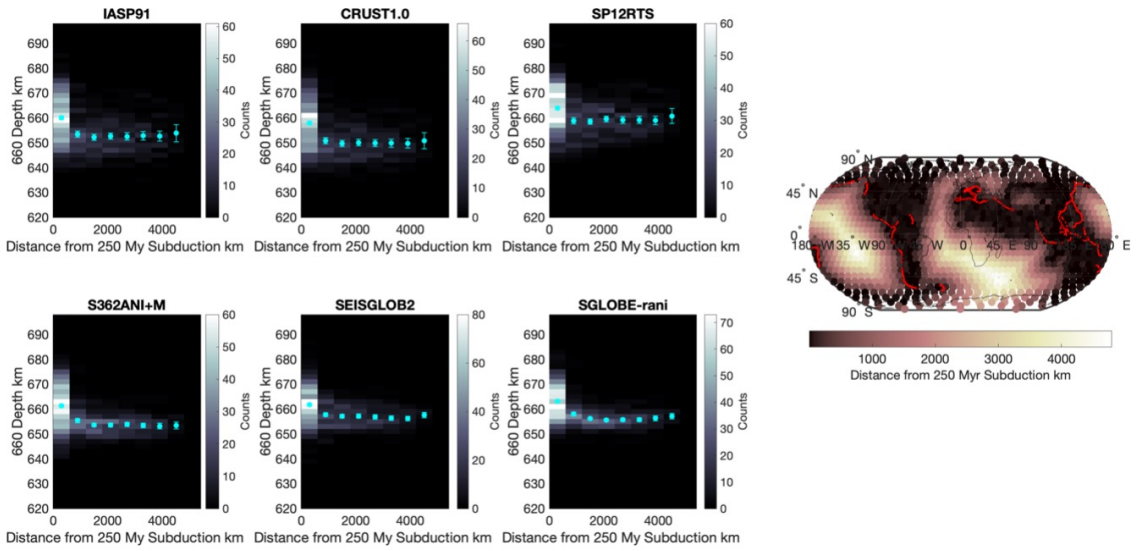

Figure 4.21 Histograms of 660 depth vs. distance from the paleo trench locations for the different migration models. Migration model is indicated above each panel, cyan circles with error bars show the mean and standard error of the mean of each 600 km distance bin. Map on the right indicates the current trench location in red, and the bins coloured by distance to the paleo trenches used in the histograms.

In all models, the 660 is depressed to 670 - 680 km beneath the subduction zones and their vicinities, this includes the subduction zones mentioned for the MTZ thickness and in addition, Cascadia (Figure 4.4). Most of the deep 660 bins are located beneath current or paleo trenches, as follows: IASP91 75%, IASP91 with crustal correction 76%, SP12RTS 68 %, S362ANI+M 84%, SEISGLOB2 72% and SGLOBE-rani 86% (Figure 4.21). The deep bins that are not located beneath the paleo trenches are again located east of South America and beneath western south Africa, with a few bins in central Europe and a few scattered bins in the Pacific. All migration models passed the t-test for the depression of the 660 comparing regions near current or paleo tranches to those at further distances.

There are locations beneath paleo trenches that do not have depressed 660. The number of deeper-than-average bins relative to the total number of deeper-than-average bins increases from 0 -10 Myr with a plateau of ~28 - 32% depending on the migration model from 10 - 70 Myr, and there is a relatively constant percentage from 19 - 25% depending on the migration model at > 70 Myr (Figure 4.22). The number of deeper-than-average bins relative to the total number of bins near current or paleo trench locations has a similar pattern. The percentages increase from 0 - 10 Myr, with a plateau from 10 - 85 Myr of 75% to 85%. At older ages, the percentages decrease to 53% - 74%. In general, SGLOBE-rani and S362ANI+M have the highest percentages, while SP12RTS has the lowest values.

Vote maps show deeper 660 near high-velocity zones near the subduction zones, even if the depths and velocities are not well correlated (Figure 4.15 – 4.17). The 660 is not very correlated with seismic velocity, with correlation coefficients of 0 - 0.5.

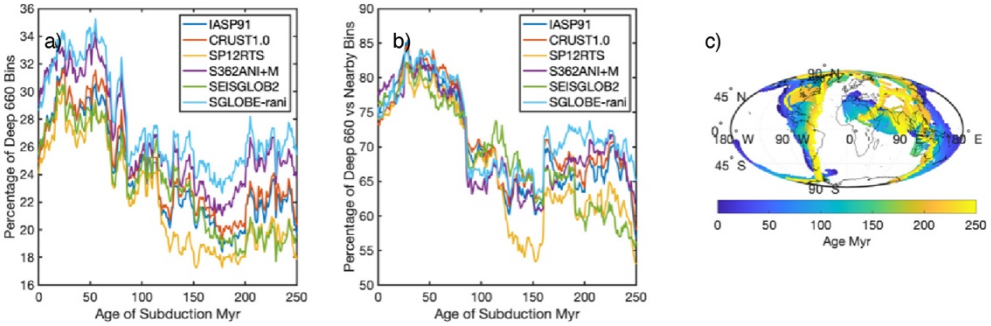

Figure 4.22 Percentages of thicker than average bins relative to the total thicker than average bins a) and relative to the bins nearby (<600 km) a paleo trench b) as a function of age of subduction (or paleo trench age). Coloured lines indicate the migration model used indicated in the legend. c) shows paleo trench locations as a function of age.

4.4.4 The 410

The average depth of the 410 from the 1-D models is 411 ± 7 km and 409 ± 7km without and with crustal corrections, shallower but within error of those from the 3-D models, which range from 416 ± 5 km for model SEISGLOB2 to 417 ± 6 km for model SP12RTS (Figure 4.4). The ranges of the models are as follows: IASP91 391 - 433 km, IASP91 with a crustal correction 388 - 434 km, SP12RTS 398 - 434 km, S362ANI+M 397 - 435 km, SEISGLOBE2 395 - 430 km and SGLOBE-rani 400 - 432 km.

The 410 is relatively depressed to 415 - 429 km beneath the northeast and the south of the Pacific, and regions outlining the subduction zones around the Pacific, and some regions beneath the Indian Ocean, close to the mid-ocean ridges. The 410 is not preferentially depressed beneath hotspots, and the mean amount of depression from the mean 410 depth in the bins nearest the hotspots is between 0 and 1 km (Figure 4.10).

Beneath the Atlantic and the Pacific, 4/6 of migration models pass the t-test, suggesting a deeper 410 beneath ridges in comparison to more distant oceanic regions. In comparison, beneath the Indian Ocean, only 1/6 of migration models pass (Figure 4.23 – 4.25).

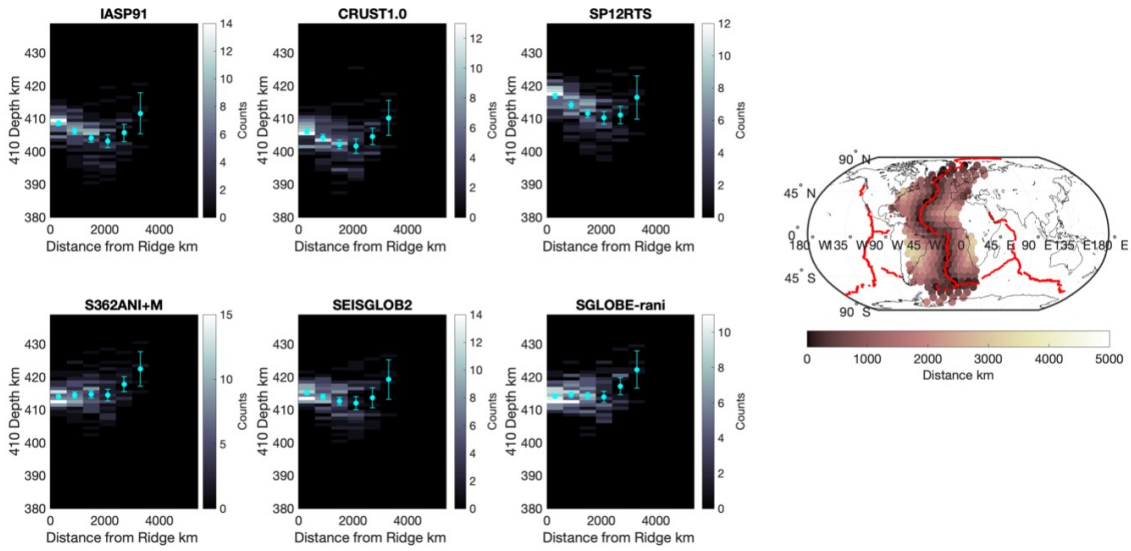

Figure 4.23 Histograms of 410 depth vs. distance from the Atlantic mid-ocean ridge system for the different migration models. Migration model is indicated above each panel, cyan circles with error bars show the mean and standard error of the mean of each 600 km distance bin. Map on the right indicates the ridge location in red, and the bins coloured by distance to the ridge included in the histograms.

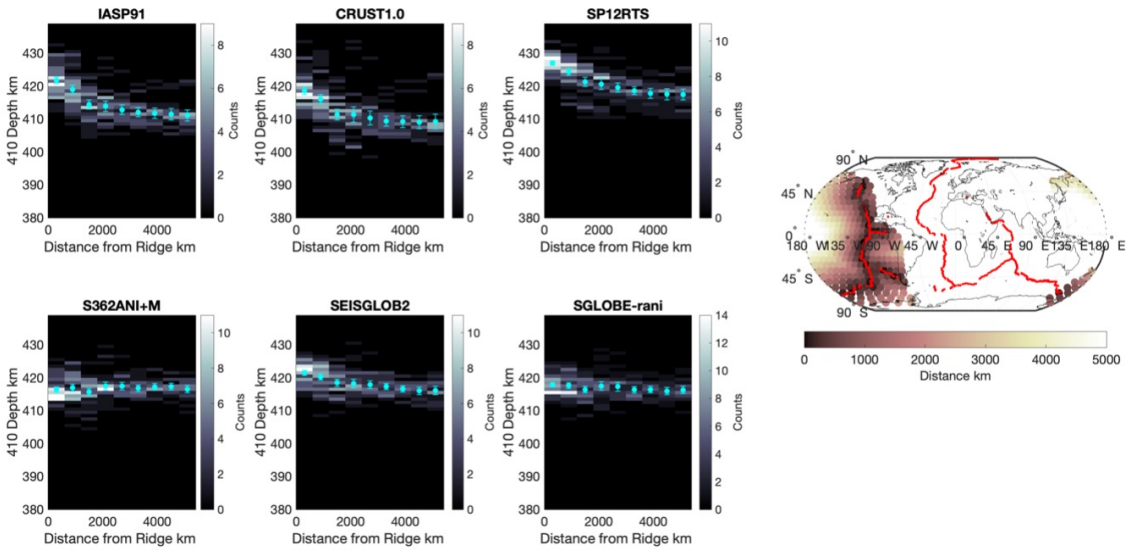

Figure 4.24 Histograms of 410 depth vs. distance from the Pacific mid-ocean ridge system for the different migration models. Migration model is indicated above each panel, cyan circles with error bars show the mean and standard error of the mean of each 600 km distance bin. Map on the right indicates the ridge location in red, and the bins coloured by distance to the ridge included in the histograms.

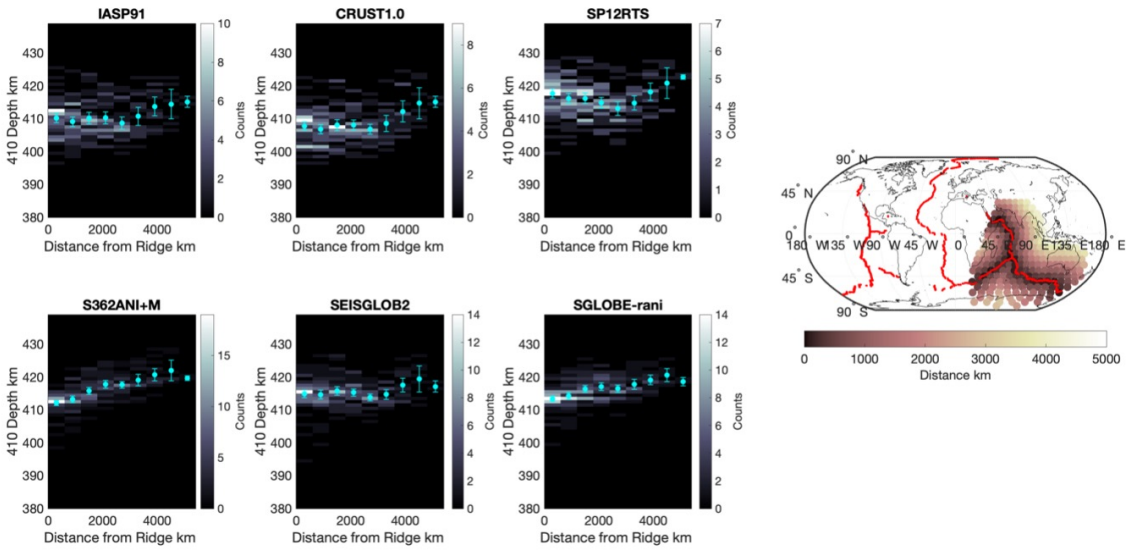

Figure 4.25 Histograms of 410 depth vs. distance from the Indian mid-ocean ridge system for the different migration models. Migration model is indicated above each panel, cyan circles with error bars show the mean and standard error of the mean of each 600 km distance bin. Map on the right indicates the ridge location in red, and the bins coloured by distance to the ridge included in the histograms.

The 410 is uplifted near high velocities in the northwestern Pacific and parts of North and South America. Vote maps don't show a strong relationship between 410 topography and seismic velocity related to expected locations of upwelling or downwelling and the correlation coefficient between the two is low, -0.3 - 0.2 (Figure 4.16, 4.17).

4.5 Discussion

Our average MTZ thickness from the 3-D models of 241 ± 6 km to 244 ± 5 km is thinner than 270 km from PREM (Su et al., 1994) and 250 km from IASP91 (Kennett & Engdahl, 1991), but agrees with previous studies from receiver functions, 242 km (Lawrence & Shearer, 2006), and SS precursors, 240 km (Houser et al., 2008) 242 km (Gu & Dziewonski, 2002) 241 km (Flanagan & Shearer, 1998) 244 ± 13 km (Huang et al., 2019). The average depths of the 660, 654 ± 8 km to 658 ± 8 km from the 3-D models, agree with those of previous SS precursor observations, for instance, 660 (Flanagan & Shearer, 1998), 661 km (Huang et al., 2019), and 660 (Houser et al., 2008). The average depth of the 410, 413 ± 5 km to 414 ± 6 km from the 3-D models agrees with previous SS observations of 418 (Flanagan & Shearer, 1998) and 416 ±7 km (Huang et al., 2019) and 410 km (Houser et al., 2008).

The features of MTZ thickness are in agreement with previous global studies either from receiver functions (Lawrence & Shearer, 2006) or from SS precursors (Flanagan & Shearer, 1998;

Houser et al., 2008; Huang et al., 2019). Aligning with typical assumptions, the MTZ is thinner than 250 km beneath oceans where hotspots concentrate and thicker than 250 km beneath active subductions such as Kurils, Philippines, Tonga, and South America.

Transition zone thickening is pervasive and strong, with thickening up to 267 km in some models visible in the circum-Pacific and across Eurasia in the Alpine orogeny region. The correlation between the 660 depths with MTZ thickness (0.54 – 0.80), the correlation between MTZ thickness and seismic velocity, the vote map agreement for high velocities and thicker MTZs and deeper 660s, and the t-test confirmation of thicker transition zone and deeper 660 near current and paleo trenches, suggest that the 660 and MTZ anomalies reflect a first order signature of thermal anomalies related to slab downwelling and stagnation.

In comparison, the lack of an anticorrelation correlation between the 410 and the MTZ (-0.22 - 0.00), the lack of an anti-correlation between seismic velocity and 410 depths, the lack of a vote map signature of high velocities and uplifted 410s near subduction zones, and the failure of the t-test for uplifted 410s near subduction zones in comparison to surrounding regions suggest that there is no strong signature of slab related to slab downwelling. Slab downwellings must still occur at depths of the 410, although they are either obscured by chemical signatures or they occur at a smaller scale than resolvable by our study.

The fact that the strongest MTZ anomaly signatures (267 km) and 660 anomalies are related to slabs and on very wide lateral scales of > 600 km to be detected here, suggests a fundamental constraint on material property transfer. The lateral scales of the thickening are much more pronounced than might be expected for a vertically descending ~100 km thick slab, extending over thousands of km. This is likely because of slab stagnation in the MTZ which results in large and coherent MTZ anomalies. Numerous other studies have observed stagnant slabs in the mantle transition zone based on tomography and measurements of mantle transition zone thickness (Goes et al., 2017; Lawrence & Shearer, 2008). Here, we find there may be a “residence time” for stagnant slabs. MTZ thickness anomalies are the largest beneath paleo trenches from 10 - 85 Myr age, suggesting that this is a common time period of slab stagnation before descending into the lower mantle. The presence of fewer anomalies beneath older paleo trenches suggests that slabs may still stagnate for 100 Myr. In addition, there were substantial amounts of thickened MTZ away from the paleo trenches, particularly beneath southern Africa. These thickened regions may be areas of even older subduction prior to the breakup of Pangea or possibly regions of foundered continental lithosphere or downwelling caused by the continental lithospheric keels (Blum & Shen, 2004).

The lack of an upwelling signature beneath hotspots in the 410, 660, or MTZ anomalies could be related to greater compositional complexity, although it could also be the case that the upwellings occur at a smaller resolution than our bin diameters, or that some or all of the upwellings do not

originate from the lower mantle or have a strong signature due to thermo-chemical effects. Many images of hotspots from Hawaii (Agius et al., 2017) or Iceland (Jenkins et al., 2016; Shen et al., 1998) using higher resolution P-to-S receiver function imaging typically identify thinned plume anomalies on length scales of 300-500 km, which is less than our bin spacing. In the case of Hawaii, the thickening of the MTZ was also observed adjacent to the thinning of the MTZ, which, if common may effectively cancel out apparent thinning (Agius et al., 2017). Finally, some plumes may not have a thoroughgoing transition zone signature, as was used in the classification of Courtillot et al. (2003) and suggested from mantle tomography (Montelli et al., 2006) . However, our analysis did not find systematic transition zone signatures for the most robust plumes in the Courtillot et al. (2003) model. Alternatively, a physical process such as an increased amount of garnet and high temperatures in the plumes could mute the thinning of the transition zone at the 660 in some cases (Jenkins et al., 2016).

The other pronounced anomaly pattern comes from ridges, in particular, beneath the Atlantic. The MTZ shows the strongest evidence of upwelling, where all migration models pass the t-test, whereas evidence in the Pacific and the Indian Ocean is less strong with 3/6 and 2/6 of models passing, respectively. There is a general correlation between MTZ thickness and seismic velocity (0.42 – 0.66), although the velocity/thickness vote maps show agreement beneath oceans, without necessarily showing a strengthened signature beneath ridges. This supports the general notion of upwelling beneath the oceans, and particularly the Mid-Atlantic Ridge. One possible explanation for the preferential signature beneath the Mid-Atlantic Ridge in comparison to other ridges could be that the ridge has remained in the same position and has been relatively stable over the past 50-100 Myr period (Müller et al., 2019) in comparison to the other basins which have seen significant migration and reorganisation of the ridge systems. MTZ upwelling beneath the Mid-Atlantic Ridge is contrary to the classic paradigm in which ridge upwellings occur over only the shallowest sub-ridge mantle depths. However, the observation is consistent with previous P-to-S receiver function studies beneath the Mid-Atlantic Ridge and Cascadia (Agius et al., 2021; Dai et al., 2023), global SS-precursor studies that found thinning beneath the ridges in Cascadia (e.g., Huang et al., 2019; Waszek et al., 2021), and slow sub-ridge MTZ velocities in several global tomography models (e.g., Montelli et al., 2006; Montelli et al., 2004).

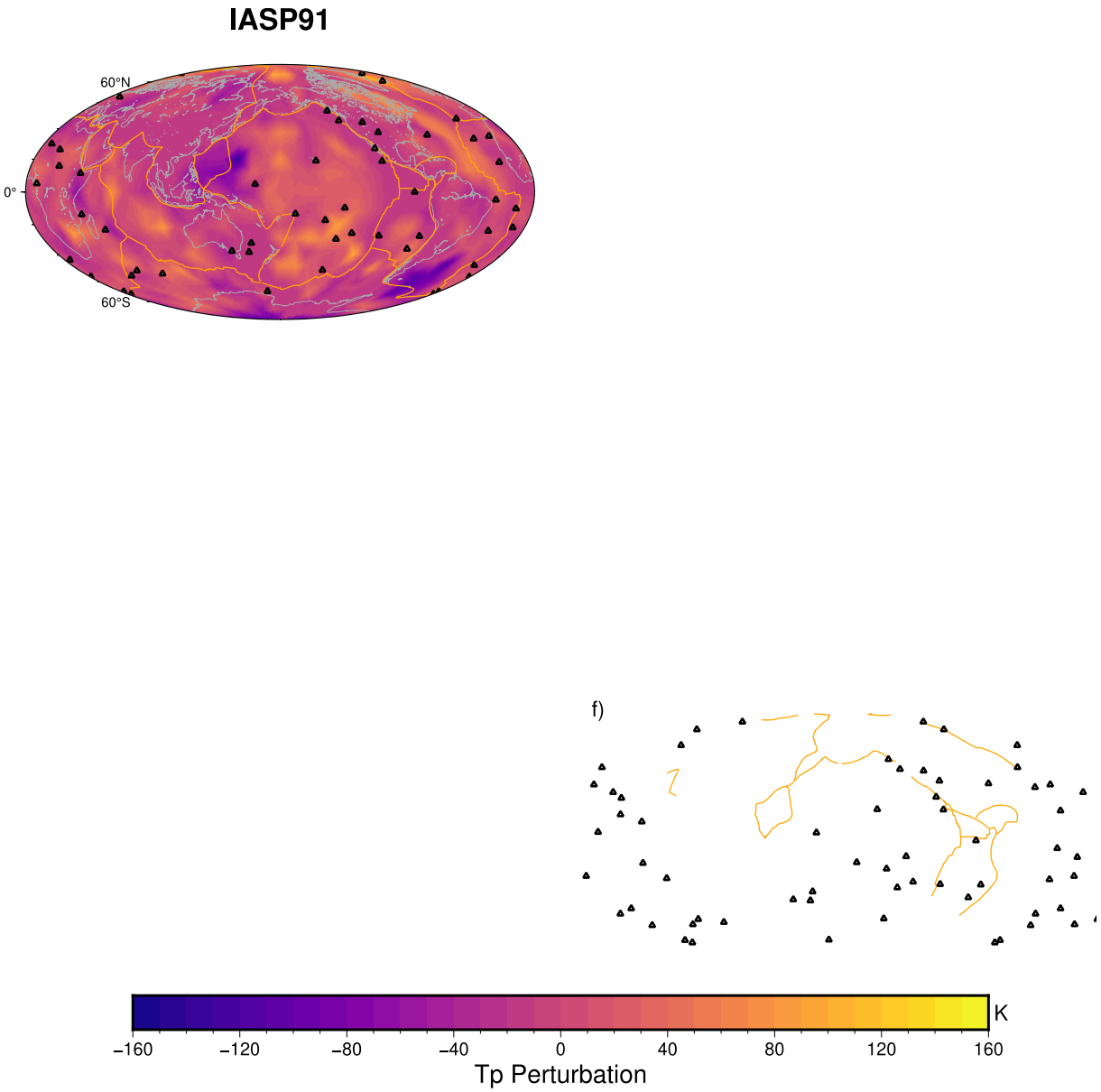

Figure 4.26 Temperature anomaly maps. Potential temperature (Tp) anomalies inverted from MTZ topographies via looking up predictions from thermodynamic modelling. a) – b) Tp perturbation maps from MTZ topographies from migration using only 1-D reference model IASP91, crustal corrections with CRUST1.0 only, and models with crustal corrections using CRUST1.0 and upper mantle corrections using SP12RTS, S362ANI+M, SEISGLOB2, SGLOBE-rani, respectively.

The thermal perturbations, based on the MTZ topographies found here and temperature and discontinuity depths relationships predicted by thermodynamic modelling (e.g., Waszek et al., 2021), show a range from ± 160 K (Figure 4.26). The coldest regions are found east of South America and west of southern Africa, with the other coldest regions found beneath the trenches in most of the migration models. The Pacific Ocean basin appears as a moderately warm region, typically with > 60 K perturbation, while the other ocean basins have both hotter and colder anomalies. The Mid-Atlantic Ridge has thermal anomalies along much of its axis of up to ~80 K in the northern Atlantic in

most of the migration models. The temperature structure we find here is more muted compared to some other SS precursor work, for example, Lawrence and Shearer (2008) estimated up to ± 300 K using ranges of Clapeyron slopes from several studies (Fei et al., 2004; Katsura et al., 2004; Katsura et al., 2003; Litasov et al., 2005; Morishima et al., 1994). Our temperatures are more similar to those of Waszek et al. (2021), which had ranges of –200 K to 175 K, where a mixed mantle composition is predicted by thermodynamic modelling.

Previous work has attempted to infer the amount of hydration and its global distribution based on seismic observations (Chang et al., 2015; Houser, 2016; Mao & Zhong, 2018; Meier et al., 2009; Wang et al., 2021). However, the results of these investigations are highly variable. The depths of the 410 and the 660 with shear velocities have been used to infer very little evidence for hydration (8 % of bins with an average of 0.6 wt.%) (Houser, 2016) and also much more pervasive hydration, for instance, in all regions away from subduction zones (Meier et al., 2009) or primarily in subduction regions and at high percentages (0.5 - 1 wt% and 0.2 - 0.5 wt%, at the top and the bottom of the MTZ, respectively (Wang & Wang, 2022). These discrepancies likely arise from uncertainties in the mineral physics relationships and the seismic observations. We note that the velocity anomalies around the 410 and the 660 are nearly identical (Figure 4.3 – 4.5), correlated at 0.47 - 0.84, despite the fact that our interpreted upwellings/downwellings at the two discontinuities are substantially different. Therefore, this is not a goal of this study. In addition, previous studies have considered the MTZ discontinuity depths and amplitudes of the reflected phases, considering SS (and PP) precursors, to infer the basalt content (e.g., Waszek et al., 2021; Yu et al., 2023). However, we have not analysed PP precursors and the waveform processing performed here, including deconvolutions, increases our uncertainty in amplitudes. Finally, some have analysed negative phases preceding the 410 to infer the locations and properties of a supra-410 melt layer. However, again, we have less certainty in the robustness of these phases since the deconvolutions performed in preprocessing can result in artificial sidelobes.

4.6 Conclusion

We use a new deconvolution approach to image the global MTZ discontinuities using SS precursors with a dataset consisting of the last 3 decades' records. The massive dataset provides an excellent global data coverage, and the implemented method provides higher resolution imaging. We obtain the depths of the MTZ discontinuities and thicknesses with different migration models that correct the effects of heterogeneity of the crust and the upper mantle. We interpret the robust features of the MTZ regardless of migration assumptions.

The features of MTZ thickness are in agreement with previous global studies either from receiver functions (Lawrence & Shearer, 2006) or from SS precursors (Flanagan & Shearer, 1998;

Houser et al., 2008; Huang et al., 2019) as well. Aligning with typical assumptions, the MTZ is thinner than 250 km beneath oceans where hotspots concentrate and thicker than 250 km beneath active subductions such as Kurils, Philippines, Tonga, and South America.

The 660 topography variations are generally correlated with MTZ thicknesses, reflecting the locations of upwellings and downwellings at a large scale as well as locations where cold materials accumulate in the bottom of the MTZ. The lack of anticorrelations between the 410 and the 660 topography requires more complexity than the simple assumption of vertical/sub-vertical transport of materials. The subducted cold materials may be stagnant at the 660 but affect the 410 at a lateral scale and/or magnitude that is smaller than resolvable by our study. The 660 may play a larger role in dictating downward material transfer through the MTZ.

Overall, our observations suggest a greater complexity of materials transport across the MTZ than the typical paradigm of the simple vertical ascent of material through the MTZ (Morgan 1971). Large volumes of cold materials descend into the lower mantle from the upper mantle beneath the subduction zones or into the mantle transition zone and stall at the bottom. Deep upwellings from the lower mantle may occur beneath tectonic locations other than hotspots, including beneath ridges. Such prevalent upwellings play a role in counterbalancing the slab downwellings.

Chapter 5 Conclusions

5.1 Summary of Observations

To advance our understanding of mantle transition zone (MTZ), regional seismic observation with a particular focus on the Cascadia region and global investigation of the MTZ discontinuities were conducted. High-resolution imaging using extended-time multi-taper Ps receiver functions (RFs) for regional data was applied. A novel SS precursor imaging method for global-scale analysis was developed and validated. Finally, the new SS precursor method was applied to global data sets.

In the first part of our study, the Cascadia region, located along the Pacific Northwest coast of North America, geologically significant due to the presence of subducting slabs, volcanic activity, and the Juan de Fuca and Gorda Ridges, is seismically imaged. An amphibious dataset, combining both onshore and offshore seismic stations was used to achieve detailed imaging of the MTZ. The analysis focused on seismic phases that exceeded the formal error bars of the stack, avoiding the far edges of the model and concentrating on depths that were unaffected by crustal reverberation artefacts.

While the assumptions in migration models can influence the absolute depths of the imaged discontinuities, the presence of MTZ phases and the observed trends in MTZ discontinuity depths and thicknesses are robust across a range of migration models. The receiver functions revealed that the MTZ is thinned beneath the Juan de Fuca and Gorda Ridges, as well as beneath the Cascadia Slabs, corresponding to regions where the 660-km discontinuity is uplifted. Additionally, a significant depression of the 410-km discontinuity beneath the northern Juan de Fuca plate and the Gorda plate has been observed, which is offset from the uplifted 660-km discontinuity. This lack of anticorrelation between the 410 and 660 depths challenges classical models of vertically ascending or descending mantle flows. This could be caused by more complex mantle flow and/or compositional effects that obscure vertical flows. However, the variations in topography at both the 410 and 660 discontinuities are consistent with thermal predictions based on previous seismic tomography studies. Therefore, temperature is the most straightforward explanation, and therefore complexity than the classical model of uniform vertical upwellings and downwellings is implied.

Secondly, a novel SS precursor imaging method using deconvolution, which enables high-resolution imaging of Earth's internal discontinuities from as shallow as 20 km in depth to the MTZ was developed. This method achieves a grid resolution in 6-degree circular bins. To verify the effectiveness of this method, we applied it to AxiSEM synthetics calculated for a PREM model modified to include velocity increases at potential Moho depths ranging from 10 to 60 km. This showed that the method can resolve Moho depths as shallow as 20 km. In addition, we compared

the resolved Moho depths from the 6-degree bins to those from the CRUST1.0 model. The models were correlated at 77% beneath all continental regions, with the exceptions mainly located in coastal areas where complexities in crustal structure may affect the imaging results. Both synthetic and real data examples confirmed that the method is also effective in resolving MTZ discontinuities, further supporting its potential for future high-resolution imaging of subsurface structures. This technique opens up new possibilities for imaging other discontinuities within the Earth's mantle and crust, offering a more detailed understanding of mantle processes.

Finally, the new SS precursor imaging approach was applied to a global data set consisting of records from over 9165 broadband seismic stations. The global MTZ topographies were imaged at high resolution. The depths of the MTZ discontinuities and the thickness of the MTZ were obtained including a crustal correction. Migration tests using different mantle velocity models were performed, and robust features were interpreted.

In a global view, the MTZ thicknesses align with the classical assumption that the MTZ is thin in hot regions and thick in cold regions. The MTZ beneath the Pacific is thinned where upwellings are expected since numerous hotspots are located there. Around the Pacific, beneath the subduction zones, the MTZ is found to be thickened where the descending of cold slabs from the upper mantle to the lower mantle occurs. Focused thinning beneath individual hotspots is not resolved. Away from the locations where upwellings are conventionally expected, focused thinning of the MTZ is observed beneath the Mid-Atlantic Ridge in comparison to adjacent regions, i.e., beneath the older Atlantic lithosphere, suggesting upwelling.

The 660 topography perturbations are better correlated with MTZ thicknesses. More complex dynamics than vertical upwellings beneath hotspots and downwellings beneath subduction zones are implied. Overall agreement between MTZ thickness and velocity in the vote count maps suggests that rather than strong chemical heterogeneity, temperature dominates the signals, but material transport is more complex. For instance, beneath subduction zones the slab may descend directly through the 410, with an anomaly that is not laterally large enough for detection by SS precursors, whereas slabs are likely impeded and accumulated near the 660. Beneath the oceans, MTZ thinning suggests that large scale material upwelling likely occurs. The lack of focused thinning beneath hotspots could be again related to resolution and/or more complex pathways and/or scales of ascent. Finally, pronounced thinning beneath the Mid-Atlantic Ridge suggests that upwelling from the lower mantle occurs there. Mixed evidence for thinning beneath other ridges could be explained by the higher rates of mobility of the Pacific and Indian Ridges in comparison to the Atlantic.

In conclusion, receiver functions and SS precursors effectively image the MTZ discontinuities, albeit at different scales of resolution and with different global coverage. The nature of the formation of materials transport downwellings is more complicated than the simple vertical

ascending shown by the classic paradigm (Morgan, 1971). Large volumes of cold materials descend into the lower mantle beneath the subduction zones and stall at the bottom. Ascension of hot materials from the lower mantle occurs beneath oceans, with enhanced upwelling ridges, at least and particularly beneath the Atlantic. Material ascent beneath ridges may play a role in counterbalancing slab downwelling.

5.2 Future Work

Precise constraints on the global mantle transition zone are essential for understanding the role of the mantle transition zone, thus the mantle convection and the evolution of the Earth. As demonstrated before, SS precursor imaging can achieve excellent global data coverage, and the newly implemented approach provides higher resolution. However, due to the fact that SS precursors are of long period, the lateral resolution is of the degree of ~ 1000 km. In contrast, receiver functions imaging can provide a finer lateral resolution, on the scale of ~ 150 km, as demonstrated in the Cascadia study. In addition, despite the wide variety of tectonic regimes in Cascadia, it only represents a small fraction of the tectonic environments on this planet. Therefore, the next practical approach is to apply receiver functions to the global data set to put tight constraints on the MTZ globally. The in-situ observations would enable a more comprehensive mapping of small-scale variations, particularly in regions with complex tectonics, such as beneath continental shields, hotspots, convergent margins, etc.

Besides the MTZ topographies, more prosperities could be revealed by seismic imaging of high resolution combining the SS precursors and receiver functions. For instance, compositional heterogeneity in the MTZ has been proposed. More accumulation of basalt at the bottom of the MTZ than its upper part in the global average is inferred by SS precursors amplitude analysis (Yu et al., 2023). Therefore, I will perform additional consideration of the geographical distributions of the compositional anomalies. Hydration of the MTZ is also controversial, however, it is crucial for understanding the dynamic of the mantle. A sporicidal low-velocity layer atop MTZ has been reported beneath the Pacific and other locations (e.g., Tauzin et al., 2010; Wei & Shearer, 2017). A more systematic investigation of the low velocity atop and/or immediately beneath the MTZ could be done by combining global receiver functions and the new SS precursor image approach.

The SS precursors and receiver functions are expected to produce consistent long-wavelength features of the mantle discontinuities, revealing the general mantle dynamics. Given the different sizes of the Fresnel zone, discrepancies are also expected for analysing the local variations of structure, composition, temperature, hydration, etc, inferring small-scale dynamic processes.

Both receiver functions and the newly developed SS precursor deconvolution approaches are able to resolve sharp discontinuities with high resolution in theory. In practice, suppressing noise and stacking coherent signals are important for obtaining high-resolution imaging. With the enormous volume of the global data set, machine learning and artificial intelligence (AI) techniques should also be considered. Future research could apply machine learning models to pick coherent phases automatedly. This could help process large volumes of seismic data more efficiently, improve the resolution, and potentially reveal subtle features that may be overlooked by traditional methods.

Overall, this will lead to a more comprehensive knowledge of the mantle dynamics and the evolution of the Earth.

Appendix A Support Information: Seismic imaging beneath Cascadia shows shallow mantle flow patterns guide lower mantle upwellings

We show examples of RFs from on- and offshore data (Figure A.1). We compare the on- and offshore datasets and melded them together (Figure A.2). We use different methods to testify the supra-410 phases (Figure A.3). We show hit counts maps (Figure A.4) and error maps (Figure A.5). Several seismic tomography results (Figure A.6) suggest upwellings from the lower mantle beneath the study area. We show vertical cross-sections from different migration models (Figure A.7).

A.1 Oceanic and land data

Variation in the character of the receiver functions between ocean and land stations is expected at shallow, crustal depths (Figure 2.4) given the very different crustal structures of the two. To demonstrate an example of the expected differences we constructed a synthetic receiver function from an oceanic model and one from a continental model (Figure A.2a). For the oceanic model, we assumed a 1 km sediment layer above a thin (6 km) oceanic crystalline crust under 3 km of water, and an underlying model taken from PREM (Dziewonski & Anderson, 1981). For the land model, we assumed PREM. We applied the same corrections to the synthetics that we applied to the data.

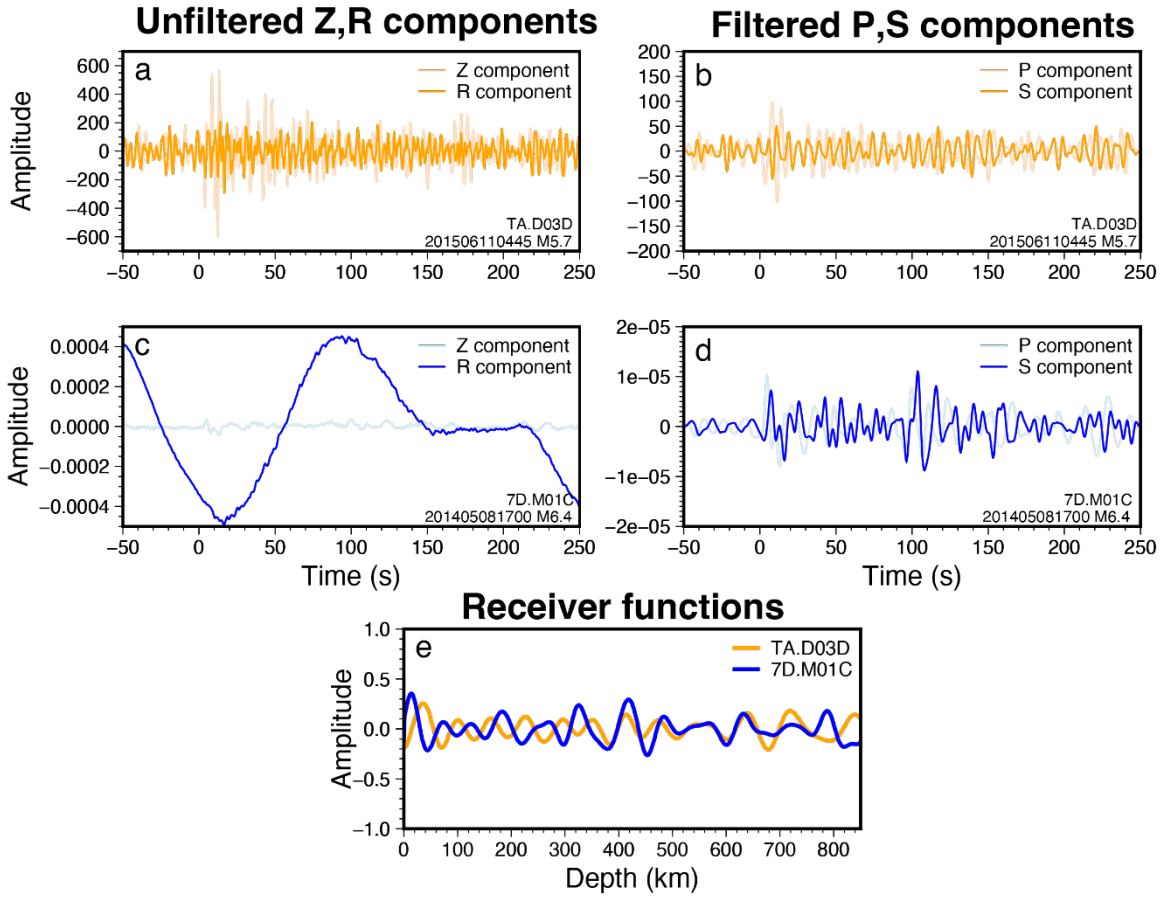

Figure A.1 Examples of RFs from on- and off-shore data. a. unfiltered Z and R components of a M5.7 earthquake recorded by the onshore station D03D. b. filtered P and S components using a bandpass of 0.05 – 0.2 Hz correspond to a. c. unfiltered Z and R components of an M6.4 earthquake recorded by the offshore station M01C. d. filtered P and S components using a bandpass of 0.05 – 0.2 Hz correspond to c. e. Receiver functions correspond to b and d. The piercing points of these two receiver functions are both within the bin centred at 47.5° N, 126° W showed in Figure 2.2.

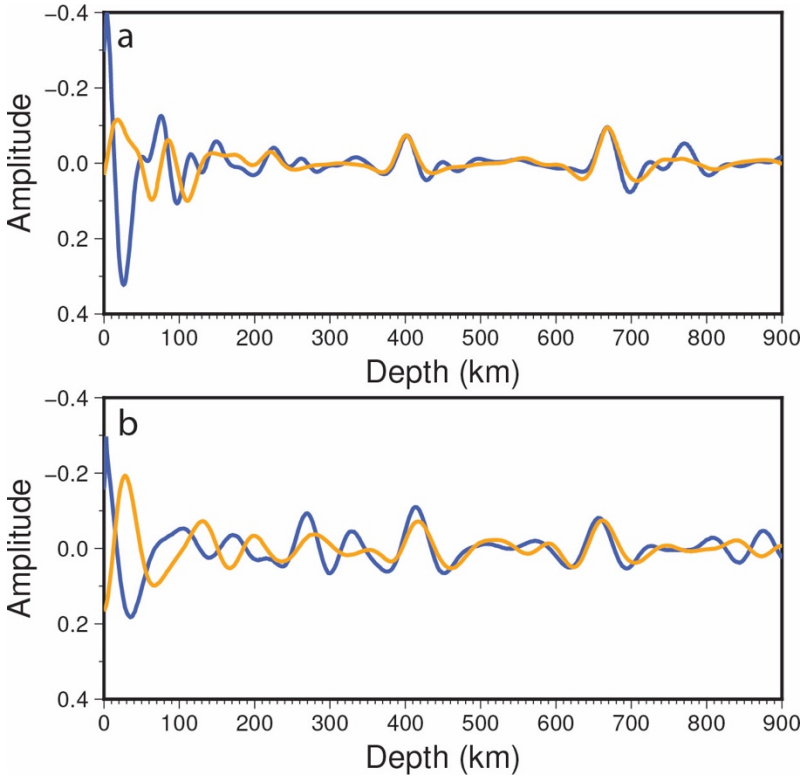

Figure A.2 Onshore and offshore RFs comparations. a. Synthetic RFs. Orange line: RF from a synthetic land model using the parameters of crust and mantle from the reference earth model PREM (without a water layer), which has a crustal thickness of 21.4 km (Dziewonski & Anderson, 1981). Blue line: RF from a synthetic ocean model. The crust is set to be 6 km thick with Vp: 5.9 km/s and Vs: 3.4 km/s. The mantle is taken from the land model while adding a sediment layer with thickness: 1 km, Vp: 1.65 km/s, Vs: 1 km/s, Q_κ: 163.35, Q_μ: 80, and a water layer with thickness: 3 km, Vp: 1.45 km/s, Vs: 0 km/s, Q_κ: 57823, Q_μ: 0. b. Real RFs. Orange line: average RF from offshore data with piercing points at 410 km and 660 km within the bin shown in Figure 2.2 c, d. Blue line: average RF from OBS data with piercing points at 410 km and 660 km within the bin shown in Figure 2.2 c, d.

We find substantial differences at shallow depths between the ocean and land receiver function examples (Figure A.1, A.2). In particular, the most prominent phase in the continental receiver function is the red (positive) phase associated with the continental Moho near 20 km depth. Whereas, there is a large blue (negative) phase at nearby depths beneath the oceans, which is caused by interference between P-to-S conversions from the sediment and crustal layers and associated reverberations (Rychert et al., 2013). These differences are similar to those observed in the data (Figure 2.4). Although we provide a single example for demonstration, the exact details of these differences are expected to be variable owing to factors such as differences in shallow structure (e.g., depth variations of the sediment, Moho, and lithosphere-asthenosphere boundary (Rychert et al., 2018a) and interference of reverberated phases. Given that reverberated phases are not properly accounted for in our migration approach, matching these characteristics is beyond the

scope of this work, we are not performing waveform modelling, and we do not have any strong interpretation of phases shallower than 250 km depth.

The synthetic test demonstrates the robustness of the transition zone discontinuities. The depths of the transition zone discontinuities remain the same regardless of this shallow variability (Figure A.2 a). In addition, supra-410 phases do not artificially appear in the ocean synthetic receiver functions. Also, reverberated phases from shallow discontinuities have completely died off by transition zone depths (Agius et al., 2021). Some small phases just after the 410 and 660 discontinuities appear in the ocean synthetic receiver functions, but not the land receiver functions. We have seen similar phenomena in some of our previous modelling work that includes sediment (Rychert et al., 2013). However, we do not model these phases given that we are not interpreting those depths, and the phases don't impact the 410 or the 660 depths. We also note that although the ocean and land data have different corrections applied to them, given the theoretical difference in the positions of the seismometers beneath air vs. water and the physical differences in the underlying Earth properties. The corrections are an effective way of merging the two datasets.

We also compare receiver functions made by land vs. ocean data in a single bin (Figure A.3 b). We find different characters between ocean vs. land data at shallow depths (< 30 km), similar to those found in the synthetic data. Similarly, variable reverberation effects contaminate the shallow 200 – 300 km. It is not our intention to model this exactly given the many potential complications. However, regardless of the differences in the shallow structure and corrections applied to account for this structure, the depths of the discontinuities are the same for the synthetic test and within our error bars for the data. This indicates that our theoretical corrections and variations in reverberations are not affecting our transition zone results.

A.2 Supra-410 phase

We applied an iterative time-domain deconvolution (Ligorria & Ammon, 1999) to test the robustness of the supra-410 phases Time-domain deconvolution does not suffer from sidelobes and therefore is an effective means of testing whether the supra-410 phases are sidelobe artefacts or actual conversions from the top of a supra-410 melt layer. We examined the data with theoretical piercing points in the two bins at 410 km depth with the strongest supra-410 phases (Figure 2.4 a, c,2.5 a). We filtered the waveforms between 0.05 and 0.2 Hz and used a Gaussian width factor of 3.5 for deconvolution. The stability of the time-domain deconvolution is different from the frequency-domain deconvolution. Therefore, we needed to remove 7 and 16 time-domain RFs without clear Moho phases or just pure spikes from the two bins, respectively. We then migrated the 22 and 39 remaining waveforms to depth using sediment and crustal corrections and the IASP91 model, as done for the frequency domain RFs. We then stacked the RFs to construct the RFs for waveforms

corresponding to the two bins characterized by large supra-410 phases (Figure A.3 c, d). We stacked the waveforms in the bins in the original model from the multi-taper deconvolution for comparison (Figure A.3 a, b). We scaled the time-domain RFs to have the same amplitudes for P410s phases as frequency-domain RFs.

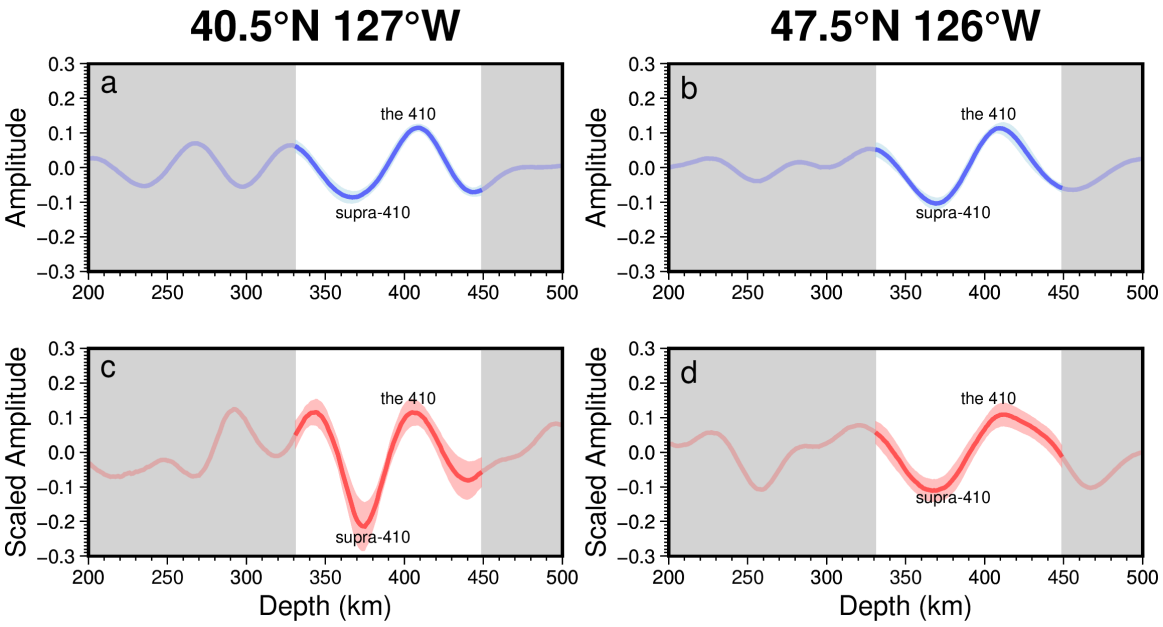

Figure A.3 Stacked RFs using different deconvolution methods. a. Stacked RFs in the bin centred at 40.5°N, 127°W (Figure 2.5 a). The blue line shows the stacked result of RFs calculated using the multitaper frequency domain deconvolution technique (Helffrich, 2006), and light blue shows the standard deviation. Shaded areas show depths that are not interpretable, as they sample different Earth structures. b. same as a but for the bin centred at 47.5° N, 126° W. c. Red line shows the stacked RFs that pierce a bin centred at 40.5° N, 127° W at 410 km depth using iterative deconvolution in the time domain (Ligorria & Ammon, 1999), with the pink region showing error bars. d. Same as c but for the RFs that pierce a bin centred at 47.5° N, 126° W at 410 km depth.

The resulting stacked receiver functions are more complex than the 3-D model in that there are also other phases besides the 410, 660, and supra-410 phases. In addition, there are some differences between the methods. This is expected for two reasons: 1) These stacks were made with receiver functions that contribute to the supra-410 stacks in the 3-D model, but these RFs also sample a variety of different structures laterally at other depths. 2) The methods have different stabilities, which meant fewer waveforms were useable in the time domain stacks. Overall, the weighting and 3-D stacking that contribute to the stability and consistency of the 3-D model cannot be achieved using this small number of waveforms sampling different geographical areas at depths above and below the supra-410 phase. Therefore, we have no interpretation of phases at depths other than the 365 - 375 km depth range in these stacks. However, the test demonstrates that the

supra-410 phase persists regardless of method, and in particular the phase persists in the time-domain method stacks, which are not susceptible to sidelobe artefacts.

We also note that the supra-410 phases are not artefacts of sediment deposited beneath the ocean near western North America. This is because the data in the supra-410 phase bins does not come from stations directly above, i.e., near the continental margin. Instead, the data in the supra-410 bins is primarily recorded at land stations further to the east.

In the end, we discuss the supra-410 phases given that their locations occur where we interpret upwelling based on the 410 topography, although these phases are not required for our interpretation of material transfer through the MTZ.

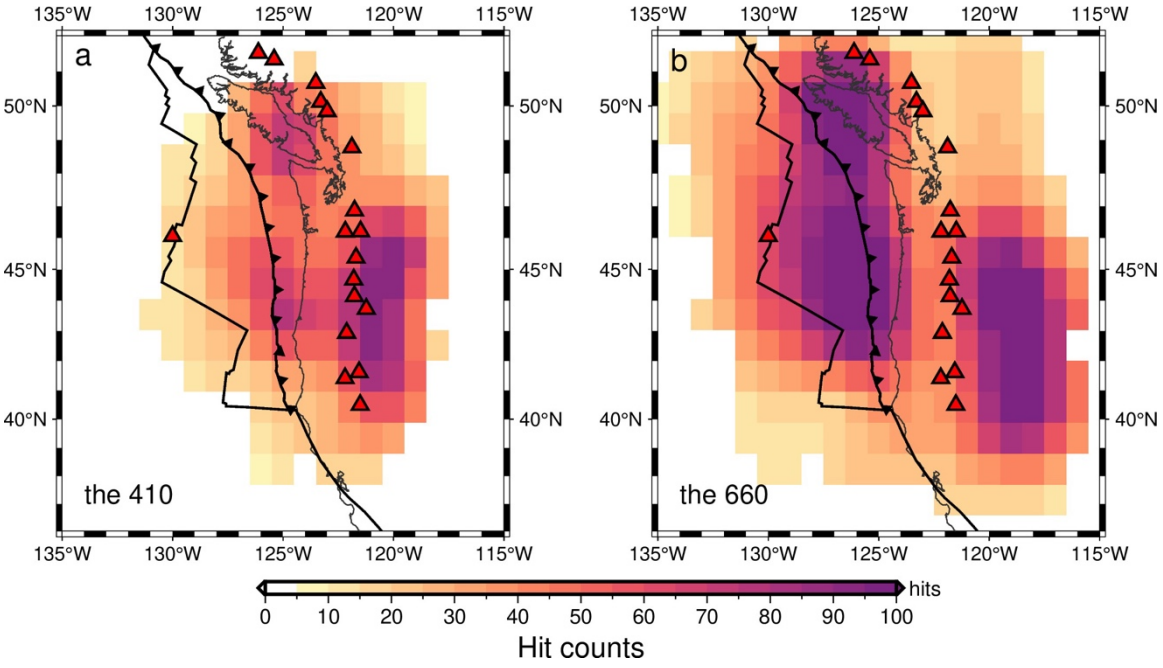

Figure A.4 Hit counts maps at 410 and 660 km depths. Maps show numbers of waveforms stacked at 410 and 660 km.

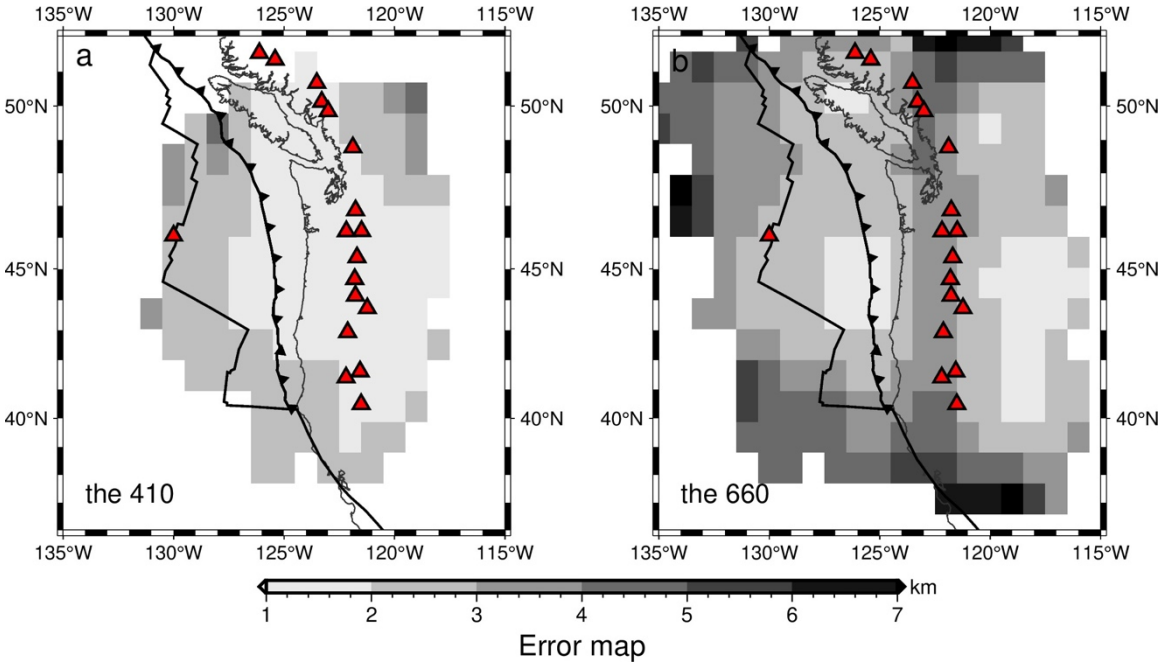

Figure A.5 Error maps of the 410 and 660 depths. Maps show standard errors of means of the 410 and the 660 depths.

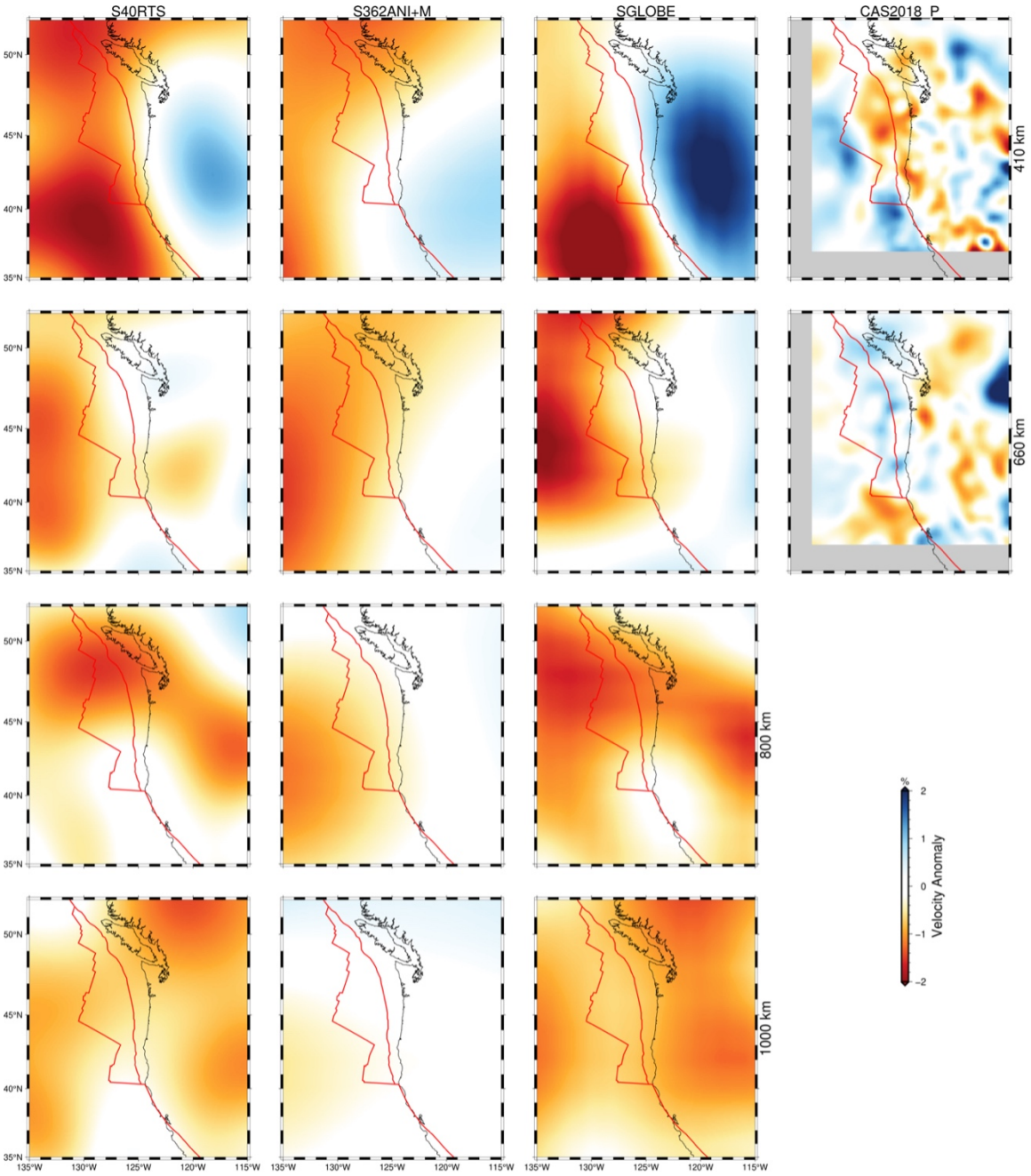

Figure A.6 Horizontal slices of tomography models. Left 3 columns: Horizontal slices of global tomography models S40RTS (Ritsema et al., 2011), S362ANI+M (Moulik & Ekström, 2014), and SGLOBE-rani (Chang et al., 2015) that share the same normal mode and overtone data combined with different types and combinations of surface wave and body wave data and tomography methods to resolve the mantle velocities at 410 km, 660 km, 800 km, and 1000 km. Right column: horizontal slices of regional P-wave velocity anomalies model CAS2018_P (Bodmer et al., 2018) at 410 km and 660 km. The grey areas show the region outside the mode.

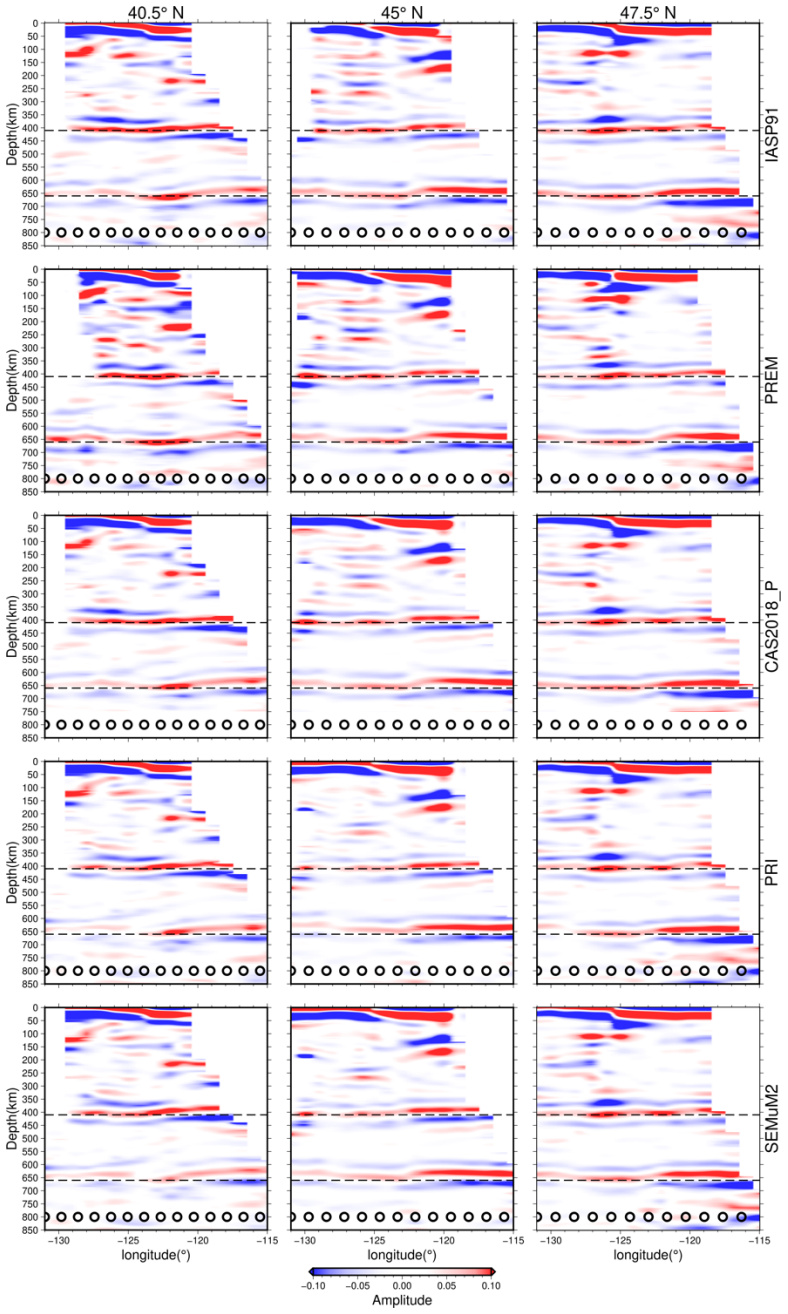

Figure A.7 Migration tests (Vertical cross-sections). Vertical cross-sections similar to Figure 2.4 are shown for the following migration models: IASP91 (Kennett et al., 1995) (top), PREM (Dziewonski & Anderson, 1981) (second row), the 3-D P-velocity anomaly model CAS2018_P (Bodmer et al., 2018) with assuming IASP91 for the reference model and calculating S-wave velocities assuming the Vp/Vs values from IASP91 (third row), 3-D Vs model SEMuM2 (French et al., 2013) with Vp/Vs ratio from IASP91 (bottom), and 3-D Vp and Vs models from PRI (Montelli et al., 2006) (fourth row).

Appendix B Support Information: Global Imaging of the Mantle Transition Zone using SS precursors

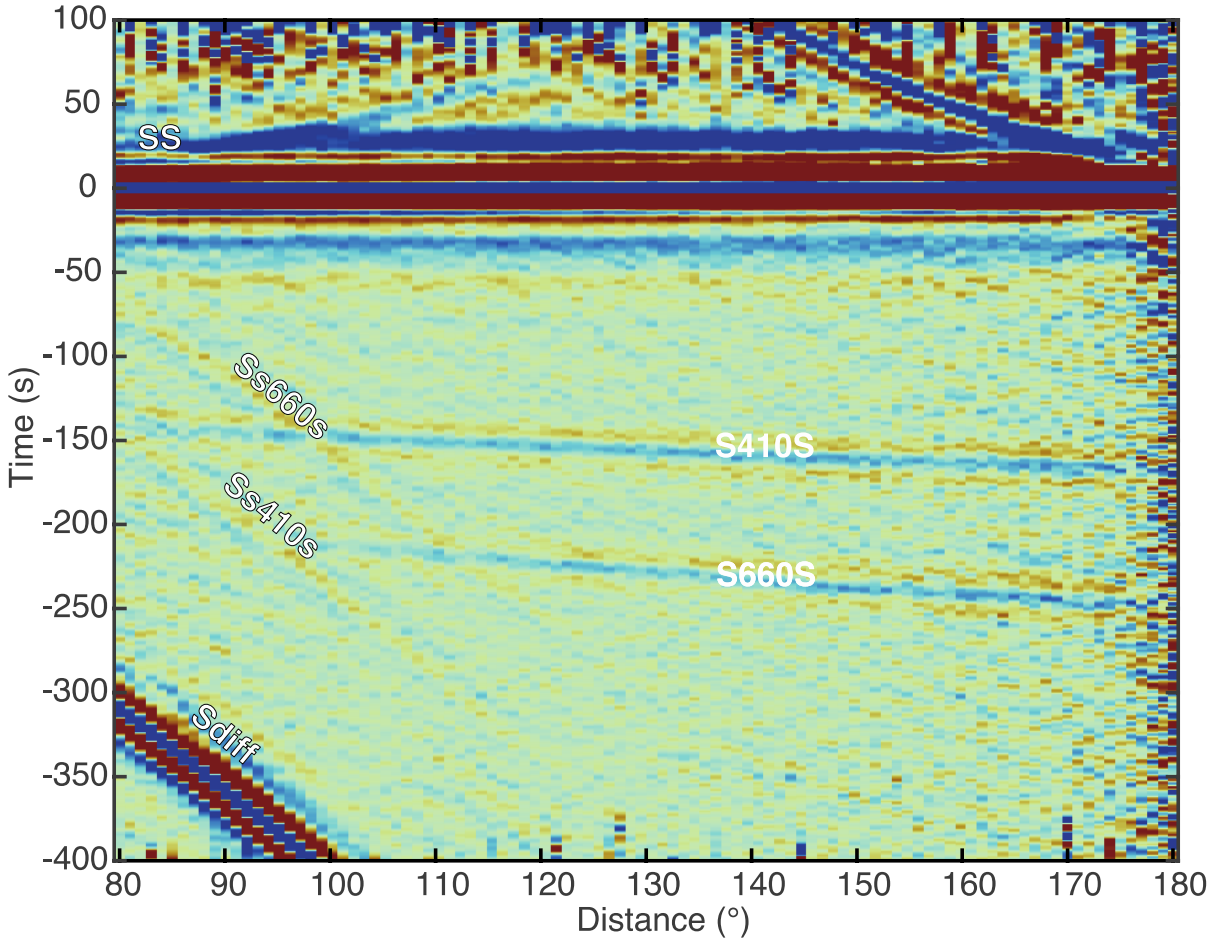

Figure B.1 Global stacks of SS waveforms. The global stacks of our dataset. Waveforms are aligned at the SS and stacked every 1 degree according to the epicentre distance. To avoid Ss410s, Ss660s and other interferences, we restrict our data between 120° to 170° (Coloured region).

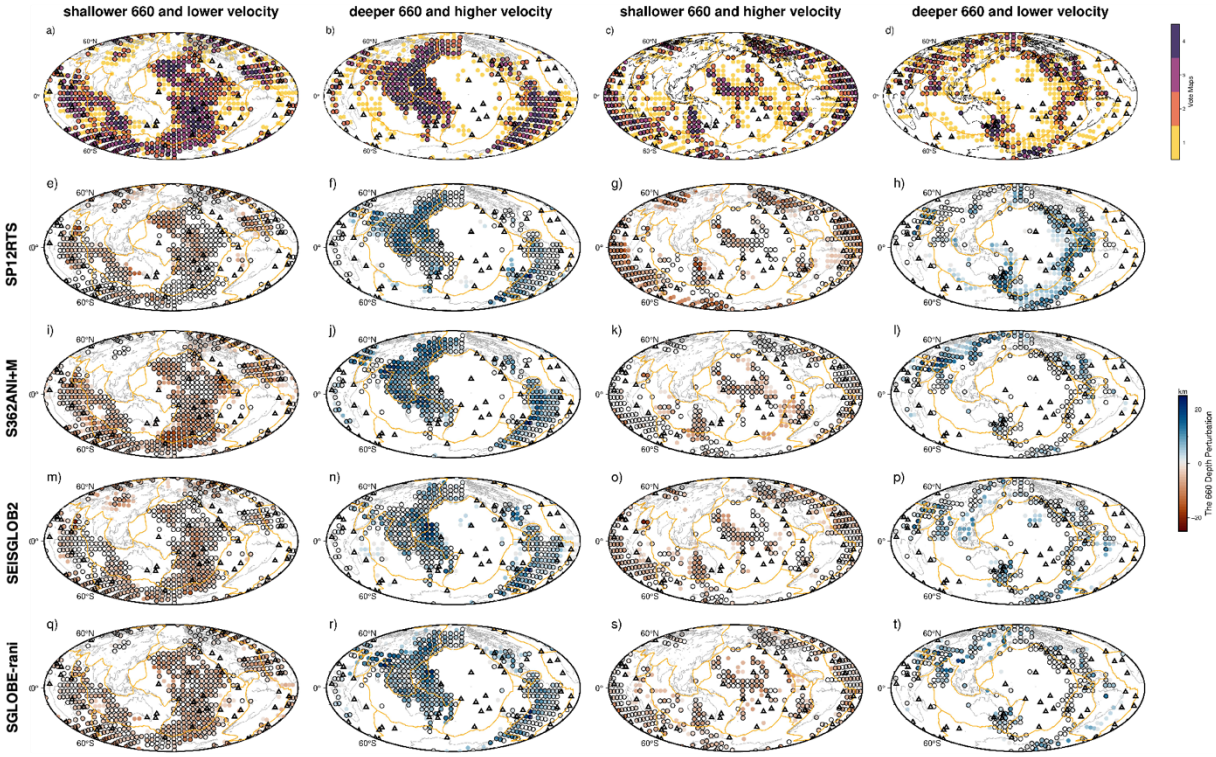

Figure B.2 Patterns by the 660 depth perturbations and velocity perturbations. a) vote maps of a shallower 660 and low-velocity anomaly from 4 models with 3-D crustal and mantle corrections. b) vote maps of a deeper 660 and high-velocity anomaly. c) vote maps of a shallower 660 and high-velocity anomaly. d) vote maps of a deeper 660 and low-velocity anomaly. e) – h), the 660 depth perturbations to its average of patterns corresponding to a) – d) respectively from model SP12RTS. i) – l), from model S362ANI+M, m) – p), from model SEISGLOB2, q) – t), from SGLOBE-rani. Orange lines show plate boundaries (Bird, 2003) and black triangles indicate major hotspots (Courtillot et al., 2003).

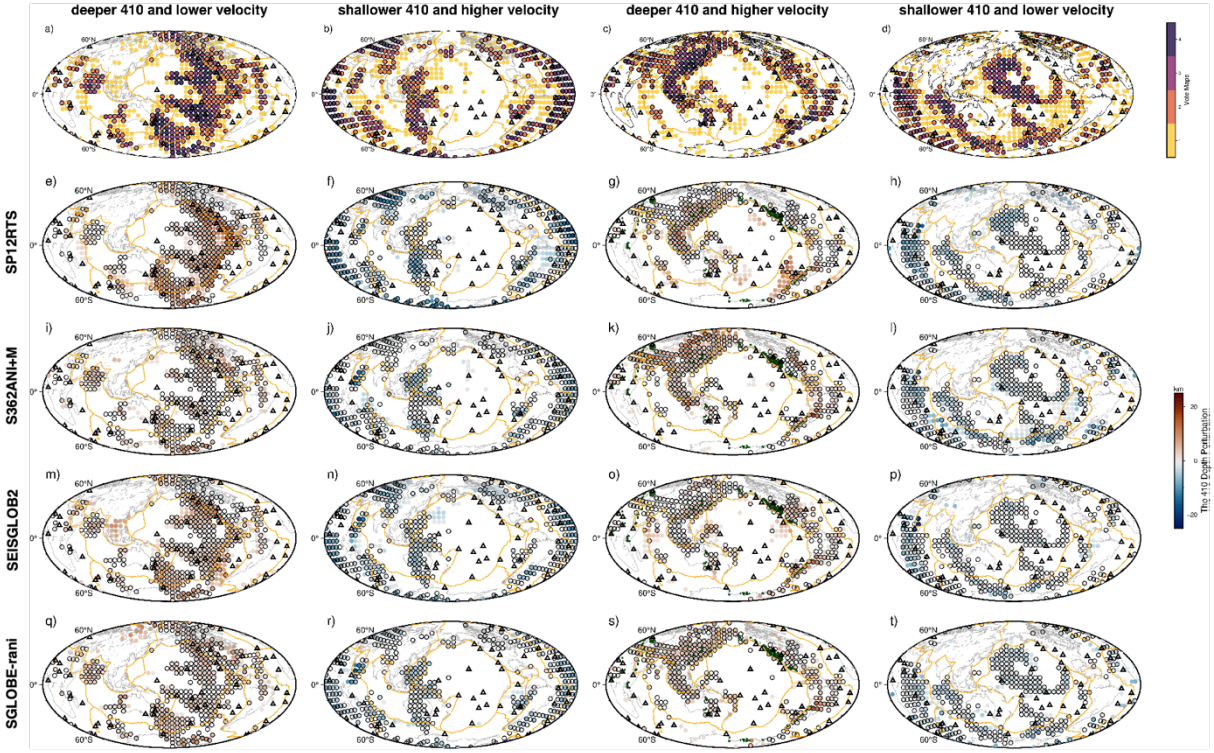

Figure B.3 Patterns by the 410 depth perturbations and velocity perturbations. a) vote maps of a deeper 410 and low-velocity anomaly from 4 models with 3-D crustal and mantle corrections. b) vote maps of a shallower 410 and high-velocity anomaly. c) vote maps of a deeper 410 and high-velocity anomaly. d) vote maps of a shallower 410 and low-velocity anomaly. e) – h), the 410 depth perturbations to its average of patterns corresponding to a) – d) respectively from model SP12RTS. i) – l), from model S362ANI+M, m) – p), from model SEISGLOB2, q) – t), from SGLOBE-rani. Orange lines show plate boundaries (Bird, 2003) and black triangles indicate major hotspots (Courtillot et al., 2003).

Glossary of Terms

MTZ..... The mantle transition zone. The region between the upper mantle and the lower mantle within the Earth.

RF..... Receiver function. A time series, computed from three-component seismograms, provides the relative response of Earth structure near the receiver.

SNR ..... Signal to noise ratio. A value to evaluate the quality of data quantitatively comparing the signal we expect with others (noise).

SS ..... S-wave that is reflected at the Earth's surface and received by the seismic station.

List of References

(ASL)/USGS, A. S. L. (1990). *United States National Seismic Network [Dataset]* https://doi.org/10.7914/SN/US

Abers, G. A., Hu, X., & Sykes, L. R. (1995). Source scaling of earthquakes in the shumagin region, Alaska: time-domain inversions of regional waveforms. *Geophysical Journal International*, *123*(1), 41-58. https://doi.org/10.1111/j.1365-246X.1995.tb06660.x

Abt, D. L., Fischer, K. M., French, S. W., Ford, H. A., Yuan, H., & Romanowicz, B. (2010). North American lithospheric discontinuity structure imaged by Ps and Sp receiver functions. *Journal of Geophysical Research: Solid Earth*, *115*(B9).

Agius, M. R., Rychert, C. A., Harmon, N., & Laske, G. (2017). Mapping the mantle transition zone beneath Hawaii from Ps receiver functions: Evidence for a hot plume and cold mantle downwellings. *Earth and Planetary Science Letters*, *474*, 226-236.

Agius, M. R., Rychert, C. A., Harmon, N., Tharimena, S., & Kendall, J.-M. (2021). A thin mantle transition zone beneath the equatorial Mid-Atlantic Ridge. *Nature*, *589*(7843), 562-566.

Akaogi, M., Ito, E., & Navrotsky, A. (1989). Olivine‐modified spinel‐spinel transitions in the system Mg2SiO4‐Fe2SiO4: Calorimetric measurements, thermochemical calculation, and geophysical application. *Journal of Geophysical Research: Solid Earth*, *94*(B11), 15671-15685.

Allegre, C. J., Manhes, G., & Göpel, C. (1995). The age of the Earth. *Geochimica et Cosmochimica Acta*, *59*(8), 1445-1456.

Ammon, C. J. (1991). The isolation of receiver effects from teleseismic P waveforms. *Bulletin of the Seismological Society of America (BSSA)*, *81*(6), 2504-2510.

Array, I. T. (2003). *USArray Transportable Array [Dataset]* https://doi.org/10.7914/SN/TA

Artemieva, I. (2011). *The Lithosphere: An Interdisciplinary Approach*. Cambridge University Press. https://doi.org/DOI: 10.1017/CBO9780511975417

Baker, M. B., & Stolper, E. M. (1994). Determining the composition of high-pressure mantle melts using diamond aggregates. *Geochimica et Cosmochimica Acta*, *58*(13), 2811-2827.

Ballmer, M. D., Houser, C., Hernlund, J. W., Wentzcovitch, R. M., & Hirose, K. (2017). Persistence of strong silica-enriched domains in the Earth's lower mantle. *Nature Geoscience*, *10*(3), 236-240.

Ballmer, M. D., Schmerr, N. C., Nakagawa, T., & Ritsema, J. (2015). Compositional mantle layering revealed by slab stagnation at~ 1000-km depth. *Science Advances*, *1*(11), e1500815.

Bassin, C., Laske, G., & Masters, G. (2000). The current limits of resolution for surface wave tomography in North America. *EOS Transactions, Fall Meeting Suppliment, AGU*, *81*(F897).

Bell, S. W., Forsyth, D. W., & Ruan, Y. (2015). Removing noise from the vertical component records of ocean‐bottom seismometers: Results from year one of the Cascadia Initiative. *Bulletin of the Seismological Society of America*, *105*(1), 300-313.

Bercovici, D., & Karato, S.-i. (2003). Whole-mantle convection and the transition-zone water filter. *Nature*, *425*(6953), 39-44.

Bezada, M., Faccenda, M., & Toomey, D. (2016). Representing anisotropic subduction zones with isotropic velocity models: A characterization of the problem and some steps on a possible path forward. *Geochemistry, Geophysics, Geosystems*, *17*(8), 3164-3189.

Bina, C. R., & Helffrich, G. (1994). Phase transition Clapeyron slopes and transition zone seismic discontinuity topography. *Journal of Geophysical Research: Solid Earth*, *99*(B8), 15853-15860.

Bird, P. (2003). An updated digital model of plate boundaries. *Geochemistry, Geophysics, Geosystems*, *4*(3).

Blum, J., & Shen, Y. (2004). Thermal, hydrous, and mechanical states of the mantle transition zone beneath southern Africa. *Earth and Planetary Science Letters*, *217*(3-4), 367-378.

Bodmer, M., Toomey, D. R., Hooft, E. E., & Schmandt, B. (2018). Buoyant asthenosphere beneath Cascadia influences megathrust segmentation. *Geophysical Research Letters*, *45*(14), 6954-6962.

Bodmer, M., Toomey, D. R., VanderBeek, B., Hooft, E., & Byrnes, J. S. (2020). Body Wave Tomography of the Cascadia Subduction Zone and Juan de Fuca Plate System: Identifying Challenges and Solutions for Shore‐Crossing Data. *Geochemistry, Geophysics, Geosystems*, *21*(12), e2020GC009316.

Bostock, M. (1998). Mantle stratigraphy and evolution of the Slave province. *Journal of Geophysical Research: Solid Earth*, *103*(B9), 21183-21200.

Bostock, M., & Sacchi, M. (1997). Deconvolution of teleseismic recordings for mantle structure. *Geophysical Journal International*, *129*(1), 143-152.

Bostock, M. G. (1999). Seismic imaging of lithospheric discontinuities and continental evolution. *Lithos*, *48*(1-4), 1-16. <Go to ISI>://000083177600002

Campbell, I. H. (2007). Testing the plume theory. *Chemical Geology*, *241*(3-4), 153-176.

Cao, Q., van der Hilst, R. D., de Hoop, M. V., & Shim, S.-H. (2011). Seismic Imaging of Transition Zone Discontinuities Suggests Hot Mantle West of Hawaii. *Science*, *332*(6033), 1068-1071. https://doi.org/doi:10.1126/science.1202731

Center, N. C. E. D. (2014). *Berkeley Digital Seismic Network (BDSN) [Dataset]* https://doi.org/10.7932/BDSN

Cerveny, V. (2005). *Seismic ray theory*. Cambridge university press.

Chambers, K., Woodhouse, J., & Deuss, A. (2005). Topography of the 410-km discontinuity from PP and SS precursors. *Earth and Planetary Science Letters*, *235*(3-4), 610-622.

Chang, S. J., Ferreira, A. M., Ritsema, J., van Heijst, H. J., & Woodhouse, J. H. (2015). Joint inversion for global isotropic and radially anisotropic mantle structure including crustal thickness perturbations. *Journal of Geophysical Research: Solid Earth*, *120*(6), 4278-4300.

Cheng, C., Bodin, T., Tauzin, B., & Allen, R. M. (2017). Cascadia subduction slab heterogeneity revealed by three‐dimensional receiver function Kirchhoff migration. *Geophysical Research Letters*, *44*(2), 694-701.

Choy, G. L., & Richards, P. G. (1975). Pulse distortion and Hilbert transformation in multiply reflected and refracted body waves. *Bulletin of the Seismological Society of America*, *65*(1), 55-70. https://doi.org/10.1785/bssa0650010055

Christensen, U. R., & Hofmann, A. W. (1994). Segregation of subducted oceanic crust in the convecting mantle. *Journal of Geophysical Research: Solid Earth*, *99*(B10), 19867-19884.

Connolly, J. A. (2005). Computation of phase equilibria by linear programming: a tool for geodynamic modeling and its application to subduction zone decarbonation. *Earth and Planetary Science Letters*, *236*(1-2), 524-541.

Contenti, S., Gu, Y. J., Ökeler, A., & Sacchi, M. D. (2012). Shear wave reflectivity imaging of the Nazca‐South America subduction zone: Stagnant slab in the mantle transition zone? *Geophysical Research Letters*, *39*(2).

Courtillot, V., Davaille, A., Besse, J., & Stock, J. (2003). Three distinct types of hotspots in the Earth's mantle. *Earth and Planetary Science Letters*(205), 295-308.

Crawford, W. C., & Webb, S. C. (2000). Identifying and Removing Tilt Noise from Low-Frequency (0.1 Hz) Seafloor Vertical Seismic Data. *Bulletin of the Seismological Society of America*, *90*(4), 952-963.

Crotwell, H. P., Owens, T. J., & Ritsema, J. (1999). The TauP Toolkit: Flexible seismic travel-time and ray-path utilities. *Seismological Research Letters*, *70*, 154-160.

Dahlen, F., & Tromp, J. (1999). *Theoretical global seismology*. Princeton university press.

Dai, Y., Rychert, C. A., & Harmon, N. (2023). Seismic imaging beneath Cascadia shows shallow mantle flow patterns guide lower mantle upwellings. *Journal of Geophysical Research: Solid Earth*, *128*(9), e2023JB026374.

Dai, Y., Tharimena, S., Rychert, C., & Harmon, N. (2024). A global SS precursor method for imaging discontinuities: the Moho and beyond. *Geophysical Journal International*, *238*(2), 756-763.

Deuss, A. (2009). Global Observations of Mantle Discontinuities Using SS and PP Precursors. *Surveys in Geophysics*, *30*, 301-326.

Deuss, A., & Woodhouse, J. (2001). Seismic Observations of Splitting of the Mid-Transition Zone Discontinuity in Earth's Mantle. *Science*, *294*(5541), 354-357. https://doi.org/doi:10.1126/science.1063524

Deuss, A., & Woodhouse, J. H. (2004). The nature of the Lehmann discontinuity from its seismological Clapeyron slopes. *Earth and Planetary Science Letters*, *225*(3-4), 295-304.

Doran, A. K., & Laske, G. (2017). Ocean‐Bottom Seismometer Instrument Orientations via Automated Rayleigh‐Wave Arrival‐Angle Measurements. *Bulletin of the Seismological Society of America*, *107*(2), 691-708.

Dugda, M. T., Nyblade, A. A., Julia, J., Langston, C. A., Ammon, C. J., & Simiyu, S. (2005). Crustal structure in Ethiopia and Kenya from receiver function analysis: Implications for rift development in eastern Africa. *Journal of Geophysical Research: Solid Earth*, *110*(B1).

Durand, S., Debayle, E., Ricard, Y., Zaroli, C., & Lambotte, S. (2017). Confirmation of a change in the global shear velocity pattern at around 1000 km depth. *Geophysical Journal International*, *211*(3), 1628-1639.

Dziewonski, A. M., & Anderson, D. L. (1981). Preliminary reference Earth model. *Physics of the Earth and Planetary Interiors*, *25*(4), 297-356.

Eagar, K. C., Fouch, M. J., & James, D. E. (2010). Receiver function imaging of upper mantle complexity beneath the Pacific Northwest, United States. *Earth and Planetary Science Letters*, *297*(1-2), 141-153.

Eakin, C. M., Obrebski, M., Allen, R. M., Boyarko, D. C., Brudzinski, M. R., & Porritt, R. (2010). Seismic anisotropy beneath Cascadia and the Mendocino triple junction: Interaction of the subducting slab with mantle flow. *Earth and Planetary Science Letters*, *297*(3-4), 627-632.

Eaton, D. W., Darbyshire, F., Evans, R. L., Grutter, H., Jones, A. G., & Yuan, X. H. (2009). The elusive lithosphere-asthenosphere boundary (LAB) beneath cratons. *Lithos*, *109*(1-2), 1-22. https://doi.org/10.1016/j.lithos.2008.05.009

Faccenda, M., & Dal Zilio, L. (2017). The role of solid–solid phase transitions in mantle convection. *Lithos*, *268*, 198-224.

Fei, Y., Van Orman, J., Li, J., Van Westrenen, W., Sanloup, C., Minarik, W., Hirose, K., Komabayashi, T., Walter, M., & Funakoshi, K.-i. (2004). Experimentally determined postspinel transformation boundary in Mg2SiO4 using MgO as an internal pressure standard and its geophysical implications. *Journal of Geophysical Research: Solid Earth*, *109*(B2).

Fischer, K. M., Ford, H. A., Abt, D. L., & Rychert, C. A. (2010). The Lithosphere-Asthenosphere Boundary. *Annual Review of Earth and Planetary Sciences*, *38*(1), 551-575. https://doi.org/Doi 10.1146/Annurev-Earth-040809-152438

Flanagan, M. P., & Shearer, P. M. (1998). Global mapping of topography on transition zone velocity discontinuities by stacking SS precursors. *Journal of Geophysical Research: Solid Earth*, *103*(B2), 2673-2692.

Frazer, W. D., & Park, J. (2021). Seismic evidence of mid‐mantle water transport beneath the Yellowstone region. *Geophysical Research Letters*, e2021GL095838.

Frazer, W. D., & Park, J. (2023). High-resolution mid-mantle imaging with multiple-taper SS-precursor estimates. *Geophysical Journal International*, *233*(2), 1356-1371. https://doi.org/10.1093/gji/ggac491

French, S., Lekic, V., & Romanowicz, B. (2013). Waveform tomography reveals channeled flow at the base of the oceanic asthenosphere. *Science*, *342*(6155), 227-230.

French, S. W., & Romanowicz, B. (2015). Broad plumes rooted at the base of the Earth's mantle beneath major hotspots. *Nature*, *525*(7567), 95-99.

Fukao, Y., & Obayashi, M. (2013). Subducted slabs stagnant above, penetrating through, and trapped below the 660 km discontinuity. *Journal of Geophysical Research: Solid Earth*, *118*(11), 5920-5938.

Gao, S. S., & Liu, K. H. (2014). Mantle transition zone discontinuities beneath the contiguous United States. *Journal of Geophysical Research: Solid Earth*, *119*(8), 6452-6468.

Ghosh, S., Ohtani, E., Litasov, K. D., Suzuki, A., Dobson, D., & Funakoshi, K. (2013). Effect of water in depleted mantle on post-spinel transition and implication for 660 km seismic discontinuity. *Earth and Planetary Science Letters*, *371*, 103-111.

Goes, S., Agrusta, R., van Hunen, J., & Garel, F. (2017). Subduction-transition zone interaction: A review. *Geosphere*, *13*(3), 644-664.

Gossler, J., & Kind, R. (1995). Seismological evidence for a correlation between lithosphere and mantle transition zone. International Kimberlite Conference: Extended Abstracts,

Grand, S. P., Van der Hilst, R. D., & Widiyantoro, S. (1997). Global seismic tomography: a snapshot of convection in the Earth. *Geological Society of America Today*, *7*(4).

Gu, Y., Dziewonski, A. M., & Agee, C. B. (1998). Global de-correlation of the topography of transition zone discontinuities. *Earth and Planetary Science Letters*, *157*(1-2), 57-67.

Gu, Y. J., & Dziewonski, A. M. (2002). Global variability of transition zone thickness. *Journal of Geophysical Research: Solid Earth*, *107*(B7), ESE 2-1-ESE 2-17.

Hacker, B. R., Kelemen, P. B., & Behn, M. D. (2011). Differentiation of the continental crust by relamination. *Earth and Planetary Science Letters*, *307*(3-4), 501-516.

Hansen, S., & Schmandt, B. (2017). P and S wave receiver function imaging of subduction with scattering kernels. *Geochemistry, Geophysics, Geosystems*, *18*(12), 4487-4502.

Harmon, N., Forsyth, D. W., & Weeraratne, D. S. (2009). Thickening of young Pacific lithosphere from high-resolution Rayleigh wave tomography: A test of the conductive cooling model. *Earth and Planetary Science Letters*, *278*(1-2), 96-106. https://doi.org/10.1016/j.epsl.2008.11.025

Heit, B., Yuan, X. H., Bianchi, M., Kind, R., & Gossler, J. (2010). Study of the lithospheric and upper-mantle discontinuities beneath eastern Asia by SS precursors. *Geophysical Journal International*, *183*(1), 252-266. <Go to ISI>://WOS:000281902600019

Helffrich, G. (2006). Extended-time multitaper frequency domain cross-correlation receiver-function estimation. *Bulletin of the Seismological Society of America*, *96*(1), 344-347.

Hernández, E. R., Brodholt, J., & Alfè, D. (2015). Structural, vibrational and thermodynamic properties of Mg2SiO4 and MgSiO3 minerals from first-principles simulations. *Physics of the Earth and Planetary Interiors*, *240*, 1-24.

Hier-Majumder, S., Ballmer, M. D., Agius, M., Rychert, C., & Harmon, N. (2021). Evidence for melt leakage from the Hawaiian plume above the mantle transition zone. *Physics of the Earth and Planetary Interiors*, *321*, 106813.

Hirose, K. (2002). Phase transitions in pyrolitic mantle around 670‐km depth: Implications for upwelling of plumes from the lower mantle. *Journal of Geophysical Research: Solid Earth*, *107*(B4), ECV 3-1-ECV 3-13.

Hirschmann, M. M., & Dasgupta, R. (2009). The H/C ratios of Earth's near-surface and deep reservoirs, and consequences for deep Earth volatile cycles. *Chemical Geology*, *262*(1-2), 4-16.

Hodgson, I., Illsley‐Kemp, F., Gallacher, R. J., Keir, D., Ebinger, C. J., & Mtelela, K. (2017). Crustal structure at a young continental rift: A receiver function study from the Tanganyika Rift. *Tectonics*, *36*(12), 2806-2822.

Hofmann, A. W. (1997). Mantle geochemistry: the message from oceanic volcanism. *Nature*, *385*(6613), 219-229.

Hooft, E. E., & Detrick, R. S. (1995). Relationship between axial morphology, crustal thickness, and mantle temperature along the Juan de Fuca and Gorda Ridges. *Journal of Geophysical Research: Solid Earth*, *100*(B11), 22499-22508.

Houser, C. (2016). Global seismic data reveal little water in the mantle transition zone. *Earth and Planetary Science Letters*, *448*, 94-101.

Houser, C., Masters, G., Flanagan, M., & Shearer, P. (2008). Determination and analysis of long-wavelength transition zone structure using SS precursors. *Geophysical Journal International*, *174*(1), 178-194. https://doi.org/10.1111/j.1365-246X.2008.03719.x

Huang, Q., Schmerr, N., Waszek, L., & Beghein, C. (2019). Constraints on seismic anisotropy in the mantle transition zone from long‐period SS precursors. *Journal of Geophysical Research: Solid Earth*, *124*(7), 6779-6800.

Hung, T. D., Yang, T., Le, B. M., Yu, Y., Xue, M., Liu, B., Liu, C., Wang, J., Pan, M., & Huong, P. T. (2021). Crustal structure across the extinct mid‐ocean ridge in South China sea from OBS receiver

functions: insights into the spreading rate and magma supply prior to the ridge cessation. *Geophysical Research Letters*, *48*(3), e2020GL089755.

Inoue, T., Irifune, T., Higo, Y., Sanehira, T., Sueda, Y., Yamada, A., Shinmei, T., Yamazaki, D., Ando, J., & Funakoshi, K. (2006). The phase boundary between wadsleyite and ringwoodite in Mg 2 SiO 4 determined by in situ X-ray diffraction. *Physics and Chemistry of Minerals*, *33*, 106-114.

Ishii, T., Huang, R., Fei, H., Koemets, I., Liu, Z., Maeda, F., Yuan, L., Wang, L., Druzhbin, D., Yamamoto, T., Bhat, S., Farla, R., Kawazoe, T., Tsujino, N., Kulik, E., Higo, Y., Tange, Y., & Katsura, T. (2018). Complete agreement of the post-spinel transition with the 660-km seismic discontinuity. *Scientific Reports*, *8*(1), 6358. https://doi.org/10.1038/s41598-018-24832-y

Ito, E., Akaogi, M., Topor, L., & Navrotsky, A. (1990). Negative pressure-temperature slopes for reactions formign MgSiO3 perovskite from calorimetry. *Science*, *249*(4974), 1275-1278.

Ito, E., & Katsura, T. (1989). A temperature profile of the mantle transition zone. *Geophysical Research Letters*, *16*(5), 425-428.

Ito, E., & Takahashi, E. (1989). Postspinel transformations in the system Mg2SiO4 - Fe2SiO4 and some geophysical implications. *Journal of Geophysical Research: Solid Earth*, *94*(B8), 10637-10646.

Janiszewski, H. A., & Abers, G. A. (2015). Imaging the plate interface in the Cascadia seismogenic zone: New constraints from offshore receiver functions. *Seismological Research Letters*, *86*(5), 1261-1269.

Jellinek, A. M., & Manga, M. (2002). The influence of a chemical boundary layer on the fixity, spacing and lifetime of mantle plumes. *Nature*, *418*(6899), 760-763.

Jellinek, A. M., & Manga, M. (2004). Links between long - lived hot spots, mantle plumes, d ″ , and plate tectonics. *Reviews of Geophysics*, *42*(3).

Jenkins, J., Cottaar, S., White, R., & Deuss, A. (2016). Depressed mantle discontinuities beneath Iceland: Evidence of a garnet controlled 660 km discontinuity? *Earth and Planetary Science Letters*, *433*, 159-168.

Julià, J. (2007). Constraining velocity and density contrasts across the crust—mantle boundary with receiver function amplitudes. *Geophysical Journal International*, *171*(1), 286-301.

Karato, S.-i., & Wu, P. (1993). Rheology of the Upper Mantle: A Synthesis. *Science*, *260*(5109), 771-778. https://doi.org/doi:10.1126/science.260.5109.771

Katsura, T., & Ito, E. (1989). The system Mg2SiO4 - Fe2SiO4 at high pressures and temperatures: Precise determination of stabilities of olivine, modified spinel, and spinel. *Journal of Geophysical Research: Solid Earth*, *94*(B11), 15663-15670.

Katsura, T., Yamada, H., Nishikawa, O., Song, M., Kubo, A., Shinmei, T., Yokoshi, S., Aizawa, Y., Yoshino, T., & Walter, M. J. (2004). Olivine - wadsleyite transition in the system (Mg, Fe) 2SiO4. *Journal of Geophysical Research: Solid Earth*, *109*(B2).

Katsura, T., Yamada, H., Shinmei, T., Kubo, A., Ono, S., Kanzaki, M., Yoneda, A., Walter, M. J., Ito, E., & Urakawa, S. (2003). Post-spinel transition in Mg2SiO4 determined by high P–T in situ X-ray diffractometry. *Physics of the Earth and Planetary Interiors*, *136*(1-2), 11-24.

Kawakatsu, H., Kumar, P., Takei, Y., Shinohara, M., Kanazawa, T., Araki, E., & Suyehiro, K. (2009). Seismic evidence for sharp lithosphere-asthenosphere boundaries of oceanic plates. *Science*, *324*(5926), 499-502.

Kellogg, L. H., Hager, B. H., & van der Hilst, R. D. (1999). Compositional stratification in the deep mantle. *Science*, *283*(5409), 1881-1884.

Kennett, B., & Engdahl, E. (1991). Traveltimes for global earthquake location and phase identification. *Geophysical Journal International*, *105*(2), 429-465.

Kennett, B. L., Engdahl, E., & Buland, R. (1995). Constraints on seismic velocities in the Earth from traveltimes. *Geophysical Journal International*, *122*(1), 108-124.

Kim, H., Kawakatsu, H., Akuhara, T., Shinohara, M., Shiobara, H., Sugioka, H., & Takagi, R. (2021). Receiver function imaging of the amphibious NE Japan subduction zone - effects of low - velocity sediment layer - . *Journal of Geophysical Research: Solid Earth*, e2021JB021918.

Kim, Y., Miller, M. S., Pearce, F., & Clayton, R. W. (2012). Seismic imaging of the Cocos plate subduction zone system in central Mexico. *Geochemistry, Geophysics, Geosystems*, *13*(7), n/a-n/a. https://doi.org/10.1029/2012gc004033

Koelemeijer, P., Ritsema, J., Deuss, A., & Van Heijst, H.-J. (2016). SP12RTS: a degree-12 model of shear-and compressional-wave velocity for Earth's mantle. *Geophysical Journal International*, *204*(2), 1024-1039.

Koppers, A. A., Becker, T. W., Jackson, M. G., Konrad, K., Müller, R. D., Romanowicz, B., Steinberger, B., & Whittaker, J. M. (2021). Mantle plumes and their role in Earth processes. *Nature Reviews Earth & Environment*, *2*(6), 382-401.

Kumar, P., Kawakatsu, H., Shinohara, M., Kanazawa, T., Araki, E., & Suyehiro, K. (2011). P and S receiver function analysis of seafloor borehole broadband seismic data. *Journal of Geophysical Research: Solid Earth*, *116*(B12).

Kumar, P., Kind, R., Yuan, X., & Mechie, J. (2012). USArray receiver function images of the lithosphere-asthenosphere boundary. *Seismological Research Letters*, *83*(3), 486-491.

Landuyt, W., & Bercovici, D. (2009). Variations in planetary convection via the effect of climate on damage. *Earth and Planetary Science Letters*, *277*(1-2), 29-37.

Langston, C. A. (1979). Structure under Mount Rainier, Washington, inferred from teleseismic body waves. *Journal of Geophysical Research: Solid Earth*, *84*(B9), 4749-4762.

Laske, G., Masters, G., Ma, Z., & Pasyanos, M. (2012). CRUST1.0: An updated global model of Earth's crust. *Geophysical Research Abstracts*.

Laske, G., Masters, G., Ma, Z., & Pasyanos, M. (2013). Update on CRUST1. 0—A 1-degree global model of Earth's crust. Geophys. res. abstr,

Lawrence, J. F., & Shearer, P. M. (2006). A global study of transition zone thickness using receiver functions. *Journal of Geophysical Research: Solid Earth*, *111*(B6).

Lawrence, J. F., & Shearer, P. M. (2008). Imaging mantle transition zone thickness with SdS-SS finite-frequency sensitivity kernels. *Geophysical Journal International*, *174*(1), 143-158. https://doi.org/10.1111/j.1365-246X.2007.03673.x

Lay, T., & Wallace, T. C. (1995). *Modern global seismology* (Vol. 58). Elsevier.

Lee, D. K., & Grand, S. P. (1996). Depth of the upper mantle discontinuities beneath the East Pacific Rise. *Geophysical Research Letters*, *23*(23), 3369-3372.

Lekić, V., & Fischer, K. M. (2017). Interpreting spatially stacked Sp receiver functions. *Geophysical Journal International*, *210*(2), 874-886.

Lessing, S., Thomas, C., Rost, S., Cobden, L., & Dobson, D. P. (2014). Mantle transition zone structure beneath India and Western China from migration of PP and SS precursors. *Geophysical Journal International*, *197*(1), 396-413.

Ligorria, J. P., & Ammon, C. J. (1999). Iterative Deconvolution and Receiver-Function Estimation. *Bulletin of the Seismological Society of America*, 1395-1400.

Litasov, K., Ohtani, E., Sano, A., Suzuki, A., & Funakoshi, K. (2005). In situ X-ray diffraction study of post-spinel transformation in a peridotite mantle: implication for the 660-km discontinuity. *Earth and Planetary Science Letters*, *238*(3-4), 311-328.

Long, X., Ballmer, M. D., Córdoba, A. M. C., & Li, C. F. (2019). Mantle melting and intraplate volcanism due to self‐buoyant hydrous upwellings from the stagnant slab that are conveyed by small‐scale convection. *Geochemistry, Geophysics, Geosystems*, *20*(11), 4972-4997.

Mao, W., & Zhong, S. (2018). Slab stagnation due to a reduced viscosity layer beneath the mantle transition zone. *Nature Geoscience*, *11*(11), 876-881.

Marquardt, H., & Miyagi, L. (2015). Slab stagnation in the shallow lower mantle linked to an increase in mantle viscosity. *Nature Geoscience*, *8*(4), 311-314.

Martin-Short, R., Allen, R. M., Bastow, I. D., Totten, E., & Richards, M. A. (2015). Mantle flow geometry from ridge to trench beneath the Gorda–Juan de Fuca plate system. *Nature Geoscience*, *8*(12), 965-968.

Masters, G., Johnson, S., Laske, G., & Bolton, H. (1996). A shear-velocity model of the mantle. *Philosophical Transactions of the Royal Society a-Mathematical Physical and Engineering Sciences*, *354*(1711), 1385-1410. https://doi.org/DOI 10.1098/rsta.1996.0054

McNamara, A. K., & Zhong, S. (2005). Thermochemical structures beneath Africa and the Pacific Ocean. *Nature*, *437*(7062), 1136-1139.

Mehouachi, F., & Singh, S. C. (2018). Water-rich sublithospheric melt channel in the equatorial Atlantic Ocean. *Nature Geoscience*, *11*(1), 65-69. https://doi.org/10.1038/s41561-017-0034-z

Meier, U., Curtis, A., & Trampert, J. (2007). Global crustal thickness from neural network inversion of surface wave data. *Geophysical Journal International*, *169*(2), 706-722. https://doi.org/10.1111/j.1365-246X.2007.03373.x

Meier, U., Trampert, J., & Curtis, A. (2009). Global variations of temperature and water content in the mantle transition zone from higher mode surface waves. *Earth and Planetary Science Letters*, *282*(1-4), 91-101.

Mohorovičić, A. (1910). Potres od 8. X. 1909. *Godišnje izvješće zagrebačkog meteorološkog opservatorija za godinu 1909*.

Montagner, J. P., & Tanimoto, T. (1991). Global upper mantle tomography of seismic velocities and anisotropies. *Journal of Geophysical Research*, *96*, 15.

Montelli, R., Nolet, G., Dahlen, F., & Masters, G. (2006). A catalogue of deep mantle plumes: New results from finite‐frequency tomography. *Geochemistry, Geophysics, Geosystems*, *7*(11).

Montelli, R., Nolet, G., Dahlen, F., Masters, G., Engdahl, E. R., & Hung, S.-H. (2004). Finite-frequency tomography reveals a variety of plumes in the mantle. *Science*, *303*(5656), 338-343.

Morgan, J. P., & Morgan, W. J. (1999). Two-stage melting and the geochemical evolution of the mantle: a recipe for mantle plum-pudding. *Earth and Planetary Science Letters*, *170*(3), 215-239.

Morgan, W. J. (1971). Convection plumes in the lower mantle. *Nature*, *230*, 42-43.

Morishima, H., Kato, T., Suto, M., Ohtani, E., Urakawa, S., Utsumi, W., Shimomura, O., & Kikegawa, T. (1994). The phase boundary between α-and β-Mg2SiO4 determined by in situ X-ray observation. *Science*, *265*(5176), 1202-1203.

Moulik, P., & Ekström, G. (2014). An anisotropic shear velocity model of the Earth's mantle using normal modes, body waves, surface waves and long-period waveforms. *Geophysical Journal International*, *199*(3), 1713-1738.

Müller, R. D., Cannon, J., Qin, X., Watson, R. J., Gurnis, M., Williams, S., Pfaffelmoser, T., Seton, M., Russell, S. H., & Zahirovic, S. (2018). GPlates: Building a virtual Earth through deep time. *Geochemistry, Geophysics, Geosystems*, *19*(7), 2243-2261.

Müller, R. D., Sdrolias, M., Gaina, C., & Roest, W. R. (2008). Age, spreading rates, and spreading asymmetry of the world's ocean crust. *Geochemistry, Geophysics, Geosystems*, *9*(4).

Müller, R. D., Zahirovic, S., Williams, S. E., Cannon, J., Seton, M., Bower, D. J., Tetley, M. G., Heine, C., Le Breton, E., & Liu, S. (2019). A global plate model including lithospheric deformation along major rifts and orogens since the Triassic. *Tectonics*, *38*(6), 1884-1907.

Nataf, H. C., & Ricard, Y. (1996). 3SMAC: An a priori tomographic model of the upper mantle based on geophysical modeling. *Physics of the Earth and Planetary Interiors*, *95*(1-2), 101-122. https://doi.org/Doi 10.1016/0031-9201(95)03105-7

Nissen-Meyer, T., van Driel, M., Stähler, S. C., Hosseini, K., Hempel, S., Auer, L., Colombi, A., & Fournier, A. (2014). AxiSEM: broadband 3-D seismic wavefields in axisymmetric media. *Solid Earth*, *5*(1), 425-445. https://doi.org/10.5194/se-5-425-2014

Nissen‐Meyer, T., Fournier, A., & Dahlen, F. A. (2007). A two‐dimensional spectral‐element method for computing spherical‐earth seismograms—I. Moment‐tensor source. *Geophysical Journal International*, *168*(3), 1067-1092. https://doi.org/10.1111/j.1365-246X.2006.03121.x

Niu, F., & Li, J. (2011). Component azimuths of the CEArray stations estimated from P-wave particle motion. *Earthquake Science*, *24*, 3-13.

Niu, F., Solomon, S. C., Silver, P. G., Suetsugu, D., & Inoue, H. (2002). Mantle transition-zone structure beneath the South Pacific Superswell and evidence for a mantle plume underlying the Society hotspot. *Earth and Planetary Science Letters*, *198*(3-4), 371-380.

Nolet, G. (1987). Seismic wave propagation and seismic tomography. In *Seismic tomography: With applications in global seismology and exploration geophysics* (pp. 1-23). Springer.

Nolet, G., Allen, R., & Zhao, D. (2007). Mantle plume tomography. *Chemical Geology*, *241*(3-4), 248-263.

OBSIP, I. (2011). *Cascadia Initiative Community Experiment - OBS Component [Dataset]* https://doi.org/10.7914/SN/7D_2011

Oppenheim, A. V., & Schafer, R. W. (1975a). *Digital Signal Processing* (Vol. 19752). Prentice-Hall, Englewood Cliffs, NJ.

Oppenheim, A. V., & Schafer, R. W. (1975b). *Digital Signal Processing*. Prentice-Hall, Inc.

Park, J., & Levin, V. (2000). Receiver Functions from Multiple-Taper Spectral Correlation Estimates. *Bulletin of the Seismological Society of America*, *90*(6), 1507-1520. https://doi.org/10.1785/0119990122

Park, J., Lindberg, C. R., & Vernon III, F. L. (1987). Multitaper spectral analysis of high‐frequency seismograms. *Journal of Geophysical Research: Solid Earth*, *92*(B12), 12675-12684.

Portner, D. E., Beck, S., Zandt, G., & Scire, A. (2017). The nature of subslab slow velocity anomalies beneath South America. *Geophysical Research Letters*, *44*(10), 4747-4755.

Price, K. V., Storn, R. M., & Lampinen, J. A. (2005). *Differential Evolution: A Practical Approach to Global Optimization* Springer.

Revenaugh, J., & Sipkin, S. (1994). Seismic evidence for silicate melt atop the 410-km mantle discontinuity. *Nature*, *369*(6480), 474-476.

Rickers, F., Fichtner, A., & Trampert, J. (2013). The Iceland–Jan Mayen plume system and its impact on mantle dynamics in the North Atlantic region: evidence from full-waveform inversion. *Earth and Planetary Science Letters*, *367*, 39-51.

Rigden, S. M., Gwanmesia, G. D., Gerald, J. D. F., Jackson, L., & Liebermann, R. C. (1991). Spinel elasticity and seismic structure of the transition zone of the mantle. *Nature*, *354*(6349), 143-145.

Ringwood, A. E. (1975). Composition and Petrology of the Earth's Mantle. *MacGraw-Hill*, *618*.

Ringwood, A. E. (1991). Phase transformations and their bearing on the constitution and dynamics of the mantle. *Geochimica et Cosmochimica Acta*, *55*(8), 2083-2110.

Ritsema, J., Deuss, a. A., Van Heijst, H., & Woodhouse, J. (2011). S40RTS: a degree-40 shear-velocity model for the mantle from new Rayleigh wave dispersion, teleseismic traveltime and normal-mode splitting function measurements. *Geophysical Journal International*, *184*(3), 1223-1236.

Ritsema, J., Van Heijst, H. J., & Woodhouse, J. H. (2004). Global transition zone tomography. *Journal of Geophysical Research: Solid Earth*, *109*(B2).

Ritsema, J., Xu, W., Stixrude, L., & Lithgow-Bertelloni, C. (2009). Estimates of the transition zone temperature in a mechanically mixed upper mantle. *Earth and Planetary Science Letters*, *277*(1-2), 244-252.

Roy Chowdhury, K. (2020). Deep Seismic Reflection and Refraction Profiling. In H. K. Gupta (Ed.), *Encyclopedia of Solid Earth Geophysics* (pp. 1-18). Springer International Publishing. https://doi.org/10.1007/978-3-030-10475-7_226-1

Rychert, C. A., Fischer, K. M., & Rondenay, S. (2005a). A sharp lithosphere-asthenosphere boundary imaged beneath eastern North America. *Nature*, *436*(7050), 542-545. <Go to ISI>://000230788800058

Rychert, C. A., Fischer, K. M., & Rondenay, S. (2005b). A sharp lithosphere–asthenosphere boundary imaged beneath eastern North America. *Nature*, *436*(7050), 542-545.

Rychert, C. A., Hammond, J. O., Harmon, N., Michael Kendall, J., Keir, D., Ebinger, C., Bastow, I. D., Ayele, A., Belachew, M., & Stuart, G. (2012a). Volcanism in the Afar Rift sustained by decompression melting with minimal plume influence. *Nature Geoscience*, *5*(6), 406-409.

Rychert, C. A., & Harmon, N. (2016). Stacked P‐to‐S and S‐to‐P receiver functions determination of crustal thickness, Vp, and Vs: The H‐V stacking method. *Geophysical Research Letters*, *43*(4), 1487-1494.

Rychert, C. A., Harmon, N., Constable, S., & Wang, S. (2020). The Nature of the Lithosphere-Asthenosphere Boundary. *Journal of Geophysical Research: Solid Earth*, *125*(10), e2018JB016463. https://doi.org/10.1029/2018jb016463

Rychert, C. A., Harmon, N., & Ebinger, C. (2014a). Receiver function imaging of lithospheric structure and the onset of melting beneath the Galápagos Archipelago. *Earth and Planetary Science Letters*, *388*, 156-165.

Rychert, C. A., Harmon, N., & Schmerr, N. (2014b). Synthetic waveform modelling of SS precursors from anisotropic upper-mantle discontinuities. *Geophysical Journal International*, *196*(3), 1694-1705.

Rychert, C. A., Harmon, N., & Tharimena, S. (2018a). Scattered wave imaging of the oceanic plate in Cascadia. *Science Advances*, *4*(2), eaao1908.

Rychert, C. A., Harmon, N., & Tharimena, S. (2018b). Seismic Imaging of the Base of the Ocean Plates. *Lithospheric Discontinuities*, 71-87. https://doi.org/doi:10.1002/9781119249740.ch4

10.1002/9781119249740.ch4 (Geophysical Monograph Series)

Rychert, C. A., Laske, G., Harmon, N., & Shearer, P. M. (2013). Seismic imaging of melt in a displaced Hawaiian plume. *Nature Geoscience*, *6*(8), 657-660. https://doi.org/10.1038/ngeo1878

Rychert, C. A., Rondenay, S., & Fischer, K. M. (2007). P-to-S and S-to-P imaging of a sharp lithosphere-asthenosphere boundary beneath eastern North America. *Journal of Geophysical Research-Solid Earth*, *112*(B8). https://doi.org/Artn B08314

10.1029/2006jb004619

Rychert, C. A., Schmerr, N., & Harmon, N. (2012b). The Pacific lithosphere-asthenosphere boundary: Seismic imaging and anisotropic constraints from SS waveforms. *Geochemistry Geophysics Geosystems*, *13*. https://doi.org/Artn Q0ak10

10.1029/2012gc004194

Rychert, C. A., & Shearer, P. M. (2009). A global view of the lithosphere-asthenosphere boundary. *Science*, *324*(5926), 495-498.

Rychert, C. A., & Shearer, P. M. (2010a). Resolving crustal thickness using SS waveform stacks. *Geophysical Journal International*, *180*(3), 1128-1137.

Rychert, C. A., & Shearer, P. M. (2010b). Resolving crustal thickness using SS waveform stacks. *Geophys. J. Int.*, *180*(3), 1128-1137. https://doi.org/10.1111/j.1365-246X.2009.04497.x (10.1111/J.1365-246x.2009.04497.X)

Rychert, C. A., & Shearer, P. M. (2011). Imaging the lithosphere-asthenosphere boundary beneath the Pacific using SS waveform modeling. *Journal of Geophysical Research-Solid Earth*, *116*. <Go to ISI>://WOS:000293345400003

Rychert, C. A., Shearer, P. M., & Fischer, K. M. (2010). Scattered wave imaging of the lithosphere–asthenosphere boundary. *Lithos*, *120*(1-2), 173-185.

Satterthwaite, F. E. (1946). An approximate distribution of estimates of variance components. *Biometrics bulletin*, *2*(6), 110-114.

Schmandt, B., Dueker, K., Humphreys, E., & Hansen, S. (2012). Hot mantle upwelling across the 660 beneath Yellowstone. *Earth and Planetary Science Letters*, *331*, 224-236.

Schmandt, B., Jacobsen, S. D., Becker, T. W., Liu, Z., & Dueker, K. G. (2014). Dehydration melting at the top of the lower mantle. *Science*, *344*(6189), 1265-1268.

Schmerr, N. (2012). The Gutenberg Discontinuity: Melt at the Lithosphere-Asthenosphere Boundary. *Science*, *335*(6075), 1480-1483. https://doi.org/10.1126/science.1215433

Schmerr, N., & Garnero, E. (2006). Investigation of upper mantle discontinuity structure beneath the central Pacific using SS precursors. *Journal of Geophysical Research-Solid Earth*, *111*(B8). <Go to ISI>://WOS:000239993800007

Shearer, P. M. (1990). Seismic imaging of upper-mantle structure with new evidence for a 520-km discontinuity. *Nature*, *344*(6262), 121-126.

Shearer, P. M. (1991). Constraints on Upper Mantle Discontinuities from Observations of Long-Period Reflected and Converted Phases. *Journal of Geophysical Research-Solid Earth*, *96*(B11), 18147-18182. https://doi.org/Doi 10.1029/91jb01592

Shearer, P. M. (1993). Global mapping of upper mantle reflectors from long-period SS precursors. *Geophysical Journal International*, *115*(3), 878-904. https://doi.org/10.1111/j.1365-246X.1993.tb01499.x

Shearer, P. M. (2019). *Introduction to seismology*. Cambridge university press.

Shearer, P. M., Flanagan, M. P., & Hedlin, M. A. H. (1999). Experiments in migration processing of SS precursor data to image upper mantle discontinuity structure. *Journal of Geophysical Research-Solid Earth*, *104*(B4), 7229-7242. https://doi.org/Doi 10.1029/1998jb900119

Shearer, P. M., & Masters, T. G. (1992). Global mapping of topography on the 660-km discontinuity. *Nature*, *355*(6363), 791-796.

Shen, Y., Sheehan, A. F., Dueker, K. G., de Groot–Hedlin, C., & Gilbert, H. (1998). Mantle discontinuity structure beneath the southern East Pacific Rise from P-to-S converted phases. *Science*, *280*(5367), 1232-1235.

Shibutani, T., Ueno, T., & Hirahara, K. (2008). Improvement in the extended-time multitaper receiver function estimation technique. *Bull. Seis. Soc. Am.*, *98*(2), 812-816. https://doi.org/10.1785/0120070226

Sleep, N. H. (2005). Evolution of the continental lithosphere. *Annu. Rev. Earth Planet. Sci.*, *33*(1), 369-393.

Smyth, J. R., & Frost, D. J. (2002). The effect of water on the 410‐km discontinuity: An experimental study. *Geophysical Research Letters*, *29*(10), 123-121-123-124.

Song, T. A., & Kim, Y. (2011). Anisotropic uppermost mantle in young subducted slab underplating Central Mexico. *Nature Geoscience*, *5*(1), 55-59.

Stachnik, J. C., Sheehan, A. F., Zietlow, D. W., Yang, Z., Collins, J., & Ferris, A. (2012). Determination of New Zealand Ocean Bottom Seismometer Orientation via Rayleigh-Wave Polarization. *Seismological Research Letters*, *83*, 704-713. https://doi.org/10.1785/0220110128

Stern, T. A., Henrys, S. A., Okaya, D., Louie, J. N., Savage, M. K., Lamb, S., Sato, H., Sutherland, R., & Iwasaki, T. (2015). A seismic reflection image for the base of a tectonic plate. *Nature*, *518*(7537), 85-88. https://doi.org/10.1038/nature14146

Stixrude, L., & Lithgow-Bertelloni, C. (2011). Thermodynamics of mantle minerals – II. Phase equilibria. *Geophysical Journal International*, *184*(3), 1180-1213. https://doi.org/https://doi.org/10.1111/j.1365-246X.2010.04890.x

Storn, R., & Price, K. (1997). Differential evolution - A simple and efficient heuristic for global optimization over continuous spaces. *Journal of Global Optimization*, *11*(4), 341-359. https://doi.org/Doi 10.1023/A:1008202821328

Su, W. j., Woodward, R. L., & Dziewonski, A. M. (1994). Degree 12 model of shear velocity heterogeneity in the mantle. *Journal of Geophysical Research: Solid Earth*, *99*(B4), 6945-6980.

Suetsugu, D., Inoue, T., Yamada, A., Zhao, D., & Obayashi, M. (2006). Towards mapping the three-dimensional distribution of water in the transition zone from P-velocity tomography and 660-km discontinuity depths. *GEOPHYSICAL MONOGRAPH-AMERICAN GEOPHYSICAL UNION*, *168*, 237.

Suzuki, A., Ohtani, E., Morishima, H., Kubo, T., Kanbe, Y., Kondo, T., Okada, T., Terasaki, H., Kato, T., & Kikegawa, T. (2000). In situ determination of the phase boundary between wadsleyite and ringwoodite in Mg2SiO4. *Geophysical Research Letters*, *27*(6), 803-806.

Tauzin, B., Debayle, E., & Wittlinger, G. (2010). Seismic evidence for a global low-velocity layer within the Earth's upper mantle. *Nature Geoscience*, *3*(10), 718-721.

Tauzin, B., Kim, S., & Afonso, J. C. (2018). Multiple phase changes in the mantle transition zone beneath northeast Asia: Constraints from teleseismic reflected and converted body waves. *Journal of Geophysical Research: Solid Earth*, *123*(8), 6636-6657.

Tauzin, B., & Ricard, Y. (2014). Seismically deduced thermodynamics phase diagrams for the mantle transition zone. *Earth and Planetary Science Letters*, *401*, 337-346.

Tharimena, S., Rychert, C., & Harmon, N. (2017a). A unified continental thickness from seismology and diamonds suggests a melt-defined plate. *Science*, *357*(6351), 580-583.

Tharimena, S., Rychert, C., Harmon, N., & White, P. (2017b). Imaging Pacific lithosphere seismic discontinuities—Insights from SS precursor modeling. *Journal of Geophysical Research: Solid Earth*, *122*(3), 2131-2152.

Tharimena, S., Rychert, C. A., & Harmon, N. (2016). Seismic imaging of a mid-lithospheric discontinuity beneath Ontong Java Plateau. *Earth and Planetary Science Letters*, *450*, 62-70.

Thomson, D. J. (1982). Spectrum estimation and harmonic analysis. *Proceedings of the IEEE*, *70*(9), 1055-1096.

Tian, D., Lv, M., Wei, S. S., Dorfman, S. M., & Shearer, P. M. (2020). Global variations of Earth's 520- and 560-km discontinuities. *Earth and Planetary Science Letters*, *552*, 116600.

Toomey, D. R., Allen, R. M., Barclay, A. H., Bell, S. W., Bromirski, P. D., Carlson, R. L., Chen, X., Collins, J. A., Dziak, R. P., & Evers, B. (2014). The Cascadia Initiative: A sea change in seismological studies of subduction zones. *Oceanography*, *27*(2), 138-150.

Tsekhmistrenko, M., Sigloch, K., Hosseini, K., & Barruol, G. (2021). A tree of Indo-African mantle plumes imaged by seismic tomography. *Nature Geoscience*, *14*(8), 612-619.

van Driel, M., Krischer, L., Stähler, S. C., Hosseini, K., & Nissen-Meyer, T. (2015). Instaseis: instant global seismograms based on a broadband waveform database. *Solid Earth*, *6*(2), 701-717. https://doi.org/10.5194/se-6-701-2015

Vinnik, L. (1977). Detection of waves converted from P to SV in the mantle. *Physics of the Earth and Planetary Interiors*, *15*(1), 39-45.

Vinnik, L., & Farra, V. (2007). Low S velocity atop the 410-km discontinuity and mantle plumes. *Earth and Planetary Science Letters*, *262*(3-4), 398-412.

Vinnik, L. P. (2019). Receiver Function Seismology. *Izvestiya, Physics of the Solid Earth*, *55*(1), 12-21. https://doi.org/10.1134/S1069351319010130

Wang, P., Zhou, Y., Xu, M., Zhang, H., Chen, X., & Guo, L. (2022). Investigation of Effects of Near‐Surface Complexities on Measurement of Mantle Discontinuity Using SS and Its Precursors. *Journal of Geophysical Research: Solid Earth*, *127*(9), e2022JB024485.

Wang, W., Zhang, H., Brodholt, J. P., & Wu, Z. (2021). Elasticity of hydrous ringwoodite at mantle conditions: Implication for water distribution in the lowermost mantle transition zone. *Earth and Planetary Science Letters*, *554*, 116626.

Wang, X., Chen, L., Wang, K., Chen, Q.-F., Zhan, Z., & Yang, J. (2024). Seismic evidence for melt-rich lithosphere-asthenosphere boundary beneath young slab at Cascadia. *Nature Communications*, *15*(1), 3504.

Wang, Z., & Wang, Y. (2022). Global water distribution in the mantle transition zone from a seismic isotropic velocity model and mineral physics modeling. *Frontiers in Earth Science*, *10*, 984063.

Washington, U. o. (1963). *Pacific Northwest Seismic Network - University of Washington [Dataset]* https://doi.org/10.7914/SN/UW

Waszek, L., Tauzin, B., Schmerr, N. C., Ballmer, M. D., & Afonso, J. C. (2021). A poorly mixed mantle transition zone and its thermal state inferred from seismic waves. *Nature Geoscience*, *14*(12), 949-955. https://doi.org/10.1038/s41561-021-00850-w

Wei, S. S., & Shearer, P. M. (2017). A sporadic low‐velocity layer atop the 410 km discontinuity beneath the Pacific Ocean. *Journal of Geophysical Research: Solid Earth*, *122*(7), 5144-5159.

Xu, W., Lithgow-Bertelloni, C., Stixrude, L., & Ritsema, J. (2008). The effect of bulk composition and temperature on mantle seismic structure. *Earth and Planetary Science Letters*, *275*(1-2), 70-79.

Yang, J., & Faccenda, M. (2020). Intraplate volcanism originating from upwelling hydrous mantle transition zone. *Nature*, *579*(7797), 88-91.

Ye, Y., Gu, C., Shim, S. H., Meng, Y., & Prakapenka, V. (2014). The postspinel boundary in pyrolitic compositions determined in the laser‐heated diamond anvil cell. *Geophysical Research Letters*, *41*(11), 3833-3841.

Yonggang, G. Y., Wu, Z., & Wentzcovitch, R. M. (2008). α–β–γ transformations in Mg2SiO4 in Earth's transition zone. *Earth and Planetary Science Letters*, *273*(1-2), 115-122.

Yoshizawa, K., Yomogida, K., & Tsuboi, S. (1999). Resolving power of surface wave polarization data for higher-order heterogeneities. *Geophysical Journal International*, *138*(1), 205-220.

Yu, C., Day, E. A., De Hoop, M. V., Campillo, M., & Van Der Hilst, R. D. (2017). Mapping Mantle Transition Zone Discontinuities Beneath the Central Pacific With Array Processing ofSSPrecursors. *Journal of Geophysical Research: Solid Earth*, *122*(12), 10,364-310,378. https://doi.org/10.1002/2017jb014327

Yu, C., Goes, S., Day, E. A., & van der Hilst, R. D. (2023). Seismic evidence for global basalt accumulation in the mantle transition zone. *Science Advances*, *9*(22), eadg0095. https://doi.org/doi:10.1126/sciadv.adg0095

Yuan, X., Kind, R., Li, X., & Wang, R. (2006). The S receiver functions: synthetics and data example. *Geophysical Journal International*, *165*(2), 555-564. https://doi.org/10.1111/j.1365-246X.2006.02885.x

Zha, Y., Webb, S. C., & Menke, W. (2013). Determining the orientations of ocean bottom seismometers using ambient noise correlation. *Geophysical Journal Letters*. https://doi.org/10.1002/grl.50698

Zhang, Z., Irving, J. C., Simons, F. J., & Alkhalifah, T. (2023). Seismic evidence for a 1000 km mantle discontinuity under the Pacific. *Nature Communications*, *14*(1), 1714.

Zhang, Z., & Olugboji, T. (2023). Lithospheric imaging through reverberant layers: Sediments, oceans, and glaciers. *Journal of Geophysical Research: Solid Earth*, *128*(5), e2022JB026348.

Zhao, D., Yamamoto, Y., & Yanada, T. (2013). Global mantle heterogeneity and its influence on teleseismic regional tomography. *Gondwana Research*, *23*(2), 595-616.

Zheng, Z., Ventosa, S., & Romanowicz, B. (2015). High resolution upper mantle discontinuity images across the Pacific Ocean from SS precursors using local slant stack filters. *Geophysical Journal International*, *202*(1), 175-189.

Zhou, Y. (2018). Anomalous mantle transition zone beneath the Yellowstone hotspot track. *Nature Geoscience*, *11*(6), 449-453.